Superconducting InSb nanowire devices

Szombati, Daniel

DOI
10.4233/uuid:117aac8c-bd12-48fb-ae93-834f1ee62417

Publication date
2017

Document Version
Final published version

Citation (APA)
Szombati, D. (2017). *Superconducting InSb nanowire devices*. [Dissertation (TU Delft), Delft University of Technology]. https://doi.org/10.4233/uuid:117aac8c-bd12-48fb-ae93-834f1ee62417

SUPERCONDUCTING INSB NANOWIRE DEVICES

SUPERCONDUCTING INSB NANOWIRE DEVICES

Proefschrift

ter verkrijging van de graad van doctor
aan de Technische Universiteit Delft,
op gezag van de Rector Magnificus prof. ir. K.C.A.M. Luyben,
voorzitter van het College voor Promoties,
in het openbaar te verdedigen op vrijdag 24 maart 2017 om 10:00 uur

door

Daniel SZOMBATI

Master of Sciences
geboren te Budapest, Hongarije.

Dit proefschrift is goedgekeurd door de

promotor: Prof.dr.ir. L.P. Kouwenhoven

Samenstelling promotiecommissie:

Rector Magnificus,	voorzitter
Prof.dr.ir. L.P. Kouwenhoven,	Technische Universiteit Delft
Onafhankelijke leden:	
Prof.dr. Y.M. Blanter,	Technische Universiteit Delft
Prof.dr.ir. J. Aarts,	Universiteit Leiden
Prof.dr. S.D.C. Wehner,	Technische Universiteit Delft
dr. F. Giazotto,	Scuola Normale Superiore di Pisa, Italië
Prof.dr.ir. R. Hanson,	Technische Universiteit Delft, reservelid
Overige leden:	
Prof.dr.ir. E.P.A.M. Bakkers,	Technische Universiteit Delft

Printed by: Proefschriftmaken.nl

Front & Back: SEM image of the DC-SQUID used to measure the Josephson φ_0-junction. Designed by Sara Szombati.

Casimir PhD Series, Delft-Leiden 2017-06

ISBN 978-90-8593-291-8

An electronic version of this dissertation is available at
http://repository.tudelft.nl/.

Beauty at low temperatures is beauty.

Joseph Brodsky

CONTENTS

SUMMARY

Josephson junctions form a two-level system which is used as a building block for many types of superconducting qubits. Junctions fabricated from semiconducting nanowires are gate-tunable and offer electrostatically adjustable Josephson energy, highly desirable in qubit architecture. Studying nanowire weak links is therefore important for future quantum computing applications. The inherent spin-orbit interaction and high g-factor of InSb nanowires promise rich physics when combined with superconductivity, especially when an external magnetic field is applied. In particular, it can give rise to topological state of matter including Majorana bound states, paving the way for a novel type of fault-tolerant topological qubit. Such quantum computation can be realized when Majorana bound states are braided through a network of topological wires. Probing the magnitude and phase of the supercurrent through InSb nanowires provides insight on the feasibility of realizing topological states in these wires. This thesis describes experiments measuring the critical current and density of states of InSb nanowire Josephson junctions which are either voltage- current- or phase-biased, as the chemical potential or magnetic field inside the wire is changed.

In Chapter 3, the critical current through an InSb nanowire with NbTiN electrodes is measured. The critical current can be as high as $\sim$ 100 nA but decays rapidly with magnetic field followed by an aperiodic oscillation. Numerical simulations of the supercurrent through the nanowire show that this supercurrent profile is caused mostly by the interference between the transverse modes carrying the supercurrent inside the nanowire. This so–called orbital effect becomes significant beyond 100 mT, while the spin–orbit and Zeeman interactions become substantial at magnetic field of the order $\sim$ 1 T.

The Josephson energy through cross-shaped nanowires, grown by merging individual InSb nanowires, is investigated in Chapter 4. A finite Josephson coupling is measured through all branches of the nanocross, even when the length of the weak link extends beyond 1 μm. This is a requirement for braiding Majorana bound states hosted in such nanowire networks.

In Chapter 5 we build a quantum dot with two superconducting and a normal contact using the three legs of a nanowire cross. The superconducting terminals are joined in a loop such that superconducting interference can be probed by threading a flux. The density of states as a function of voltage bias, dot chemical potential and flux is probed through the quantum dot via the normal lead acting as a tunnel probe. It is revealed that the proximity effect can be turned on and off via both the bias and gate voltage. The pairing amplitude on the dot remains finite for in-plane magnetic field values up to 600 mT, suggesting that the nanowire cross platform is suitable for braiding, since a topological state can be reached at 100-200 mT. As the conductance through the dot is sensitive to the flux through the loop, the device may also be used as a mangetometer converting flux to current with a sensitivity of $1\,\frac{\mathrm{nA}}{\Phi_0}$.

The superconducting phase across a nanowire quantum dot as a function of the magnitude and direction of a large in-plane magnetic field is investigated in Chapter6. The nanowire is embedded in a DC-SQUID where one arm consists of a gate-defined quantum dot in the nanowire and the other is a nanowire reference junction, also gate-tunable. By measuring the critical current through the SQUID as a function of the flux and the chemical potential of the dot, we can detect the change of phase through the ground state of the dot. At zero-field we measure the 0-π transition of the quantum dot Josephson junction as the ground state parity of the dot changes. When the magnetic field exceeds 100 mT a 0-φ transition is measured indicating the presence of an anomalous supercurrent flow at vanishing phase difference across the quantum dot. This anomalous current is enabled by the breaking of the chiral symmetry due to spin-orbit interaction in the nanowire and the time-reversal symmetry breaking of the magnetic field. The phase of the 0-φ transition, or equivalently the magnitude of the anomalous current, can be tuned continuously via the gate underneath the dot. Such a φ_0 junction may serve as a phase bias element and have applications in superconducting spintronics.

Chapter 7 focuses on future experiments aiming to detect and control Majorana bound states in a superconducting InSb nanowire. Such devices can be expanded to a braiding circuit, realizing a topological quantum computer.

SAMENVATTING

Josephson juncties vormen de bouwsteen voor vele toepassingen in de kwantum informatica. Eén dimensionele nanodraden zijn gate controlleerbaar en vormen een veelzijdig platform door het bieden van elektrostatisch regelbare Josephson energie; het bestuderen van zwakke links is dan ook belangrijk voor toekomstige kwantum informatica toepassingen. De inherente spin-baan koppeling en hoge g-factor van InSb in combinatie met supergeleiding beloven rijke fysica, in het bijzonder wanneer een extern magneet veld wordt aangeboden. Meer specifiek kan dit leiden tot topologische toestanden van materie waarin gelokaliseerde Majorana toestanden aanwezig zijn. Fout-tolerante kwantum informatica kan gerealiseerd worden door het 'vlechten' van gelokaliseerde Majorana toestanden in een netwerk van topologische draden. Het meten van de grootte en fase van superstroom door InSb nanodraden geeft inzicht in de mate waarin deze topologische toestanden gerealiseerd kunnen worden in dergelijke draden.

De kritische stroom door een InSb nanodraad met NbTiN electrodes kan een sterkte bereiken van ~ 100 nA, maar valt snel af in magneetveld, en wordt daarna gevolgd door een aperiodieke oscillatie. Numerieke simulaties van de superstroom door de nanodraad tonen aan dat dit superstroom profiel hoogst waarschijnlijk veroorzaakt wordt door interferentie tussen de verschillend transverse kanalen die de superstroom transporteren. Dit zogenaamde orbitale effect wordt van belang boven 100 mT, terwijl de spin-baan en Zeeman interacties substantieel worden bij magneetvelden van orde ~ 1 T (Chapter3).

De Josephson energie door kruisvormige nanodraden, gegroeid door het samenvoegen van individuele InSb nanodraden, is onderzocht in Hoofdstuk4. Een eindige Josephson koppeling is gemeten door alle takken van het nanokruis, zelfs wanneer de lengte van de zwakke link groter is dan μm. Dit is een vereiste voor het vlechten van gelokaliseerde Majorana toestanden aanwezig in dit soort nanodraad netwerken.

In Hoofdstuk5 construeren we een kwantum dot met twee supergeleidende en één normaal contact door de drie armen van een nanokruis te gebruiken. De supergeleidende reservoirs zijn verbonden via een ring zodat supergeleidende interferentie gemeten kan worden wanneer een flux in de ring aanwezig is. De toestandsdichtheid als een functie van bias voltage, dot chemische potentiaal en flux is gemeten door het kwantum dot via het normale contact dat fungeerd als tunneling sensor. Dit maakt duidelijk dat het proximity effect kan worden aan en uitgezet via zowel het bias als het gate voltage. De parings amplitude op het dot blijf eindig for planaire magneetveld waardes tot 600 mT, wat suggereerd dat het nanokruis platform geschikt is voor vlechten, aangezien een topologische toestand kan worden bereikt vanaf 100-200 mT. Omdat de geleiding door het dot afhankelijk is van de flux door de ring, kan de structuur als magnetometer worden gebruikt die flux in stroom converteerd met een gevoeligheid van $1\frac{\text{nA}}{\Phi_0}$.

De supergeleidende fase over een nanodraad kwantum dot als een functie van grootte en richting van een sterk planair magneetveld is bestudeerd in Hoofdstuk6. De nano-

draad is onderdeel van een DC-SQUID waarbij één arm bestaat uit een gate gedefinieerd kwantum dot in de nanodraad en de andere is een nanodraad referentie junctie die eveneens gate controleerbaar is. Door de kritische stroom door het SQUID te meten als een functie van de flux en de chemische potentiaal van het dot kunnen we de verandering in fase meten door de grondtoestand van het dot. Bij nul veld meten we de 0-π transitie van de dot superstroom wanneer de gepaardheid van het dot veranderd. Wanner het magneetveld 100 mT overstijgt wordt een 0-φ transitie gemeten, wat de aanwezigheid van een anomale superstroom aangeeft bij verdwijnend faseverschil over het dot. Deze anomale superstroom wordt mogelijk gemaakt door het breken van de chirale symmetrie door spin-baan koppeling in de nanodraad en het breken van tijdsomkeerbaarheids symmetry door het magneetveld. De fase van de 0-φ transitie, of het equivalent, de grootte van de anomale stroom, kan continue geregeld worden via de gate onder het dot. Een dergelijk 0-φ junctie kan cruciale toepassingen hebben in supergeleidende spintronica.

Toekomstige experimenten doelend op een topologische kwantum computer moeten focussen op een verbeterde controle over de geinduceerde gap in de nanodraad en op de opbrengst van nanodraad kruizen die als vlecht platform kunnen dienen. Een cruciaal aandachtspunt is het vinden van het juiste materiaal en depositie methode om een geschikt supergeleider-halfgeleider grensvlak te verkrijgen. De Josephson 0-φ -junctie kan ook gebruikt worden als sensor van de topologische toestand van de nanodraad (Hoofdstuk7).

1

INTRODUCTION

1.1. THE STRANGE WORLD OF QUANTUM MECHANICS

From the time of Newton until the dawn of the twentieth century, this rational reductionist view that the world is just a collection of multitude of billiard balls bouncing in predictable manner dominated the mind of physicists. They believed the world can be understood as the sum of its parts, and given the initial conditions of a system, one can predict its evolution til the end of times. This view was very successful at explaining the macroscopic world surrounding us.

At the turn of the twentieth century, however, as physicist were diving in to the microscopic world of smaller and smaller objects, classical physics was inadequate to explain some experiments, such as the energy emitted by a black body or the photoelectric effect. New axioms and rules had to be nailed down.

From the understanding of this microscopic world emerged the laws of quantum mechanics, with strange rules counter-intuitive to our every day lives. The law of *superposition* states that a system is simultaneously existent in all its possible configurations, until its probabilistic collapse when measured by an outside observer. Two particles may become *entangled* whereby they remain connected and one influences the other, no matter how far apart they are, implying *non-locality*. These rules reveal a new universe arising at the level electrons, atoms, molecules, light, and even microscopic objects cooled down to low temperatures. As this world is mindbogglingly complicated for us humans to understand, we build computers behaving accordingly to the rules to predict how its behavior. This is the role of the quantum computer.

1.2. BENIFITS OF QUANTUM COMPUTING

Classical computers use binary bits to perform logical operations. Each bit is in one of the two states 0 or 1. A quantum two-level system, called qubit, can be in a superposition of both $|0\rangle$ and $|1\rangle$ states. The state $|s\rangle$ of a qubit can be expressed as

$$|s\rangle = \alpha|0\rangle + \beta|1\rangle,$$

where α and β are complex numbers which normalize to unity. If we neglect the global complex phase of $|s\rangle$ and only care about the relative phase between the state $|0\rangle$ and $|1\rangle$, two real numbers are necessary to encode state $|s\rangle$. A classical computer requires 2×64 bits to encode this information assuming an accuracy up to 19 significant figures ($\log_2 10^{19} \approx 63.1$). In case of 20 qubits, there are 2^{20} basis states, and the quantum state of such system carries the information of $2\times 2^{20}-2$ real numbers, requiring around 10^8 classical bits or encoding. This is already quite a challenge for computers and the resource needed grows exponentially with the number of qubits. The main driving force behind realizing a quantum computer is to simulate quantum systems, such as binding energies of large molecules, folding of proteins of hundreds of atoms long or the ground state of physical systems. These quantum problems necessitate resources unreachable via classical computers, since calculating all possibilities is a too large sample space. As Feynamnn remarked however, the quantum world can simulate itself, thus building a controllable quantum system is the goal of quantum computing.

The major challenge is to engineer quantum two-level systems where each qubit can interact with any given other qubit upon user request, but is isolated from the environment. Isolation is crucial, since an non-isolated qubit will entangle with the outside world which will then influence the state of the qubit, resulting in decoherence and loss of quantum information.

1.3. SUPERCONDUCTIVITY AND TOPOLOGICAL QUANTUM COMPUTING

Superconductivity is the phenomena where an electric conductor cooled below a certain temperature looses its resistance completely. This cannot be explained under the classical Drude theory of electric conduction, which treats electrons as individual particles accelerating towards a positive potential with a drag force due to collision with the atomic nuclei. In fact, inside a superconductor electrons are connected and form a many body quantum ground state, called BCS condensate (after Bardeen, Schrieffer and Cooper who proposed the theory).

Superconductors thus, despite being of macroscopic size, are quantum objects and are well suited to form the basis for qubits in a quantum computer. For example, a superconducting loop interrupted on one end can be a quantum two-level system, where the states $|0\rangle$ and $|1\rangle$ are defined by the direction of the supercurrent flowing clockwise or anti-clockwise(cartoon of a flux qubit). Or two superconducting islands connected by a thin barrier, where the two states are the even and odd parity of the total charge of one island (charge qubit and transmon). Qubits based on superconductors are nowadays the most prominent candidates for a functioning quantum computer as they can be easily coupled via resonators and their dephasing time is well beyond the timescale for operations.

Superconductors also promise, however, a qubit which does not interact with the environment and thus does not dephase. This is the topological qubit built of Majorana fermions[1–3]. These are particles predicted by the Italian physicist Ettore Majorana, with their defining property being that they are equal to their antiparticle[4]. In superconductors, electron-like and hole-like quasiparticle excitations are equivalent.

Thus superconductors provide a natural environment to engineer Majorana-like quasiparticles, called Majorana bound states.

Condense matter physicists have shown recently[5, 6] that Majorana bound states can be engineered in a one dimensional semiconductor with finite g-factor and spin-orbit interaction, inside which superconductivity is induced. Such a system has two topological phases, depending on the chemical potential of the nanowire and the magnitude of the external magnetic field. If the magnetic field is smaller than a critical value, the superconducting nanowire has a single ground state lacking Majoranas. If the external field exceeds the critical value, the system hosts a pair of Majoranas and two degenerate ground states. These two topological orders are distinct and cannot change into each other unless succumbing to a phase transition. In other words, Majoranas are robust against perturbations of the system and quantum information can be encoded without loss.

1.4. OUTLINE OF THIS THESIS

This thesis is devoted to studying the Josephson effect, which is the flow of supercurrent through an interrupted superconductor, in systems capable of hosting Majorana fermions. A range of experiments are described involving two superconductors interrupted by InSb nanowire, with varying geometries.

- Chapter 2 provides the underlying theory of BCS superconductivity and the microscopic theory of Andreev bound states in 1D junctions and quantum dots.
- Chapter 3 studies the critical current through InSb Josephson junctions as a function of magnetic field strength and direction.
- Chapter 4 describes InSb nanowire networks, grown from merged individual wires and contacted by superconductors. Supercurrent and differential conductance measurements are performed between each terminal pair.
- A three terminal quantum dot is fabricated from a T-shaped nanowire in Chapter 5. The dot is phase biased via two superconducting lead and the third normal lead is used to probe the quantum dot levels at zero and finite magnetic field.
- In Chapter 6 a quantum dot is created in an InSb nanowire and embedded in a dc-SQUID geometry for phase biasing. The phase of the supercurrent flowing through the dot is probed as a function of external mangetic field magnitude and direction.
- In Chapter 7 I summarize the conclusion of each experiment and provide an outlook for future experiments.
- Appendix A introduces Majorana bound states in nanowires, a relevant topic to the thesis. Appendix B summerizes the fabrication details of the devices presented in this book.

1

BIBLIOGRAPHY

[1] N. Read and D. Green, "Paired states of fermions in two dimensions with breaking of parity and time-reversal symmetries and the fractional quantum Hall effect," *Phys. Rev. B*, vol. 61, pp. 10267–10297, Apr. 2000.

[2] D. A. Ivanov, "Non-Abelian Statistics of Half-Quantum Vortices in *p*-Wave Superconductors," *Phys. Rev. Lett.*, vol. 86, pp. 268–271, Jan. 2001.

[3] A. Y. Kitaev, "Unpaired Majorana fermions in quantum wires," *Phys.-Usp.*, vol. 44, no. 10S, p. 131, 2001.

[4] E. Majorana, "Teoria simmetrica dell'elettrone e del positrone," *Nuovo Cim*, vol. 14, pp. 171–184, Sept. 2008.

[5] Y. Oreg, G. Refael, and F. von Oppen, "Helical Liquids and Majorana Bound States in Quantum Wires," *Phys. Rev. Lett.*, vol. 105, p. 177002, Oct. 2010.

[6] R. M. Lutchyn, J. D. Sau, and S. Das Sarma, "Majorana Fermions and a Topological Phase Transition in Semiconductor-Superconductor Heterostructures," *Phys. Rev. Lett.*, vol. 105, p. 077001, Aug. 2010.

2

THEORY

This chapter outlines the key ideas of Andreev physics necessary to understand the overall behavior of the nanowire Josephson junction devices presented in this thesis. First a brief derivation of the physics of bulk superconductors, Andreev reflection, BTK theory and Andreev bound states are given from microscopic principles. Then the Josephson effect in magnetic field and through quantum dots is described, in particular π and φ_0-junction physics. Finally we introduce SQUIDs as a method for phase biasing junctions.

2.1. SUPERCONDUCTIVITY IN THE BULK

Superconductivity was first discovered experimentally in 1911 by Heike Kamerlingh Onnes[1]. A complete microscopic description of the phenomenon had to wait till 1957 for Bardeen, Cooper and Schrieffer's proposed BCS theory: their model was based on a variational mean-field approach of the phonon-mediated attractive potential acting on the electrons below the critical temperature[2].

The derivation presented here follows the work of Bagwell and Datta who transformed the Hamiltonian into a quadratic form such that the excitations of the superconductor are analogous to that of a one-particle system[3].

The pioneering theses on Andreev physics of Pillet and Bretheau[4, 5] were used as an inspiration for this chapter and is a recommended read for anyone wishing to grasp the essence of Josephson weak links.

We first derive the energy spectrum and states of a bulk uniform BCS superconductor with spin-symmetry in the one-particle picture, where the solutions are classified according to their energy. We subsequently deal with the excitation and semiconductor picture, which are needed if arbitrary spin-independent interactions are to be considered.

2.1.1. THE BOGOLIUBOV-DE GENNES EQUATIONS AND THE BCS HAMILTONIAN

When a superconductor is cooled below its critical temperature, attractive correlations arise between electrons, which dominate over the Coulomb repulsion. In BCS theory, this attraction is modeled by a mean-field approximation. The second quantization Hamiltonian for a bulk superconductor in terms of electron creation $c^\dagger_{k\sigma}$ and annihilation operators $c_{k\sigma}$ (where k and σ denote momentum and spin respectively) takes the form

$$H_{BdG} = \sum_{k,\sigma=\uparrow,\downarrow} \xi_{k\sigma} c^\dagger_{k\sigma} c_{k\sigma} + \sum_k \Delta_k c^\dagger_{k\uparrow} c^\dagger_{-k\downarrow} + \Delta^\star_k c_{-k\downarrow} c_{k\uparrow}, \tag{2.1}$$

where $\xi_{k\sigma} = \frac{\hbar^2 k^2}{2m} - \mu$ is the kinetic energy[1] relative to the chemical potential μ of an electron of mass m and momentum k and spin σ. The source of superconductivity rises from the complex pairing term Δ_k which couples electrons and holes of opposite spin and momentum. For the scope of this thesis we assume s-wave pairing where $\Delta_k = |\Delta| e^{i\varphi}$ is independent of momentum.

To transform this Hamiltonian to a quadratic form which resembles a system of non-interacting particles, a spinor field Ψ_k is introduced with a spin-up electron component of momentum k and a spin-down hole component of momentum $-k$:

$$\Psi_k \equiv \begin{pmatrix} c_{k\uparrow} \\ c^\dagger_{-k\downarrow} \end{pmatrix}. \tag{2.2}$$

[1] Although in the absence of magnetic field ξ is independent of spin, we keep the σ label as a reminder that in the presence of Zeeman interaction $\xi_{k\sigma} = \frac{\hbar^2 k^2}{2m} - \mu + E_\sigma$.

Rewritten in the spinor basis and using the Fermionic anticommutation rules $[c_{k\sigma}, c^{\dagger}_{k'\sigma'}] = \delta_{kk',\sigma\sigma'}$, the Hamiltonian gains the form[2]

$$H_{BdG} = \sum_k \Psi^{\dagger}_k \mathscr{H} \Psi_k \tag{2.3}$$
$$\mathscr{H} = \begin{pmatrix} \xi_{k\uparrow} & \Delta_k \\ \Delta^*_k & -\xi_{-k\downarrow} \end{pmatrix}.$$

We look for plane wave solutions of the Schrödinger equation for H_{BDG} of the form $(u_k \; v_k)^{\dagger} e^{ikr}$. The two spinor components u_k and v_k called "coherence factors" stand for the electron and hole part of the wavefunction and satisfy:

$$\mathscr{H} \begin{pmatrix} u_k \\ v_k \end{pmatrix} = E_k \begin{pmatrix} u_k \\ v_k \end{pmatrix}, \tag{2.4}$$

where E_k is measured with respect to the chemical potential μ. Equation 2.4 is called the Bogoliubov-de-Gennes equation. For a spin-degenerate system, such as a bulk s-wave superconductor in the absence of magnetic field, the Hamiltonian $\mathscr{H}$ in 2.3 obeys $\mathscr{H}^{\dagger} = -\mathscr{H}$. Thus if $(u_k \; v_k)^{\dagger}$ is a solution to 2.4 with energy E_k, $(-v^*_k \; u^*_k)^{\dagger}$ is also a solution with energy $-E_k$.

Without loss of generality we categorize the two linearly independent solutions of 2.4 as $|k_+\rangle$ wavefunctions with positive energies and $|k_-\rangle$ wavefunctions with negative energies (relative to μ):

$$\begin{cases} |k_+\rangle = \begin{pmatrix} u_k \\ v_k \end{pmatrix} e^{ikr} \\ |k_-\rangle = \begin{pmatrix} -v^*_k \\ u^*_k \end{pmatrix} e^{ikr} \end{cases}$$

The condition that the solutions normalize to unity implies $|u_k|^2 + |v_k|^2 = 1$.
Solving for the coherence factors with the above requirements yields

$$E_{k\pm} = \pm\sqrt{\Delta^2 + \xi^2_k} \tag{2.5}$$

$$\begin{cases} u_k &= e^{-i\frac{\varphi}{2}} \sqrt{\frac{1}{2}\left(1 + \frac{\xi_k}{\sqrt{\Delta^2+\xi^2_k}}\right)} \\ v_k &= e^{i\frac{\varphi}{2}} \sqrt{\frac{1}{2}\left(1 - \frac{\xi_k}{\sqrt{\Delta^2+\xi^2_k}}\right)} \end{cases} \tag{2.6}$$

It is now helpful to apply a basis transformation to 2.4, changing to the new orthonormal basis we found above γ_{k-}, γ_{k+}:

$$\begin{cases} \gamma^{\dagger}_{k+} &= u_k c_{k\uparrow} + v_k c^{\dagger}_{-k\downarrow} \\ \gamma^{\dagger}_{k-} &= -v^*_k c_{k\uparrow} + u^*_k c^{\dagger}_{-k\downarrow} \end{cases} \tag{2.7}$$

[2] We ignore the constant of energy $\sum_k \xi_{-k\downarrow}$ resulting from the anticommutation.

The diagonalized Schrödinger equation in this new basis now takes the form

$$H_{BdG} = \sum_{k\in E} E_{k-}\gamma^{\dagger}_{k-}\gamma_{k-} + E_{k+}\gamma^{\dagger}_{k+}\gamma_{k+}. \tag{2.8}$$

We are now in a position to make some important remarks on the nature of one particle-like excitations $\gamma^{\dagger}_{k\pm}$ in a superconductor, called "Bogoliubons" since they are a linear superposition of electrons and holes following the Bogoliubov transformation 2.7.

The energy spectrum 2.5 implies that there are no allowed energy excitations for energies less than Δ from the fermi energy, i.e. $|E| \geq \Delta$. There is an energy gap of 2Δ in the excitation spectrum of a bulk superconductor.

Bogoliubons are composed of a superposition of electrons and holes[3]. The electon-hole ratio is apparent from 2.6: the superposition depends on the energies of the excitation. The further the energy is from Δ, the more the Bogoliubons is fully electron or hole-like.

CASE OF FINITE ZEEMAN ENERGY

Assuming a finite Zeeman energy $E_Z = \frac{1}{2}\mu_B g\sigma\cdot\mathbf{B}$ acts on the electrons and holes, the energy eigenvalues for the positive and negative energy band shift by the Zeeman energy[5]:

$$E_{k\pm} = \pm\sqrt{\Delta^2 + \xi_k^2} + E_Z \tag{2.9}$$

Both energy band shift in the same direction which are no longer symmetric about the Fermi energy. In other words a finite spin-splitting introduces an asymmetry between the positive and negative excitation energies.

2.1.2. GROUND STATE, EXCITATIONS AND DENSITY OF STATES OF A BULK SUPERCONDUCTOR

ONE-PARTICLE PICTURE

Bogoliubons can be regarded as single particle excitations in a “superconducting vacuum”. The vacuum state in this respect is the state $|\mathrm{V}\rangle$ with no Bogoliubons, i.e. $\gamma_{k\pm}|\mathrm{V}\rangle = 0$. One can check that

$$|\mathrm{V}\rangle \equiv \prod_k c^{\dagger}_{-k\downarrow}|0\rangle \tag{2.10}$$

indeed satisfies the condition. The energy of the vacuum state is $E_{\mathrm{V}} = \sum_k \xi_{-k\downarrow}$.

Since $|\mathrm{V}\rangle$ is an eigenstate of H_{BDG}, so is $\gamma_{k\pm}|\mathrm{V}\rangle$ for any $k\pm$. We can thus construct the ground state $|\mathrm{GS}\rangle$ of our superconductor by adding all negative energy excitations to $|\mathrm{V}\rangle$:

$$\begin{aligned}|\mathrm{GS}\rangle &= \prod_k \gamma^{\dagger}_{k-}|\mathrm{V}\rangle \\ &= \prod_k \left(u_k - v_k c^{\dagger}_{k\uparrow}c^{\dagger}_{-k\downarrow}\right)|0\rangle\end{aligned} \tag{2.11}$$

[3] In the superconducting community a “hole” is an empty electron-state below the chemical potential, as opposed to the semiconducting community where holes are empty states below the bandgap.

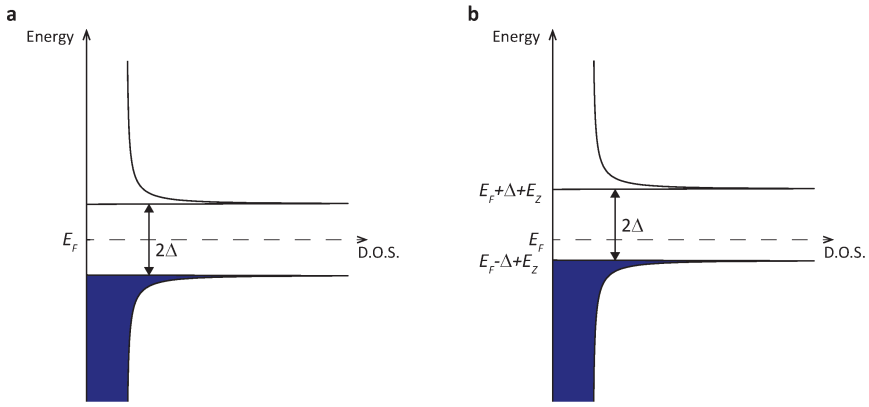

Figure 2.1: **Quasiparticle spectrum of the BCS ground state.** The figure shows the one-particle representation of the ground state of a BCS superconductor with: **a,** no external magnetic field; **b,** a finite magnetic field resulting in a Zeeman energy E_Z. All quasiparticle states below the Fermi energy are filled, while states above E_F are left empty. There are no available quasiparticle states for energies $|E - E_F| < \Delta$

with energy $E_{\mathsf{GS}} = E_{\mathsf{V}} + \sum_k E_{k-}$. This is the usual BCS ground state, a condensate constituted of a sea of paired electrons of opposite spin and momentum, the Cooper pairs. Because the Hamiltonian 2.1 does not conserve particle number, the ground state does not have a fixed number of particles. However parity is conserved and hence parity is a good quantum number. The parity of the ground state is even.

The excited states closest in energy to the ground state are obtained by either adding a Bogoliubon of positive energy $|\mathsf{ES}+\rangle = \gamma^\dagger_{k+}|\mathsf{GS}\rangle$ which has energy $E_{\mathsf{GS}} + E_{k+}$ or by removing a Bogoliubon of negative energy $|\mathsf{ES}-\rangle = \gamma_{k-}|\mathsf{GS}\rangle$ which has energy $E_{\mathsf{GS}} + |E_{k-}|$. Both these excited states differ by one in particle number from the ground state and have therefore odd parity. If the system is spin-degenerate these two excitations have the same energy but opposite spin.

It is important to emphasize here that although by mathematical tricks we produced a one-particle like representation of the superconducting ground state and excited states, 2.11 demonstrates this is in fact a many-body state involving all electrons pairing up and gathering into a condensate forming a macroscopic coherent quantum state. Thus a bulk piece of superconductor, no matter the size, embodies a single quantum state. This feature is the appeal of superconductors for quantum computational purposes.

The BCS density of states can be calculated from the normal density of states: $\mathsf{N_S}(\mathsf{E})\mathrm{d}\mathsf{E} = \frac{1}{2}\mathsf{N_N}(\xi)\mathrm{d}\xi$. Assuming a constant normal density of states leads to

$$\mathsf{N_S}(\mathsf{E}) = \frac{1}{2}\mathsf{N_N}(0)\begin{cases} \frac{|E|}{\sqrt{E^2-\Delta^2}} & \text{if } |E| > \Delta \\ 0 & \text{otherwise} \end{cases} \tag{2.12}$$

or in case of a finite Zeeman energy

$$\mathsf{N_S}(\mathsf{E}) = \frac{1}{2}\mathsf{N_N}(0)\begin{cases} \frac{|E-E_Z|}{\sqrt{(E-E_Z)^2-\Delta^2}} & \text{if } |E| > \Delta \\ 0 & \text{otherwise} \end{cases}. \tag{2.13}$$

The BCS density of states is gapped around the Fermi energy by 2Δ and diverges at $E = \pm\Delta$ (the so-called coherence peaks). The ground state is represented in Figure 2.1.

The one-particle picture presented above groups the Bogoliubon by the positive and negative energy excitations and is the most compact representation of the BCS many-body state. It is useful to build the ground state from the vacuum state. However, the existing spin-dependency is hidden in this representation, which is crucial for experiments involving magnetic-fields or Majorana physics.

EXCITATION PICTURE

Excitations in the one-particle picture are produced either by adding a Bogoliubon of positive energy $\gamma^\dagger_{k+}$ or removing a Bogoliubon of negative energy γ_{k-}. These two excitations have opposite spin. After a transformation on the Bogoliubon operators defined in 2.7

$$\begin{cases} \gamma^\dagger_{E_{k\downarrow}} & \equiv & \gamma^\dagger_{k+} \\ \gamma^\dagger_{E_{k\uparrow}} & \equiv & \gamma_{k-} \\ E_{k\downarrow} & \equiv & E_{k+} \\ E_{k\uparrow} & \equiv & -E_{k-} \end{cases} \tag{2.14}$$

the Hamiltonian H_{BdG} becomes

$$H^{exc}_{BdG} = \sum_k E_{k\downarrow}\gamma^\dagger_{E_{k\downarrow}}\gamma_{E_{k\downarrow}} + E_{k\uparrow}\gamma^\dagger_{E_{k\uparrow}}\gamma_{E_{k\uparrow}} + E_V - \sum_k E_{k\uparrow}. \tag{2.15}$$

This Hamiltonian only contains excitation with positive energy ($E_{k\downarrow}, E_{k\uparrow} > 0$), thus the ground state in the excitation picture is empty. The ground state can be excited either by adding a spin-down Bogoliubon $|\mathsf{ES}+\rangle = \gamma^\dagger_{E_{k\downarrow}}|\mathsf{GS}\rangle$ or a spin-up Bogoliubon $|\mathsf{ES}-\rangle = \gamma^\dagger_{E_{k\uparrow}}|\mathsf{GS}\rangle$, resulting in an increase in energy of $E_{k\downarrow}$ and $E_{k\uparrow}$ respectively[4].

Basically, the excitation picture corresponds to mirroring the full quasi-particle branch of the one-particle picture over the Fermi level resulting in a second empty branch, as seen in Figure 2.2. Although the architecture of the ground state is not present in this representation, it is useful to keep track of the spin-nature of the excitations of the superconductor and treat them all on the same footing, as all excitations have positive energy. This representation is used in the appendixA to derive the zero-energy Majorana excitations inside a superconductor.

SEMICONDUCTING PICTURE

In general to diagonalize the Bogoliubov-de Gennes Hamiltonian 2.1 which includes arbitrary spin-dependent or spin-independent interactions, such as for example spin-orbit coupling, the spinor substitution in 2.2 is not enough and one needs to double the

[4] Although for the spin-degenerate system we assumed in this chapter these two excitations have equal energy, this need not be the general case. For example in the presence of an external magnetic field $E_{k\downarrow} \neq E_{k\uparrow}$

degrees of freedom. The 4-dimensional Nambu spinor is then used:

$$\widetilde{\Psi_k} \equiv \begin{pmatrix} c_{k\uparrow} \\ c^\dagger_{-k\downarrow} \\ c^\dagger_{-k\uparrow} \\ c_{k\downarrow} \end{pmatrix}. \tag{2.16}$$

After diagonalization one finds four excitations: a spin-up($\gamma^\dagger_{E\uparrow}$) and spin-down excitation($\gamma^\dagger_{E\downarrow}$) with positive energy, and a spin-up($\gamma^\dagger_{-E\uparrow}$) and spin-down excitation($\gamma^\dagger_{-E\downarrow}$) with negative energy. This is a combined form of the one-particle picture and the excitation picture, where both spin and negative energy Bogoliubons are kept track of. However, since we have doubled the degrees of freedom there is a redundancy in the number of excited states, since removing a particle with negative energy is equivalent to adding a particle with the same positive energy and opposite spin:$\gamma^\dagger_{E\sigma} \equiv \gamma_{-E-\sigma}$.

To account for the redundancy, the Hamiltonian gains a factor $\frac{1}{2}$:

$$H^{semi}_{BdG} = \frac{1}{2}\left(\sum_k E_{k\downarrow}\gamma^\dagger_{E_{k\downarrow}}\gamma_{E_{k\downarrow}} + E_{k\uparrow}\gamma^\dagger_{E_{k\uparrow}}\gamma_{E_{k\uparrow}} + \sum_k -E_{k\downarrow}\gamma^\dagger_{-E_{k\downarrow}}\gamma_{E_{k\downarrow}} - E_{k\uparrow}\gamma^\dagger_{-E_{k\uparrow}}\gamma_{E_{k\uparrow}} + E_V - \sum_k E_{k\uparrow}\right). \tag{2.17}$$

The ground state is obtained by filling all spin-down and spin-up states with negative energy. The first excited state with spin up (spin down) is created by adding a spin-up(spin-down) excitation with lowest positive energy, or equivalently, removing a spin-down(spin-up) excitation with highest negative energy.

The semiconducting picture is obtained from the excitation picture by mirroring the two positive spin-dependent quasiparticle branches on the Fermi energy and filling the so-obtained branches. Thus in this picture one keeps track of the spin of the quasiparticles as well as allowing for negative energy excitations. This is important when for example considering transport experiments, where either quasiparticles are added to the superconductor or removed, depending on the voltage bias of the lead the superconductor is connected to. The semiconducting picture is also necessary to be able to write down an arbitrary spin-dependent Hamiltonian in a quadratic form, as a four dimensional spin is needed to treat spin independently of momentum. Such is the case of Majorana fermions in nanowires where spin-orbit is an essential component.

We present the ground state and excited state representation in each picture in Figure 2.2.

2.2. TRANSPORT THROUGH A NS INTERFACE: ANDREEV REFLECTION

2.2.1. REWRITING THE BCS SOLUTIONS INTO ELECTRON AND HOLE-LIKE STATES

In section 2.1.1 we have found the "one-particle-like" solutions to the excitations inside a conductor with BCS electron-hole pairing interaction $\Delta c^\dagger_{k\uparrow} c^\dagger_{-k\downarrow}$ by solving the Schrödinger

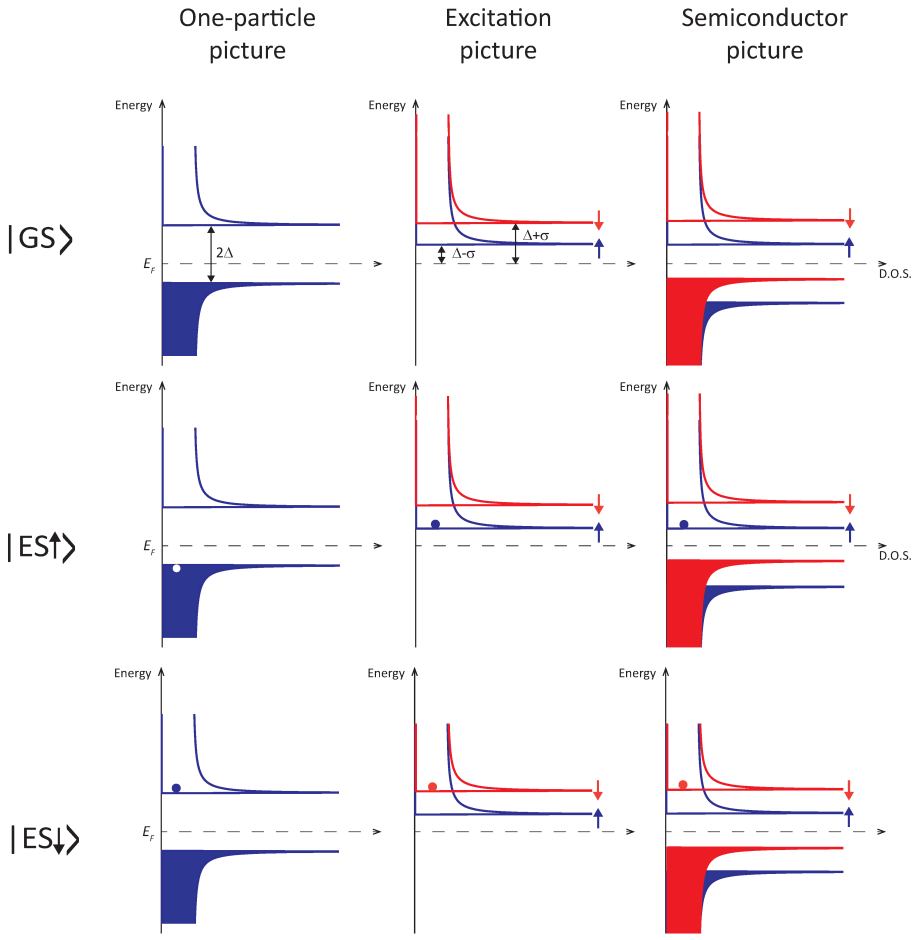

Figure 2.2: **BCS ground state and excited states in three representations.** For the excitation and semiconductor picture we labeled the bands with different spin. All DOS present the case of a finite Zeeman splitting so that the spin bands are shifted. Note that we show only one of the two representations of the excited states for the semiconducting picture.

equations for the Hamiltonian H_{BDG}. The solutions, given in terms of the coherence factors u_k and v_k in 2.6 have been expressed using a parametrization in the k-states. By reparametrizing these solution and expressing the coherence factors and momenta in terms of their energies E_k and renormalized kinetic energy $\tilde{\xi_k}$ we obtain:

$$\begin{cases} u_{e,h}(E,\varphi) = e^{-i\frac{\varphi}{2}}\left[\frac{1}{2}\left(1+\eta_{e,h}\sqrt{1-(\frac{\Delta}{E})^2}\right)\right]^{1/2} \\ v_{e,h}(E,\varphi) = e^{i\frac{\varphi}{2}} sgn(E)\left[\frac{1}{2}\left(1-\eta_{e,h}\sqrt{1-(\frac{\Delta}{E})^2}\right)\right]^{1/2} \\ k_{e,h}(E,\varphi) = k_F\left(1+\eta_{e,h} sgn(E)\frac{\sqrt{E^2-\Delta^2}}{\mu}\right)^{1/2} \end{cases} \tag{2.18}$$

Since the energy solutions E_k of 2.5 were four fold degenerate in $(\pm k, \pm\tilde{\xi})$, the relabelled solutions are also degenerate in $(\pm E_k, \pm\tilde{\xi})$. This degeneracy is included in 2.18 with the η factor which depends both on E_k and $\tilde{\xi}$ as $\eta = sgn(E_k)sgn(\xi)$. From rearranging the solutions we gain insight on the following two aspects of the excitations in a superconductor:

- For energies $|E| \geq \Delta$, k is real and the solutions are purely propagating plane waves. We also obtain a solution, however, for $|E| < \Delta$, in which case the imaginary wave vector k results in exponentially growing and decaying solutions. These kind of solutions do not exist in a uniform superconductor and are only allowed physically if the states are bounded by domain walls, i.e. if the order parameter Δ is inhomogeneous in space.

- The charge $q_E = v_k^2 - u_k^2$ of the excitation is

$$q_E = -\eta_{e,h}\sqrt{1-\left(\frac{\Delta}{E}\right)^2}.$$

  Thus in the limit $\frac{\Delta}{|E|} \to 0$ the eigenstates tend to a pure electron-like or pure hole-like states depending on the sign of η (η =+1 for electron-like and -1 for hole-like states). An excitation close to the superconducting gap edge Δ is a near-equivalent superposition of electrons and holes. Far away from the gap the wavefunction recovers resembling that of a pure electron or pure hole.

Thus the two linearly independent solutions of the the BdG Hamiltonian then can be written:

$$\underbrace{\begin{pmatrix} u_e(E,\varphi) \\ v_e(E,\varphi) \end{pmatrix} e^{ik_e(E)x}}_{\eta=1 \text{ electron-like wave}}; \underbrace{\begin{pmatrix} u_h(E,\varphi) \\ v_h(E,\varphi) \end{pmatrix} e^{ik_h(E)x}}_{\eta=-1 \text{ hole-like wave}} \tag{2.19}$$

2.2.2. ANDREEV REFLECTION ABOUT AN NS INTERFACE - BTK MODEL

To understand electron transport through a normal metal-superconductor interface, we outline the BTK model presented by Blonder, Tinkham and Klapwijk in their 1982 paper [6].

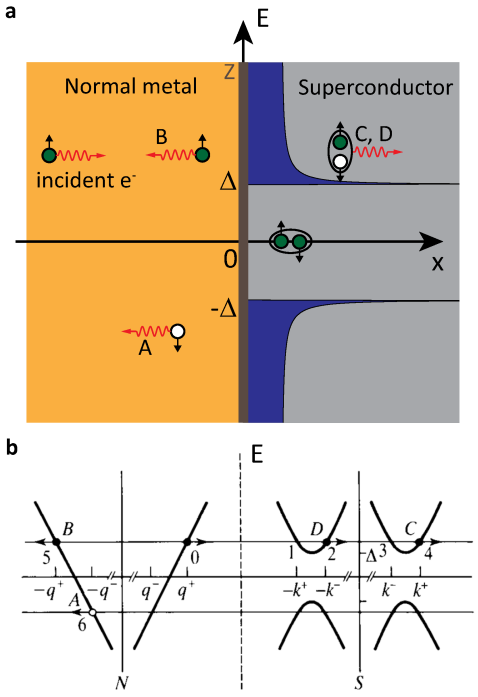

Figure 2.3: **Possible scenarios of an electron impinging on an NS interface in real and momentum space. a,**In real space, an electron of energy $E > \Delta$ propagating in a normal conductor towards S. After hitting the interface, the electron can Andreev reflect as a hole (A), reflect back normally as an electron (B) or propagate onward in S as a quasiparticle (C,D) creating a Cooper pair as well. **b,** Same events represented in momentum space. The straight lines show the linear dispersion in the normal side, while the parabolas show the quadratic dispersion of the superconductor.

Consider the situation presented in Figure 2.3**a** of an electron plane wave of energy E propagating inside a normal conductor ($\Delta(x)=0$) in the positive x-direction towards a superconductor ($\Delta(x)=\Delta$). At the interface $x=0$ there is a thin barrier separating N and S with variable transparency, modeled by a delta function of strength Z.

The picture is depicted in momentum space in Figure 2.3**b**, with linear plane-wave dispersion on the N side, and a quadratic superconducting dispersion $E_k = \pm\sqrt{\Delta^2 + \tilde{\xi}_k^{\,2}}$ on the S side. Depending on the energy E of the incoming electron, there can be four possible outcomes of the electron (labeled 0 in the Figure) hitting the delta potential:

- The electron can undergo full Andreev reflection(AR), where it is reflected back into the normal metal as a hole(label A) of opposite spin and energy $-E$, and simultaneously creating a Cooper pair in the superconductor.
- If $Z > 0$, the electron can reflect back as an electron of energy E (label B).
- If $|E| \geq \Delta$, there are available quasiparticle states and the electron is injected into the superconductor as a quasiparticle of energy E, with positive (C) or negative (D) k-momentum. This is accompanied by a partial Andreev reflection to account for charge conservation.

Figure 2.4**a** shows the probability of each transmission/reflection process as a function of incoming electron energy E for different values of barrier strength Z. In Figure 2.4**b** the corresponding dI/dV curves are plotted.

In the case of a complete transparent barrier ($Z = 0$), Andreev reflection occurs with probability 1 for energies within the gap, since there are no available quasiparticle states to access in the superconductor. This process has a charge transfer of $2e$, thus the conductance is twice the value of the normal conductance inside the gap, which then tends to R_N^{-1} as $E = eV \to \infty$.

In the opposite limit of a strong barrier, AR probability goes to zero and the electron is certainly reflected back as an electron, resulting in zero conductance.

The BTK model is useful to extract the transparency of a device with NS interface of which the I-V curve is measured. For a voltage $V \gtrsim 2\Delta$ the conductance reaches its asymptotic normal state conductance R_N^{-1}. The low voltage I-V curve however does not fit on the $I = R_N^{-1}V$ line. Instead, when the high voltage I-V curve is interpolated, it crosses the $V = 0$ axis as a finite current value $I_{exc} \equiv I(V = 0)$ called the excess current. The normalized excess current $\frac{eI_{exc}R_N}{\Delta}$ can be mapped one-to-one on the Z parameter value which can then be extracted using Figure 2.4**c**.

The same model was later adapted in a subsequent paper[8] for a superconducting SXS weak link, where the authors take into account the effects of normal scattering inside the junction.

2.3. TRANSPORT THROUGH AN SNS JUNCTION

2.3.1. ANDREEV BOUND STATES

As described in the previous section, Andreev reflection is a process where an electron traveling in a normal conductor reflects as a hole from a superconducting interface. As

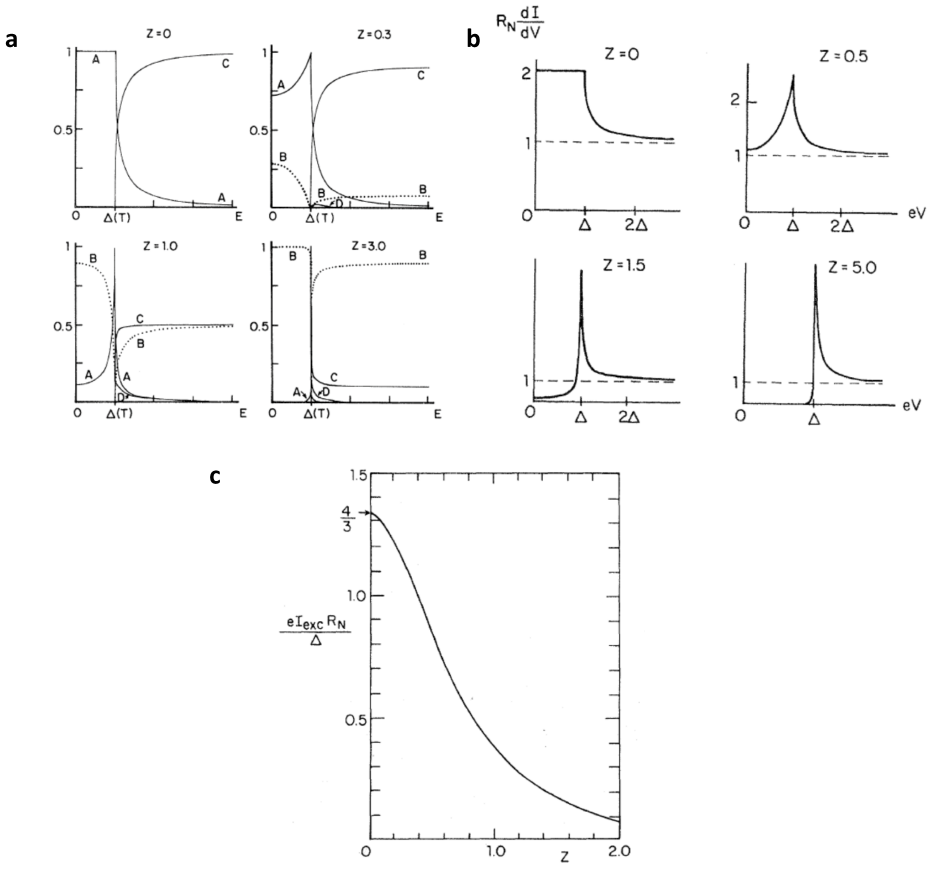

Figure 2.4: **BTK model of charge transfer and reflection about an NS interface. a,** Coefficient of Andreev reflection (A), normal reflection (B) and quasiparticle transfer without and with branchcrossing (C,D) as a function of incoming electron energy E for different barrier strengths. **b,** Differential conductance vs. voltage for different barrier strengths. **c,** Normalized excess current through the interface vs barrier strength. Figure reprinted from [7]

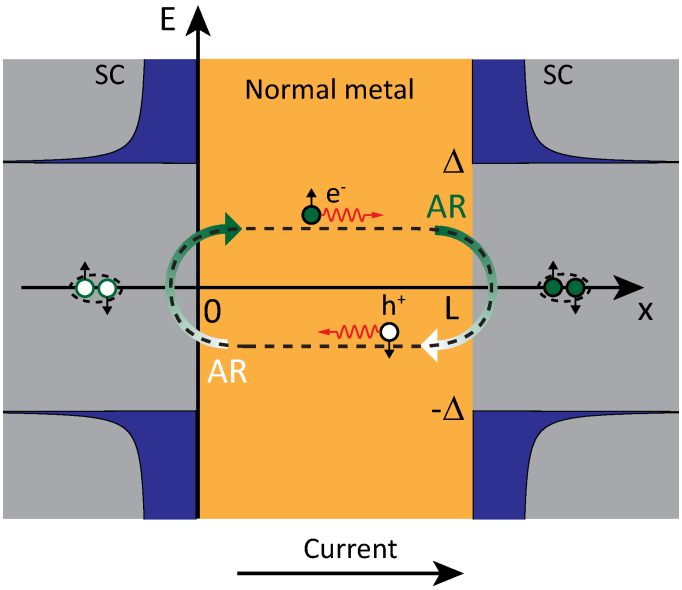

Figure 2.5: **Andreev bound state formation inside a normal metal between two superconductors.** The bound state is a superposition of a right propagating electron and a left propagating hole coupled via Andreev reflections. A complete $e^- \rightarrow h^+ \rightarrow e^-$ cycle entails a charge transfer of $2e$.

an analogy to optics, the SN boundary can be regarded as a mirror reflecting perfectly electron waves as their phase-conjugate hole. Placing two mirrors opposite each other results in a Fabry-Perot cavity where, assuming phase coherence is preserved, the constructively interfering forward and backward traveling waves form bound states with discrete energies.

Similarly, when a normal conductor is sandwiched between two superconductors, an electron starting in the normal conductor propagating to the right reflects from the right SN interface as a hole, which then reflects back as an electron from the left SN interface completing the cycle (Figure 2.5). The condition for bound state formation is that after a full cycle of the electron-hole the phase gained is an integer multiple of 2π. If the condition is met a bound state is formed in the system, called Andreev bound state (ABS). Note that this cycle is accompanied by a transfer of charge $2e$ from the left to the right superconductor guaranteed by the properties of AR.

Although one can calculate the energies of the ABS by matching the phase of the incoming and outgoing electron after a full cycle, in this section we will adopt the scattering matrix approach, which is equivalent and more readily adaptable for other nanostructures.

2.3.2. CALCULATING ABS USING THE SCATTERING MATRIX APPROACH

The Landauer-Büttiker scattering approach[9] was first adopted to Josephson junctions by Beenakker and Van Houten [10] to calculate the energies of the ABS for a general one-dimensional SXS junction, where X is an infinitely short conductor with zero pairing

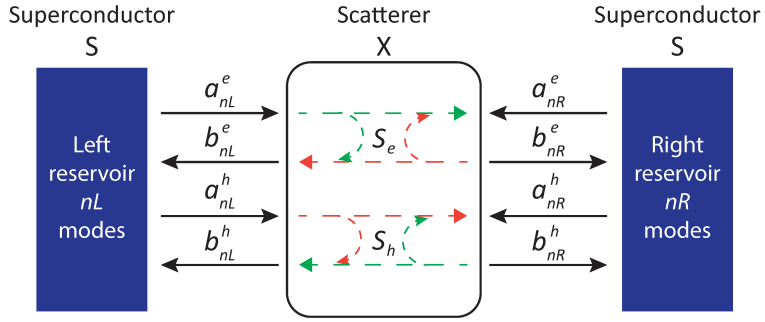

Figure 2.6: **Scattering model of the Josephson junction.** The junction is a point scatterer X described by matrices $S_{e,h}$, which couple the incident to the reflected modes of the left and right superconducting reservoirs.

amplitude and a finite transmission t.

Consider the configuration presented in Figure 2.6 : let $a^{e(h)}_{nL}$ denote the electron(hole) modes emerging from the left reservoir incident on the scatterer and $b^{e(h)}_{nL}$ the modes reflected from the scatterer back to the left reservoir. Similarly let $a^{e(h)}_{nR}$ and $b^{e(h)}_{nR}$ denote the electron (hole) modes emerging from and reflected to the right reservoir. The scattering matrix $S_e(\epsilon)$ then relates the incident and reflected electron modes via the equation

$$\begin{pmatrix} b^e_{nL} \\ b^e_{nR} \end{pmatrix} = S_e(\epsilon) \cdot \begin{pmatrix} a^e_{nL} \\ a^e_{nR} \end{pmatrix} \tag{2.20}$$

and similarly for holes

$$\begin{pmatrix} b^h_{nL} \\ b^h_{nR} \end{pmatrix} = S_h(\epsilon) \cdot \begin{pmatrix} a^h_{nL} \\ a^h_{n}R \end{pmatrix} \tag{2.21}$$

The scattering matrices **for each mode** $S_{e(h)}$ can be written in terms of the transmission t and reflection coefficient $r^{(\prime)}_{e(h)} = 1 - t^{(\prime)}_{e(h)}$:

$$S_{e(h)} = \begin{pmatrix} r_{e(h)}(\epsilon) & t_{e(h)}(\epsilon) \\ t'_{e(h)}(\epsilon) & r'_{e(h)}(\epsilon) \end{pmatrix}$$

The scattering matrix must be subject to the symmetry relations warranted by the system Hamiltonian:

- Time-reversal symmetry ensures

$$S_{e(h)}(\epsilon) = S^{\dagger}_{e(h)}(\epsilon).$$

- Particle-hole symmetry and spin-degeneracy guarantees

$$S_e(\epsilon) = \overline{S_h}(-\epsilon).$$

The equation for electrons and holes combined is:

$$\begin{pmatrix} b^e_{nL} \\ b^e_{nR} \\ b^h_{nL} \\ b^h_{nR} \end{pmatrix} = S_N \cdot \begin{pmatrix} a^e_{nL} \\ a^e_{nR} \\ a^h_{nL} \\ a^h_{nR} \end{pmatrix} \tag{2.22}$$

$$S_N = \begin{pmatrix} S_e & \mathbf{0} \\ \mathbf{0} & S_h \end{pmatrix}$$

We can write down the Andreev scattering matrix S_A for incident electron (hole) states $b^{e(h)}_{nL}, b^{e(h)}_{nR}$ and reflected electron(hole) states $a^{e(h)}_{nL}, a^{e(h)}_{nR}$ using the AR probability amplitude $\lambda(\varphi, E)$ of a pure electron state reflecting as a hole from an NS interface calculated in 2.2.2[5]:

$$\begin{pmatrix} a^e_{nL} \\ a^e_{nR} \\ a^h_{nL} \\ a^h_{nR} \end{pmatrix} = S_A \cdot \begin{pmatrix} b^e_{nL} \\ b^e_{nR} \\ b^h_{nL} \\ b^h_{nR} \end{pmatrix} \tag{2.23}$$

(2.24)

$$S_A = a\left(\frac{E}{|\Delta|}\right) \begin{pmatrix} \mathbf{0} & & \mathrm{I}_{nL}e^{-i\varphi_L} & \mathbf{0} \\ & & \mathbf{0} & \mathrm{I}_{nR}e^{-i\varphi_R} \\ \mathrm{I}_{nL}e^{i\varphi_L} & \mathbf{0} & & \\ \mathbf{0} & \mathrm{I}_{nR}e^{i\varphi_R} & \mathbf{0} & \end{pmatrix} \tag{2.25}$$

I_n is the $n \times n$ identity matrix and φ_L and φ_R are the superconducting phases of the left and right reservoir.

For resonance to occur an incident wave $a_{in} = (a^e_{nL}, a^e_{nR}, a^h_{nL}, a^h_{nR})$ has to satisfy the condition $a_{in} = S_A S_N a_{in}$.

For each channel there are two spin-degenerate Andreev bound state solutions with energies $\pm E_A$ that satisfy the equation

$$\mathrm{Det}[I - S_A S_N] = 0 \tag{2.26}$$

The result is:

$$\pm E_{A\sigma} = \pm\Delta\sqrt{1 - t\sin^2\left(\frac{\varphi}{2}\right)} \quad \text{for } 0 < t < 1 \tag{2.27}$$

$$\pm E_{A\sigma} = \pm\Delta\cos\left(\frac{\varphi}{2}\right) \quad \text{for } t = 1 \tag{2.28}$$

[5] note that we have inverted the roles of incident and reflected modes a, b since the scatterer is now the superconducting interface on the sides instead of the conductor in the center.

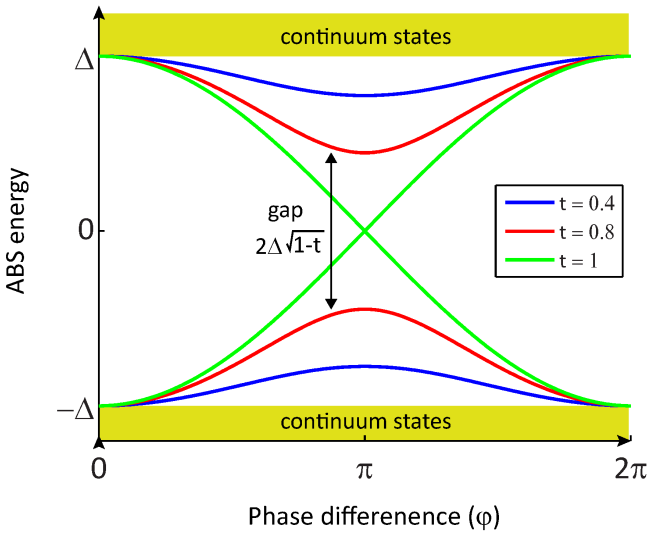

Figure 2.7: **Andreev bound state energies as a function of phase across the junction for different transmission values.** At perfect transmission the ABS carrying opposite current are uncoupled and the superconducting gap closes. For $t < 1$ the ABS pair are coupled via backscattering and a gap opens.

Note that we only considered here the ABS with energies inside the gap, which are bound and spatially localized over a distance of the order of the coherence length. However the Hamiltonian also allows for a continuum of solutions with energies outside the superconducting gap in the continuum. Contrary to the ABS these continuum states are propagating wave solutions and are delocalized. In addition in the short junction limit they do not depend on the phase difference[10].

In Figure 2.7 we plot the energies $\pm E_{A\sigma}$ of the pair of ABS as a function of the phase difference for transmission values $t = 1, 0.8, 0.4$. Each ABS pair of fixed transmission correspond to two spin-degenerate states carrying current in opposing directions.

For $t = 1$, the states $+E_{A\sigma}$ and $-E_{A\sigma}$ are uncoupled and equal at $E = 0$. The ABS energies can take any value within the gap. For $t < 1$, backscattering in the normal region creates a coupling between the ABS of opposite current flow. The coupling causes an effective anticrossing and a finite energy gap of size $2\Delta\sqrt{1-t}$ opens in the spectrum.

The ground state of this SXS system is built in the same fashion as for the system with spatially invariant pairing amplitude (in other words a bulk superconductor) by populating the vacuum state with Bogoliubons of negative energy $|\mathrm{GS}\rangle = \left(\prod_{E^i<-\Delta} \gamma^\dagger_{E^i}\right)\gamma^\dagger_{-E_A}|\mathrm{V}\rangle$. Its parity is even and the total spin is zero. The energy of the grounds state is

$$E_{GS} = \frac{1}{2}\left(-E_A(\varphi) + \sum_{E^i<-\Delta} E^i\right). \tag{2.29}$$

Here $\gamma^\dagger_{E^i}$ and E^i are the continuum operators and continuum energies of the states

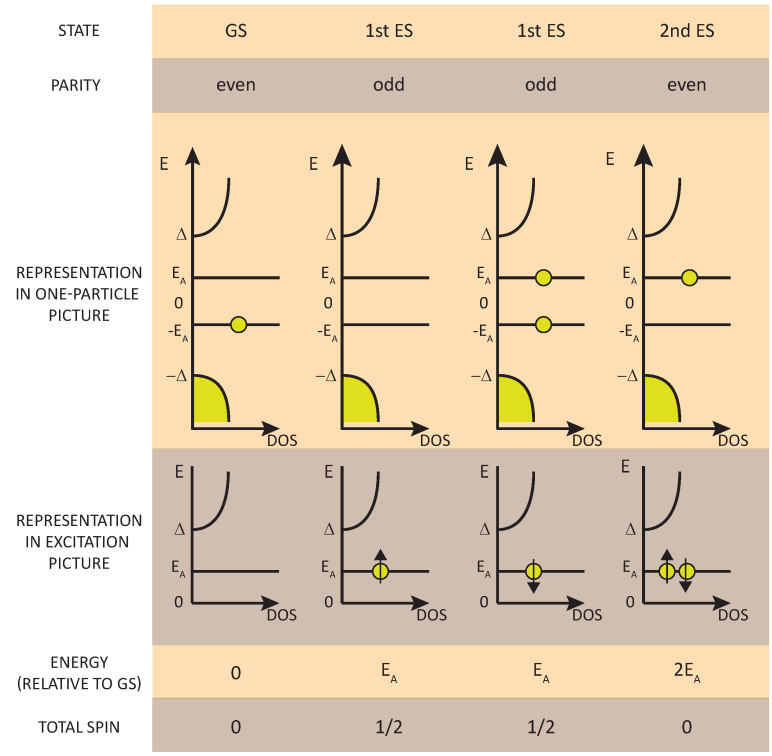

Figure 2.8: **The four basis states of the Andreev two-level system.** The energy levels are represented for a fixed phase $0 < \varphi < 2\pi$. Figure taken from [5].

the condensation energies[6] of which are larger than Δ in absolute value. Contrary to a uniform superconductor, the energy of the ground state is dependent on the phase difference between the two bulk superconductors φ.

In the one-particle picture, the four states consituting the **Andreev two-level system** are written

$$\begin{aligned} &|\mathrm{GS}\rangle, \\ &\gamma^\dagger_{E_A}|\mathrm{GS}\rangle, \\ &\gamma_{-E_A}|\mathrm{GS}\rangle, \\ &\gamma^\dagger_{E_A}\gamma^\dagger_{-E_A}|\mathrm{GS}\rangle, \end{aligned} \tag{2.30}$$

with energies 0, E_A, E_A and $2E_A$ respectively relative to the ground state.

However, the spin quantum number is hidden in the one-particle notation. It is possible to rewrite the four states above by using operators involving spin: $\gamma^\dagger_{E_A\uparrow} \equiv \gamma^\dagger_{E_A}$, $\gamma^\dagger_{E_A\downarrow} \equiv \gamma_{-E_A}$. Thus in the excitation picture the four states are written:

[6] We have not derived the continuum states here.

$$\begin{aligned} |\mathrm{GS}\rangle &\equiv |-\rangle, \\ \gamma^{\dagger}_{E_A\uparrow}|\mathrm{GS}\rangle &\equiv |\uparrow\rangle, \\ \gamma^{\dagger}_{E_A\downarrow}|\mathrm{GS}\rangle &\equiv |\downarrow\rangle, \\ \gamma^{\dagger}_{E_A\uparrow}\gamma^{\dagger}_{E_A\downarrow}|\mathrm{GS}\rangle &\equiv |+\rangle, \end{aligned} \tag{2.31}$$

In Figure 2.8 we show these four states using both representations along with their energy, parity and spin. Although we also plotted the continuum states, when the weak-link has low transmission $t < 1$ or the phase difference $\varphi \approx \pi$, the ABS energies $|E_A| \ll \Delta$ and the continuum states can be neglected.

2.3.3. CURRENT CARRIED BY THE ABS

The current I_A carried by each ABS of energy $\pm E_A$ is [10] :

$$I_A(\varphi,\tau) = -\frac{2e}{\hbar}\frac{dE_A}{d\varphi} = \frac{e\Delta}{2\hbar}\frac{t\sin(\varphi)}{\sqrt{1-t\sin^2\left(\frac{\varphi}{2}\right)}} \tag{2.32}$$

This result is valid for a one-dimensional short junction[7] bearing a single transmission channel.

Note that in this limit the current is independent of the junction's dimension and characterized only by the phase difference φ, the transmission t and the pairing amplitude Δ in the leads.

The energies of the two ABS levels $E_{A\pm}(= +E_A, -E_A)$ satisfy $E_{A+}(\varphi) = -E_{A-}(\varphi)$ and hence by virtue of 2.32 carry supercurrent of equal magnitude and opposite direction. Thus the ground state($|-\rangle$) and the even excited state($|+\rangle$) carry finite supercurrent whereas the two odd states ($|\uparrow\rangle, |\downarrow\rangle$) do not carry any (since in the odd state both or neither ABS levels are populated).

For a weak link with multiple modes $N > 1$, since Andreev reflection does not mix the different modes, each mode can be regarded as an independent junction hosting a single pair of ABS $E_{A\pm}(\varphi, t_i)$ (where the t_i are the transmission values of each mode). The total current $I(\varphi)$ is the sum of the contribution of each occupied mode:

$$I(\varphi) = \frac{e\Delta}{2\hbar}\sum_{i=1}^{N}\frac{t_i\sin(\varphi)}{\sqrt{1-t_i\sin^2\left(\frac{\varphi}{2}\right)}} \tag{2.33}$$

2.3.4. CURRENT-PHASE RELATION AND THE DC JOSEPHSON EFFECT IN A TUNNEL JUNCTION

One of the most important characteristic of a JJ is its current phase relation (CPR) that relates the phase difference between the two Cooper pair condensates interrupted by the junction and the magnitude of the supercurrent flowing across. The supercurrent is transported by the ABS through the junction. In 2.33 we derived the current passing through a JJ admitting N modes each with transmission t_i and a phase difference φ across the junction.

[7] the short junction limit holds when the junction length L is smaller than the coherence length $\xi = \frac{\hbar v_F}{\Delta} < L$)

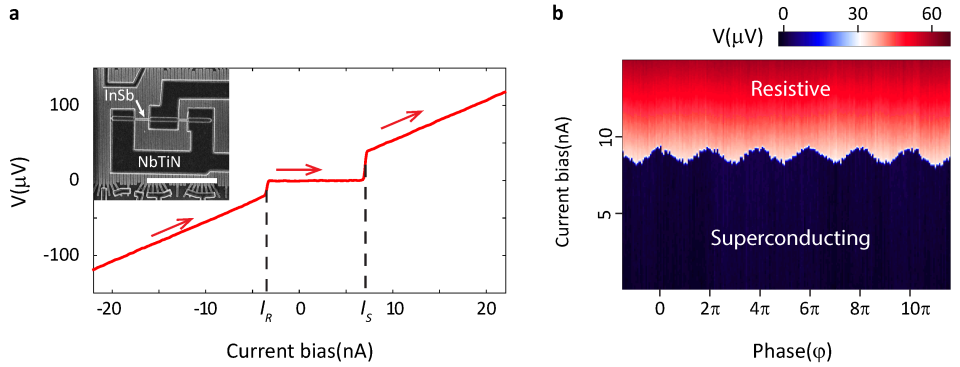

Figure 2.9: **Transport through JJs. a,** Typical IV curve for a current biased JJ. Current sweep direction is shown along with the retrapping current I_R and switching current I_S. **b,** Sinusoidal modulation of the critical current of a JJ. Phase biasing is done via a DC-SQUID configuration.

The tunnel junction limit assumes many modes with low transmission, i.e. $N \to \infty$ and $t_i \to 0$. In this limit 2.33 becomes (note that by definition $\sum^N t_i = 1$)

$$I(\varphi) = \lim_{N\to\infty, t_i\to 0} \left(\frac{e\Delta}{2\hbar} \sum_{i=1}^{N} \frac{t_i \sin(\varphi)}{\sqrt{1 - t_i \sin^2\left(\frac{\varphi}{2}\right)}} \right)$$
$$\Rightarrow I(\varphi) = I_C \sin\varphi \tag{2.34}$$

with $I_C = e\Delta/2\hbar$. Equation 2.34 is called the **dc Josephson effect**, or the first Josephson equation. It is applicable to a very wide range of junctions of different geometry and material.

The Hamiltonian of the Josephson tunnel junction can be written as:

$$H_J = -E_J \cos(\varphi) \tag{2.35}$$

where $E_J = \frac{\hbar I_C}{2e}$.

From 2.34 we can deduce the behavior of a JJ when current biased: the junction can admit supercurrent up to a maximal value I_S, above which the junction becomes resistive and a finite voltage drop appears. When the phase over the junction is not restricted (such as in a simple two terminal measurement) $I_S = \max|\mathrm{CPR}(\varphi)| = I_C$ at zero temperature. A typical V-I curve is presented in Figure 2.9**a** where the JJ is made of NbTiN superconducting leads while an InSb nanowire acts as the weak link.

When the junction is phase biased (for example by embedding it in a dc-SQUID loop), the switching current is sinusoidally modulated by the phase as expected from 2.34 (see Figure 2.9**b**).

Note that the general expression for an N-mode JJs CPR 2.33 can be expanded in terms of sinusoidal harmonics(this is true for any set of transmission values t_i, the tunnel

junction limit need not to hold) :

$$I(\varphi) = \frac{e\Delta}{2\hbar}\sum_{i=1}^{N}\frac{t_i \sin(\varphi)}{\sqrt{1 - t_i \sin^2\left(\frac{\varphi}{2}\right)}} \tag{2.36}$$

$$= \sum_{n=1}^{\infty} I_C^n \sin(n\varphi) \tag{2.37}$$

While the second expression is just a mathematical expansion in terms of sinusoidal harmonics, it is useful for JJs which show slight deviation from the ideal tunnel junction behavior and hence can be well approximated by the first few harmonics.

2.4. JOSEPHSON JUNCTIONS IN MAGNETIC FIELD AND THROUGH A QUANTUM DOT - π AND φ_0 JUNCTIONS

2.4.1. ABS WITH FINITE ZEEMAN ENERGY

For Josephson junctions where the weak link is a nanowire such as InSb or InAs, the spin degeneracy of the ABS can be lifted with the application of an external magnetic field. The Hamiltonian of the nanowire section, neglecting spin-orbit coupling and magnetic orbital effects, is

$$H_{nanowire} = \frac{\mathbf{p}^2}{2m} + V_{scatter} + \frac{1}{2}g\mu\mathbf{B}\cdot\hat{\sigma} \tag{2.38}$$

The authors of Reference [11] calculate the energies of the ABS as a function of increasing magnetic field. This is accounted for by an extra phase $\pm\theta_B = \frac{|g|\mu B}{\hbar v_F}L = \frac{E_Z}{E_{Th}}$ picked up by the propagating electron-hole wave [8] residing in the weak link of length L.

The ABS energies of the above Hamiltonian sandwiched between two superconductors separated by a phase φ are calculated for increasing magnetic field and plotted in Figure 2.10. Working in the short junction limit in the Nambu basis, for any phase φ there are always exactly four Andreev bound state solutions situated within the superconducting gap $-\Delta \leq E_{A\uparrow,\downarrow\pm} \geq \Delta$. Each solution has a definite spin which we labelled on the figure. The degeneracy $E_{A\uparrow\pm} = E_{A\downarrow\pm}$ holding in the absence of magnetic field (panel **a**) is broken at finite field, where $E_{A\downarrow\pm} > E_{A\uparrow\pm}$. Particle-hole symmetry of the BdG equations still guarantee $E_{A\uparrow\mp} = -E_{A\downarrow\pm}$.

As for any superconducting system, the ground state is obtained by populating the states below the Fermi level ($E=0$ here). In Figure 2.10 the occupied levels of the ground state are highlighted in red for each specific value of the magnetic field. The ground state supercurrent is the phase derivative summed over each occupied level and is plotted in Figure 2.10**g** for four magnetic field values presented in **a-f**.

One can identify three regions of θ_B values. For low magnetic fields (Figure 2.10**a, b**) the energy levels do not intersect (region I). The ground state energy is $E_{GS} = -\frac{1}{2}(E_{A\uparrow+} + (E_{A\downarrow+})$ and the minimum energy is found at $\varphi = 0$. The current is roughly a sine function, $I(\varphi) \sim \sin\varphi$.

[8] The acquired phase is positive for a spin-up electron or spin-down hole and negative for spin-down electron or spin-up hole

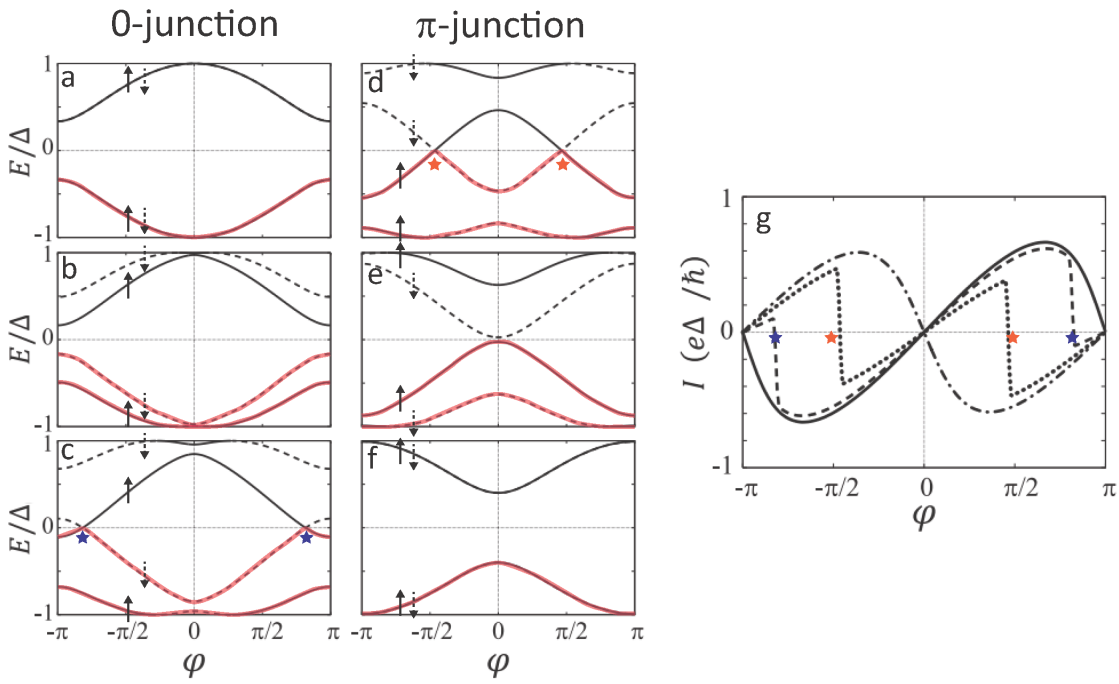

Figure 2.10: **ABS of a short nanowire SNS junction with a single channel as a function of magnetic field. a-f,** Each pannel shows $E_{A\uparrow\pm}(\varphi)$(solid lines) and $E_{A\downarrow\pm}(\varphi)$ (dashed lines) vs phase φ. The different panels represent increasing magnetic field θ_B. From top left to bottom right the values are $0, 0.1\pi, 0.27\pi, 0.53\pi, 0.79\pi, \pi$. For $\theta_B > \pi$ the junction ground state is found at $\varphi = \pi$ and are in the π-state. The populated levels in the ground state are marked red. **g,** CPR of the junction with energies plotted in (a)(full line), (c)(dashed line), (d)(dotted line) and (f)(dashed-dotted line). Figure reused from [12]

As the magnetic field is increased there is an energy level crossing $E_{A\uparrow+} = E_{A\downarrow-} = 0$ which moves from $\varphi = \pm\pi$ to $\varphi = 0$ (region II). The crossings at zero, denoted by a star in Figure 2.10, warrants a discontinuity in the gradient of E_{GS} and a jump in the current-phase relation. The global energy minimum jumps suddenly from $\varphi = 0$ to $\varphi = \pi$ at $\theta_B \sim \pi/2$, which is called a 0-π transition. Thus for magnetic field $\theta \gtrsim \pi/2$ the new ground state is found at $\varphi = \pi$ and the junction is dubbed a **"π-junction"**: *a junction of which the energy minimum is found at phase $\varphi = \pi$.*

As the field reaches $\theta_B \approx \pi$ the energy crossing disappears and the same energy levels are recovered as for the zero field case, but shifted by phase π. This is reflected in the current-phase relationship $I(\varphi) \sim -\sin\varphi$, a characteristic of the π-junction.

Why is the 0-π transition a sudden jump and not a continuous transition? This is guaranteed by the symmetries of the Hamiltonian: H in 2.38 satisfies $KHK^{-1} = H$ where K is the complex conjugation operator, which guarantees that all Andreev levels are even in phase $E_A(\varphi) = E_A(-\varphi)$ and no φ (other that 0 or π) can give an absolute minimum in energy.

Although we only considered a 1-D system with a single conduction channel, authors of Reference[12] show that the many channel system is qualitatively similar.

2.4.2. ANDREEV BOUND STATES FOR AN S-QD-S SYSTEM

So far we have considered S-X-S junction where X was an infinitely short one dimensional constriction characterized by a single parameter t per transmission channel. We now discuss how the ABS spectrum changes if X is a quantum dot instead (QD).

GENERAL HAMILTONIAN FOR AN S-QD-S SYSTEM

A quantum dot is a confinement of charge carriers which behaves like an artificial atom: its energy eigenstates form a discrete set of levels seperated by energy $\delta\epsilon$[13]. When $\delta\epsilon$ is large compared to other energies of the system, the quantum dot Hamiltonian H_{QD} can be modelled by the "Anderson impurity model"[14]: a single spin-degenerate level of energy ϵ_0, with charging energy U, which is the cost of double occupation and takes into account electron-electron interactions.

$$H_{QD} = \sum_\sigma \epsilon_0 d^\dagger_{0\sigma} d_{0\sigma} + U n_{0\uparrow} n_{0\downarrow} \tag{2.39}$$

where $d^\dagger_{0\sigma}$ creates an electron of spin σ on the level and $n_{0\sigma} = d^\dagger_{0\sigma} d_{0\sigma}$ is the number operator. The Hamiltonian of the left and right leads $H_{\nu=L,R}$ with superconducting phase φ_ν takes the usual BCS form with pairing $\Delta_\nu = |\Delta| e^{i\varphi_\nu}$

$$H_\nu = \sum_{k\sigma} \xi_{k,\nu} c^\dagger_{k\sigma,\nu} c_{k\sigma,\nu} + \sum_k (\Delta_\nu c^\dagger_{k\uparrow,\nu} c^\dagger_{-k\downarrow,\nu} + h.c.) \tag{2.40}$$

where $c^\dagger_{k\sigma,\nu}$ creates an electron in lead ν at energy $\xi_{k,\nu}$ referenced from the lead chemical potential μ_ν. The tunneling Hamiltonian H_T describes the tunneling of electrons from the leads on the dot and vice-versa:

$$H_T = \sum_{k\sigma,\nu} (V_{k\sigma,\nu} c^\dagger_{k\sigma,\nu} d_{0\sigma} + h.c.) \tag{2.41}$$

with hopping paramters $V_{k\sigma,\nu}$. Assuming the normal density of state around the Fermi energy in the leads $\rho_\nu(E)$ is constant and the hopping paramters V are independent of momentum k, the tunneling can be described by the tunneling rate $\Gamma_\nu = \pi\rho_\nu^2|V_\nu|^2$.

The Hamiltonian of the whole system is

$$H = H_L + H_R + H_T + H_{QD}. \tag{2.42}$$

STRONG, INTERMEDIATE AND WEAK COUPLING REGIMES

Electron-electron interactions make the Hamiltonian in 2.42 too complex to solve. Approximations are necessary to solve the system analytically or to compute a numerical solution within reasonable time.

Essentially there are two competing forces in a proximitized quantum dot system: firstly, the electrons concentrated on the dot repel and do not want to accept more electrons on the dot. Secondly, superconductivity from the leads couples electrons into pairs and these delocalized Cooper pairs are exchanged with the lead. Thus the charging energy U imposes constant electron number whereas superconductivity Δ favors fluctuating electrons. The rate of exchange of charge is determined by the coupling $\Gamma = \Gamma_L + \Gamma_R$.

We can distinguish between three regimes depending on the value of U,Δ and Γ[15]:

- Strong coupling regime: $\Gamma \gg \Delta, U$. When Γ is the largest energy scale, the superconductor couples well to the quantum dot. Cooper pairs can resonantly tunnel across the dot, causing a fluctuating electron population of the quantum dot. The ABS resemble that of a one dimensional channel with perfect transition and reduced gap when $\epsilon_0 = 0$ (on resonance) and that of a channel with finite transmission off resonance.

- Weakly coupled regime: $\Gamma \ll \Delta, U$. In this regime due to the large charging energy, Cooper pairs cannot tunnel on the dot. Individual electrons constituting the pair can tunnel through the dot with a characteristic time scale h/Γ, much larger than the coherence time h/Δ of Cooper pairs. Thus the electrons tunneling one by one cannot coherently recouple as Cooper pairs and no supercurrent is possible in this regime.

- Intermediately coupled regime: $\Gamma \sim \Delta \sim U$. In the intermediate regime, although electrons tunnel one-by-one from the source to the drain lead through the dot, they can recombine in Cooper pairs and supercurrent is still possible. This happens via a fourth order co-tunneling process, where the initial and final states have the same energy, but electrons can occupy virtual states in between which may be offset in energy. In addition, the charging interaction of the dot is comparable to the superconducting order, and Cooper pairs may acquire a substantial phase while tunneling through.

There is an additional energy scale pertaining to an isolated spin coupled to external reservoirs, called the Kondo energy (or temperaure). The Kondo effect where a single confined spin, such as a quantum dot with half filling of its top most orbital, interacts with the Fermi sea of normal (non-superconducting) conduction electrons via tunnel-coupling through the leads[16]. The lead electrons hop on and off the dot leading to

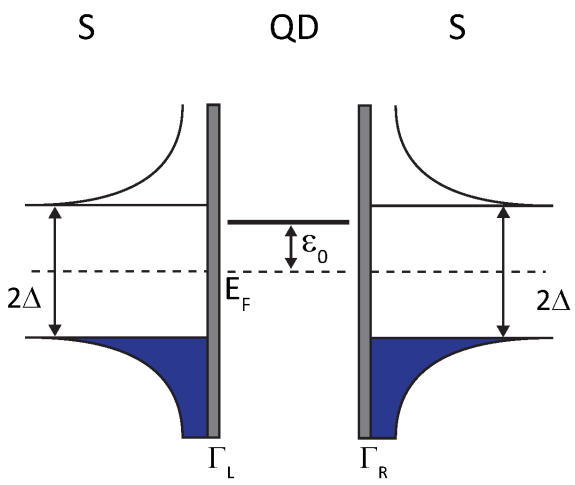

Figure 2.11: **Model of a non-interacting single level QD coupled to superconducting leads.**

spin-exchange with the local moment on the dot, thus creating a many-body spin-singlet ground state. The interplay between the Kondo-effect and superconductivity has been analysed experimentally and theoretically extensively and is beyond the scope of this thesis. Here it is sufficient to mention the Kondo temperature T_K [17], which defines the scale for the Kondo effect to be dominant:

$$T_K = \sqrt{\frac{U\Gamma}{2}} \exp\left(-\frac{\pi|\epsilon_0(\epsilon_0+U)|}{2U\Gamma}\right) \tag{2.43}$$

In the limit $\frac{U}{\Gamma} \gg 1$ the Kondo temperature becomes infinitesimal, since the electrons from the reservoir cannot interact with the isolated spin if tunneling is surpressed, inhibiting the creation of the Kondo state.

NON-INTERACTING APPROXIMATION

The simplest quantum-dot model one can introduce is when electron-electron interactions are neglected ($U = 0$). We are then left with a quantum dot with an orbital level at energy ϵ_0 relative to the Fermi energy of the leads, tunnel coupled to the left and right lead via Γ_L and Γ_R respectively. This simple model is presented in Figure 2.11. Although in general QDs have several orbitals with average level spacing $\delta\epsilon$, this model works in the limit $\Gamma, T \ll \delta\epsilon$ in which case transport occurs only via a single orbital.

The conductance of resonant tunneling of single electrons through a single level is [18]:

$$G = \frac{2e^2}{h} \frac{\Gamma_L\Gamma_R}{\epsilon_0^2 + \frac{1}{4}\Gamma^2} \tag{2.44}$$

The conductance is maximum when the dot level is completely aligned with the Fermi level of the leads. If the superconductivity of the leads can be surpressed, this

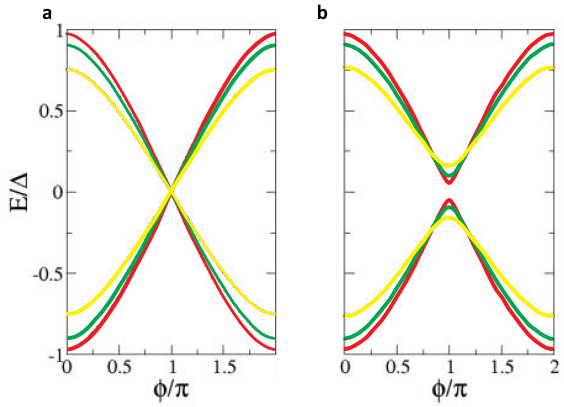

Figure 2.12: **ABS of system consisting of a non-interacting single level QD symmetrically coupled to superconducting leads.** The ABS are calculated for varying values of the tunnel coupling Γ/Δ =1.0(yellow line), 2.0(green), 4.0(red). **a,** Case of dot on resonance $\epsilon_0 = 0$. **b,** $\epsilon_0 = 0.5\Delta$. Figure from [19]

formula is useful to extract the tunnel coupling values from a device for which the differential conductance is measured as a function of gate voltage.

Computing the ABS for a non-interacting QD is straightforwardly done by calculating the normal scattering amplitude through the dot and then meeting the condition for ABS formation, that is gaining a phase of $2\pi n$ for a quasiparticle completing a full trajectory from one lead through the dot and relfecting back as a hole from the other lead. Reference [19] evaluates the ABS energies E in the limit of zero temperature, and assuming symmetric tunnelling ($\Gamma_L = \Gamma_R$) and a dot level on resonance ($\epsilon_0 = 0$) :

$$E \pm \Delta \cos\frac{\varphi}{2} + \frac{E\sqrt{\Delta^2 - E^2}}{\Gamma} = 0. \tag{2.45}$$

In the limit $\Gamma \gg \Delta$ 2.45 reduces to

$$E \approx \pm\tilde{\Delta}\cos\frac{\varphi}{2}, \tag{2.46}$$

where $\tilde{\Delta} = \Delta\left[1 - 2\frac{\Delta^2}{\Gamma^2}\right]$ is the reduced gap parameter. We plot the energies in Figure 2.12**a**. We can see that the ABS of a quantum dot tuned to resonance is gapless and resembles that of a perfectly transmitting tunnel junction 2.28, except that the ABS dispersion are reduced and do not extend all the way to the gap Δ.

When the dot is not tuned to resonance, a gap opens and the ABS energies are similar to a tunnel junction with finite transmission $\tilde{t}$:

$$E \approx \pm\sqrt{1 - \tilde{t}\sin\frac{\varphi}{2}^2}, \tag{2.47}$$

with $\tilde{t} = \frac{1}{1+(\epsilon_0/\Gamma)^2}$ the normal transmission at the Fermi energy. ABS for such a QD are plotted in Figure 2.12**b** for particular values of Γ/Δ.

Thus in the non-interacting limit the ABS through a QD are not modified qualitatively compared to ABS through an SIS JJ, besides reducing the critical current and providing an expeimentally tunable transmission value via ϵ_0 which can be changed via electrostatic gates.

CO-TUNNELING APPROXIMATION

The co-tunneling approach was first introduced by Glazman and Mateev [20]. It relies on computing expectation values of the Hamiltonian 2.42 to the lowest order in the tunnel coupling as a perturbation in Γ. The supercurrent is expressed as

$$I = e\langle \frac{d}{dt}\xi_{k,L} c^{\dagger}_{k\sigma,L} c_{k\sigma,L}\rangle \tag{2.48}$$

which is the expected current through the left lead in 2.40. After adding the co-tunneling events through the virtual levels substantially contributing to the supercurrent (i.e. those of lowest order in Γ), the result is obtained for the current by taking the limit $U \to \infty$ [9]:

$$I(\varphi) = \lambda \frac{e}{\hbar} \frac{\Gamma_L \Gamma_R}{\Delta} F\left(\frac{|\epsilon_0|}{\Delta}\right) \sin\varphi, \tag{2.49}$$

where $\lambda = 2$ for $\epsilon_0 > 0$ (empty dot) and $\lambda = -1$ for $\epsilon_0 < 0$ (singly occupied dot). Thus the supercurrent the dot admits depends on the ground state of the dot. The polarity of λ changes with the dot occupation, signaling a change in direction of the ground state supercurrent, i.e. a transition between 0- and π-junction state as we have seen in the case of a JJ in magnetic field. This phase gain of π for oddly occupied dot states is due the reversal of the electrons making up the Cooper pair while tunneling through[21].

Note that the CPR is sinusoidal in the co-tunneling limit as for a low transmission tunnel junction and the magnitude of the current is of order $I \sim \Gamma^2$ since transferring a Cooper pair between the electrodes involves the phase-coherent tunneling of two electrons.

SIMPLIFIED WEAKLY INTERACTING MODEL TREATING INTERACTION AS CONSTANT

So far we have viewed models of superconducting quantum dots where the interaction term U was either neglected or treated in the limit $U \to \infty$. The next simplest step is to transform the many-body Hamiltonian 2.42 to a single particle form.

Consider the Hamiltonian of the isolated single orbital dot 2.39. Such a dot has four eigenstates: the empty state $|0\rangle$ with energy 0, the two single electron states $|\uparrow\rangle$ and $|\downarrow\rangle$ with energy ϵ_0 and the double occupies state $|\uparrow\downarrow\rangle$ with energy $\epsilon_0 + U$. The alternative QD Hamiltonian

$$\tilde{H}_{QD} = \sum_{\sigma} \epsilon_\sigma d^{\dagger}_{0\sigma} d_{0\sigma} \tag{2.50}$$

$$\begin{cases} \epsilon_\uparrow = \epsilon_0 - U/2 \\ \epsilon_\downarrow = \epsilon_0 + U/2 \end{cases}$$

[9] the function $F(x)$ is defined as $F(x) = \frac{1}{\pi^2} \int \frac{dt_1\, dt_2}{(\cosh t_1 + \cosh t_2)(x + \cosh t_1)(x + \cosh t_2)}$

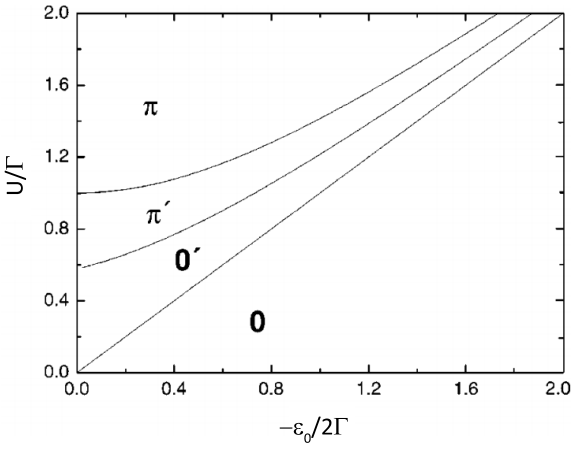

Figure 2.13: **Phase diagram of an S-QD-S junction calculated for coupling $\Gamma/\Delta = 1$ using a constant interaction model.** The dot changes between a 0 and a π state depending on the level energy and charging energy. Simulations taken from Reference[22].

has the same eigenstates and energies but is of single-particle form. The interaction is now treated to be a constant U, the energy difference of a filled and a half-empty dot[10].

Substituting $\tilde{H}_{QD}$ for H_{QD} into 2.42 we obtain a non-interacting one-particle approximation of the full interacting QD Hamiltonian. This model was introduced in [22, 23] and is equivalent to a single-level quantum dot with Zeeman exchange interaction $E_{ex} \equiv U/2$: $\epsilon_{0\sigma} = \epsilon_0 + \sigma E_{ex}$. Thus the effect of charging is very similar to the effect of an external magnetic field.

In Figure 2.13 we present the phase diagram obtained via this model in [23] for the case of symmetric tunneling ($\Gamma_L = \Gamma_R = \Gamma/2$) in the limit $\Delta \ll \Gamma$. Similarly to the magnetic ABS case in section 2.4.1, the superconducting quantum dot ground state changes between the 0-junction and π-junction case with global energy minimum at phase difference $\varphi = 0$ and $\varphi = \pi$ respectively. There are also two intermediary states $0'$ and π' where ABS energies intersect at the Fermi level: the $0'(\pi')$ state has a global energy minimum at $\varphi = 0(\varphi = \pi)$ as well as a metastable energy minimum at $\varphi = \pi(\varphi = 0)$.

The boundaries of each phase is calculated by the authors:

- 0-$0'$ phase transition: $U = -2\epsilon_0$.
- $0'$-π' phase transition: $U = \frac{4}{3}(\epsilon_0/2 + \sqrt{3\Gamma^2 + \epsilon_0^2})$
- π'-π phase transition: $U = 2\sqrt{4\Gamma^2 + \epsilon_0^2}$

Note that a necessary (but not sufficient) condition for the QD JJ to be in the π-junction state is that the bare, uncoupled dot be occupied by a single electron ($U/2 - \epsilon_0 > 0$).

[10] Although the arbitrariness of choosing which spin-state is of lower energy, this does not play a role when calculating physically measurable observables such as the Josephson supercurrent or tunnel density of states.

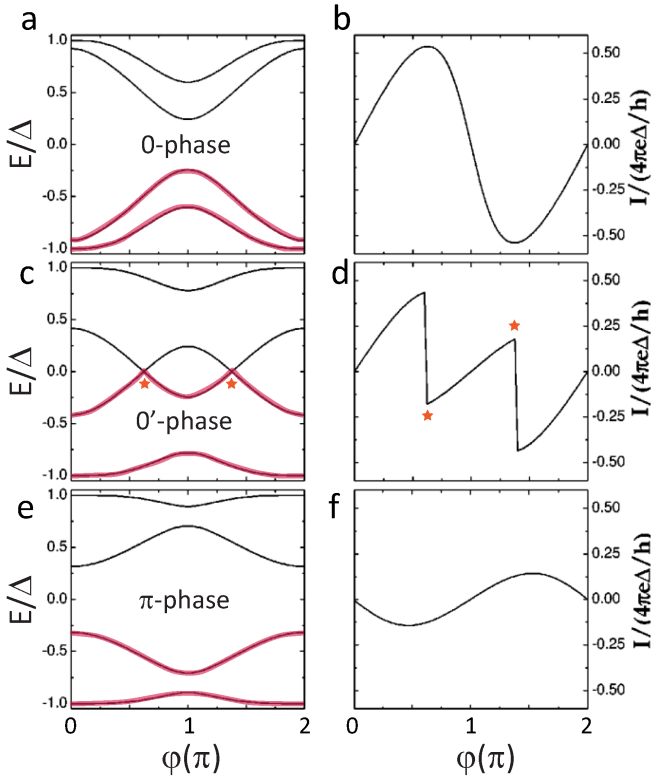

Figure 2.14: **Evolution of the ABS and CPR of a S-QD-S junction using a simplified constant interaction Anderson model.** Simulations taken from Reference[23]. The authors used parameter values $\epsilon_0/\Gamma = -0.5$ for the level energy and increasing charging energy $U = -\epsilon_0$ (panel **a, d**), $-3\epsilon_0$ (panel **b, e**) and $-6\epsilon_0$ (panel **c, f**).In each panel we denote the junction's phase and mark with red the energy levels populated in the ground state. The orange stars mark the point in phase where the ground state energy has a kink due to the change of ABS branch, causing a jump in the CPR.

In Figure 2.14 we show the ABS energies calculated as a function of phase as well as the CPR when $\epsilon_0 = -\Gamma$. The emergence of these alternative ground state phases are now explicit:

- Figure 2.14**a,b** show the energies and CPR of the junction in the 0-phase when $U = -\epsilon_0$. The ABS do not cross the Fermi level resulting in an energy gap. The only energy minimum is found at $\varphi = 0$ ("0-junction"). The CPR is continuous with current flowing in direction of the phase bias for small phase, similar to a single channel JJ with an infinitely small tunnel barrier with finite transmission 2.32.

- Figure 2.14**c, d** show the energies and CPR of the junction in the 0'-phase when $U = -3\epsilon_0$. The local energy maximum turns into a minimum at $\varphi = \pi$, but the global minimum is still found at $\varphi = \pi$. The intersecting ABS warrants a change in the ABS branch of the junction ground state as the phase is ramped, causing a jump in the CPR.

- Figure 2.14**e, f** show the energies and CPR of the junction in the π-phase when $U = -6\epsilon_0$. The ABS no longer intersect and a gap in the energy spectrum opens again. The energy has a single minimum found at $\varphi = \pi$. The CPR reflects this π shift, but the critical current is less than for the 0-junction since the increase in U has reduced the dispersion of the ABS.

Overall the behavior of the S-QD-S junction with charging energy U is qualitatively similar to S-X-S juntion with Zeeman splitting E_{ex}, visible by comparing Figure 2.10 and 2.14. Increasing U (E_{ex}) results in a splitting of the ABS, which first intersect at the Fermi level and then flip, causing a π-junction.

Experimentally, however, the charging energy U is not an easily tunable parameter, since it depends on the capacitance of the dot to the environment which is determined by the sample geometry. On the other hand the orbital energy ϵ_0 is easily tunable with electrostatic gating. The π-junction then arises in the middle of each odd diamond where the $\epsilon_0 < U/2$ condition is met.

π-junctions in quantum dots were measured in single junction carbon nanotubes[24] and SQUIDs[25, 26], as well as in nanowire SQUIDs [21]. A controllable $0'$ and π'-junction in a carbon nanotube SQUID, where the 0 to π transition is induced by winding the phase, was also recently reported [27].

2.4.3. ANOMALOUS CURRENT AND THE φ_0-JOSEPHSON JUNCTION

ANOMALOUS CURRENT AND SYMMETRIES

Anomalous current in the context of Josephson junctions is defined as the current flowing through the junction when there is no phase difference between the superconducting leads: $I_{anomalous} \equiv I(\varphi = 0)$. This current is dubbed anomalous because in usual situations it vanishes, due to symmetries respected by JJ Hamiltonian. In 1-D (or 0-D), these are time reversal symmetry and chiral symmetry [28].

The current throught the system must respect the same symmetries as the Hamiltonian. If the Hamiltonian respects time reversal symmetry, the current $I(\varphi)$ must equal to its time reversal counterpart:

$$I(\varphi) = -I(-\varphi) \tag{2.51}$$
$$\Rightarrow I(0) = (0)$$

2

If the Hamiltonian respects chiral symmetry, i.e. equivalence between left and right handedness, the current must satisfy

$$I(\varphi) = I(-\varphi) \tag{2.52}$$
$$\Rightarrow I(0) = (0)$$

Thus the anomalous current vanishes in case either time reversal or chiral symmetry holds.

Let's assume a generalized sinusoidal current phase relationship for the junction, where the minimum energy is shifted by an angle φ_0, called a φ_0**-junction**.

$$I(\varphi) = \sin(\varphi + \varphi_0).$$

The presence of either time reversal or chiral symmetry implies $\varphi_0 = 0, \pi$.

This is why, as we have seen in previous sections, the presence of magnetic field or charging energy can change the global energy minimum from $\varphi = 0$ to $\varphi = \pi$, but it can take no values in between, since it would imply an anomalous current flow. Conversely, the presence of an anomalous current directly implies a φ_0-junction with $\varphi_0 \neq 0, \pi$.

COMPLEX TUNNELING AMPLITUDE IMPLIES ANOMALOUS CURRENT

Now let's assume a generalized JJ which allows for anomalous current to flow and write the CPR as a sum of a standard '0-junction' and an anomalous current term:

$$I(\varphi) = I_0 \sin(\varphi) + I_{anomalous} \cos(\varphi) \tag{2.53}$$

Let's describe this junction in the simplest tunnel junction model where the barrier is characterized by single, but not necessarily real tunneling coefficient T. Assume phase φ_L and wavefunction $\psi_L = |\psi_L| e^{i\varphi_L}$ in the left lead and phase φ_R and wavefunction $\psi_R = |\psi_R| e^{i\varphi_R}$ in the right lead, with $\varphi = \varphi_L - \varphi_R$.

We use Feyman's derivation [29] to compute I_0 and $I_{anomalous}$ in terms of T.

Assuming weak coupling between the two superconductors, the Schrödinger equation in the left lead and right lead can be written

$$i\hbar \frac{\partial}{\partial t} \psi_L = \mu_L \psi_L + T \psi_R \tag{2.54}$$
$$i\hbar \frac{\partial}{\partial t} \psi_R = \mu_R \psi_R + T \psi_L \tag{2.55}$$

where $\mu_{L,R}$ is the chemical potential in the left and right leads. Solving these two equations for the current I gives

$$I \sim |\psi_L||\psi_R| \left(\Re(T) \sin\varphi + \Im(T) \cos\varphi \right) \tag{2.56}$$

Thus $I_0 \sim \Re(T)$ and $I_{anomalous} \sim \Im(T)$. A complex tunneling amplitude between the leads implies an anomalous current flowing at zero phase difference.

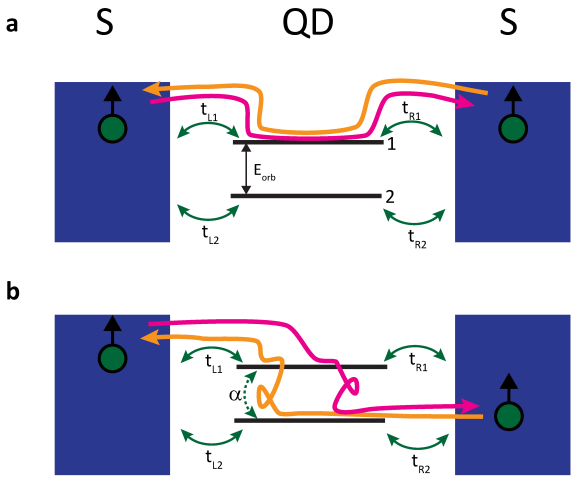

Figure 2.15: **Electron of a Cooper pair tunneling across a quantum dot with two orbitals. a,**The spin-up electron tunnels through the dot via orbital 1. Leftward (orange arrow) and Rightward(purple arrow) tunneling has the same amplitude giving no anomalous current. **b,** When SOI couples the two orbitals, the spin-up electron can tunnel via orbital 1 and 2. Leftward and righward tunneling now acquires different phases and do not cancel. We have omitted drawing the spin-down electron for clarity.

ANOMALOUS CURRENT IN S-QD-S SYSTEM WITH ZEEMAN AND SPIN-ORBIT INTERACTION

To obtain an anomalous current flowing through a JJ, one needs to break both time reversal symmetry and chiral symmetry. In order to break these symmetries in a quantum dot connected to superconducting leads, it is necessary for the dot to have two orbitals taking part in transport, coupled by spin-orbit interaction(SOI) and Zeeman split by a magnetic field[30]. The Zeeman splitting lifts the time reversal symmetry. The spin-orbit interaction results in an intrinsic net magnetic field $\mathbf{B_{SO}}$, perpendicular to both the electron momentum and local electric field gradient. The combination of $\mathbf{B_{SO}}$ and $\mathbf{B}$ pointing in a suitable direction provides a complex tunneling amplitude and lifts the chiral symmetry of the S-QD-S system as we shall see below.

We depict the system in Figure 2.15 and label the two orbitals of the quantum dot 1 and 2. The energy splitting between the orbitals is E_{orb} and the hybridization amplitude between between orbital i and lead X is labelled t_{Xi}.

To see how an anomalous current can flow in such a system, we assume the co-tunneling limit holds where the electrons forming the Cooper pair tunnel through the dot one by one and the total tunneling amplitude is the product of the individual electron amplitudes. We'll see that this tunneling amplitude will be complex at phase difference $\varphi = 0$, guaranteeing an anomalous current (see previous section).

Without SOI the individual electrons forming the Cooper pair tunnel through the QD via a single orbital level (although not necessarily the same orbital), since nothing couples the orbitals together. For example, consider the spin-up electron of the Cooper pair tunneling rightward, from the left lead to orbital 1 on the dot to the right lead(purple arrow in Figure 2.15**a**). The corresponding tunneling coefficient (matrix element) for this

process is given by $(t_{L1}\, t_{R1})$. Suppose the spin-down electron tunnels via orbital 2, with amplitude $(t_{L2}\, t_{R2})$. The amplitude $\delta_{L\to R}$ for the Cooper pair to tunnel through from left to right is then

$$\delta_{L\to R} = (t_{L1}\, t_{R1})(t_{L2}\, t_{R2}). \tag{2.57}$$

Assuming that the hybridization amplitudes are real, the amplitude describing tunneling of a spin-up electron via orbital 1(orange arrow in Figure 2.15**a**) and spin-down electron via orbital 2 from the right to the left lead (leftward tunneling) is exactly the same. Thus $\delta_{L\to R} = \delta_{R\to L}$ and the net resulting current vanishes. Therefore, the tunneling via single orbitals can not add to $I(\varphi = 0)$.

The lowest order process which contributes to $I(\varphi = 0)$ is the one in which one of the two electrons forming the Cooper pair changes the orbital during the tunneling process, while the other electron tunnels through the dot via a single orbital. Finite SOI enables such orbital change.

We consider the case when the magnetic field is orientated along the effective spin-orbit axis. The Hamiltonian of the dot then takes the simple form

$$H_{QD} = (\mu\tau_0 + E_{orb}\tau_z)\sigma_0 + B\tau_0\sigma_z + \alpha\tau_y\sigma_z \tag{2.58}$$

Here μ is the chemical potential, E_{orb} is the orbital energy, α parametrizes the strength of the SOI and B the Zeeman splitting, $\tau_{x,y,z}$ ($\sigma_{x,y,z}$) are Pauli matrices acting in orbital (spin) space (τ_0 (σ_0) are identity matrices). Usually the terms describing the Zeeman splitting and the SOI are smaller in comparison to the first term in the Hamiltonian and thus the $B\tau_0\sigma_z + \alpha\tau_y\sigma_z$ term in 2.58 is treated as a perturbation. The amplitude of the process represented by the purple arrow in Figure 2.15**b** is a second order perturbation and is proportional to $\alpha B\tau_y\sigma_0$. The spin-down electron takes the same path as before and the tunnel amplitude is unchanged. The Cooper pair tunneling amplitude now becomes

$$\delta_{L\to R} = (t_{L1}(-i\alpha B)\, t_{R2})(t_{L2}\, t_{R2}) \tag{2.59}$$

The reverse process however does not give the same amplitude, since the spin-up electron flipping from orbital 2 to 1 acquires the opposite phase, as represented with the orange arrow in Figure 2.15**b**. Thus

$$\delta_{R\to L} = (t_{L1}(i\alpha B)\, t_{R2})(t_{L2}\, t_{R2}) \tag{2.60}$$

The forward and backward tunneling process do not cancel each other but contributes towards a complex tunneling amplitude of the Cooper pair. By virtue of 2.56, this complex amplitude warrants an anomalous current.

When the magnitude field is oriented orthogonal to the SOI, the phases $\delta_{L\to R}$ and $\delta_{R\to L}$ are equal and no anomalous current can flow[30]. A component of the Zeeman field **B** parallel to $\mathbf{B_{SO}}$ is necessary to generate anomalous current and a φ_0-junction in the quantum dot. The larger the parallel component, the larger the anomalous current. This implies that by rotating the **B** field and measuring the anomalous current one can infer the intrinsic $\mathbf{B_{SO}}$ direction in the device.

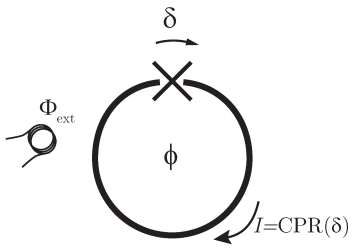

Figure 2.16: **Schematics of an RF-SQUID.** The RF-SQUID consists of a superconducting loop with circulating current J enclosing flux Φ interrupted by a JJ with phase difference φ. The externally applied flux is Φ_0.

DISTINCTION BETWEEN φ_0-JUNCTIONS, φ-JUNCTIONS

In literature, the nomenclature of φ_0-junction and φ-junction is sometimes used interchangeably and inconsistently, which I will try to clarify here.

- A φ_0-junction is a junction with energy minimum at phase $\varphi = \varphi_0$. Its CPR is of the form $I(\varphi) = \sin(\varphi + \varphi_0)$, or equivalently, $I(\varphi) = I_0 \sin\varphi + I_{anomalous} \cos\varphi$. Thus a φ_0 junction necessarily allows for anomalous current to flow. The experimental evidence of such a junction is presented in Chapter 6 of this thesis.

- A φ-junction, such as measured in Reference[31], is a JJ with a double energy minimum at phase $\pm\varphi$. It does not admit any anomalous current. Its CPR is characterized by a higher harmonic, for example $I(\varphi) = I_0 \sin\varphi + I_1 \sin(2\varphi)$ and its energy as a function of phase has a double minima symmetric around 0 provided $I_1 \geq \frac{1}{2} I_0$. The higher harmonic allows the junction to have multiple critical current values.

2.5. PHASE BIASING JOSEPHSON JUNCTIONS

The CPR of a JJ defines the supercurrent magnitude the junction can admit as a function of the phase difference: $I(\varphi) = \mathrm{CPR}(\varphi)$. The CPR is determined by the evolution of the ABS with phase (see 2.32), therefore measuring the CPR of a junction can shed light on the microscopic physics. To evaluate the CPR the phase needs to be an experimentally adjustable parameter; this is not the case for an SNS junction contacted by a source and drain lead, where the current I can be set by an external source but the phase adjusts itself such that $\mathrm{CPR}(\varphi) = I$.

In order to phase bias the junction, it must be embedded in a superconducting loop so that the superconducting order parameter winds up in itself imposing a boundary condition on the phase due to uniqueness. Such a loop is dubbed a Superconducting Quantum Interference Device (SQUID) since the supercurrent can take two interfering paths. Here we review the basics of SQUIDs, based on more extensive accounts such as [32, 33].

2.5.1. RF-SQUID

An rf-SQUID is a superconducting loop interrupted by a single Josephson junction. In Figure 2.16 we show the schematics of an RF-SQUID with phase difference δ across the

JJ, current I circulating in the loop which encloses a reduced flux ϕ. The continuity of the superconducting order parameter enforces the flux quantization condition

$$\delta + \phi = 2\pi n. \tag{2.61}$$

The reduced flux, equivalent to the phase drop over the lead, is the sum of the externally applied flux(i.e. an external magnetic field) minus the screening current:

$$\phi = \frac{2\pi}{\Phi_0}\Phi_{ext} - \phi_{sceen}$$

where $\phi_{screen} = \frac{2\pi}{\Phi_0}(L_G + LK)I$ is proportional to the loop inductance which is the sum of the geometric inductance L_G and the kinetic inductance L_K. The phase drop δ over the junction and the phase drop φ_{SC} over the lead due to kinetic inductance of the superconductor is related to the reduced flux by

$$\phi = \delta + \varphi_{\text{SC lead}} - \frac{2\pi}{\Phi_0}\phi_{\text{screen}}. \tag{2.62}$$

Throughout this thesis we use SQUID loops made typically out of NbTiN of diameter $\sim 1\mu$m and thickness and width ~ 100 nm , and the critical current of our nanowire JJ is in the nanoamper range. Such parameters yield inductances of $L_G \sim 1$ pH, $L_K^{NbTiN} \sim 10$ pH, negligible compared to the inductance L_J of the JJ $L_J \sim 10$ nH.

These inductane values mean that for nanosized SQUID loops, the phase drop due to the screening current and the phase drop over the leads can be neglected and 2.61 simplifies to

$$\delta = -\frac{2\pi}{\Phi_0}\Phi_{ext} + 2\pi n \tag{2.63}$$

Thus the phase drop over the JJ can be experimentally set using an external magnetic field perpendicular to the SQUID plane.

As the name suggests, an RF-SQUID is usually measured by probing its inductance via microwave signals, by inductively coupling the SQUID to a standard LC-tank circuit: the resonant frequency of the tank circuit is sensitive to the variation of the SQUID inductance.

However, one can measure an rf-SQUID in a DC transport scheme by weakly coupling a tunnel probe to the JJ in the loop acting as a source and connecting an electrode to the loop serving as a drain.

In Chapter 5 a weakly coupled tunnel probe is used for voltage biased spectroscopy of the junction, since the conductance measured through the junction is proportional to the carrier density of states (DOS), but the inverse proximity is too weak to disrupt superconductivity in the junction. Since the ABS in the junction are phase sensitive, the DOS and hence the measured conductance is flux periodic with the flux quantum. Such a setup is however unsuitable to directly measure the critical current or the CPR of the JJ.

2.5.2. DC-SQUID

A superconducting loop with two JJs in parallel is called a DC-SQUID. A DC-SQUID is shown in Figure 2.17 with junctions 1 and 2 each bearing critical current I_{C1}, I_{C2} and

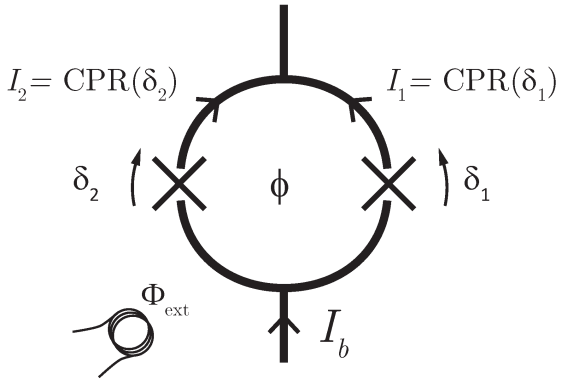

Figure 2.17: **Schematics of a DC-SQUID.** The DC-SQUID consists of a superconducting loop enclosing flux Φ interrupted by a JJ on both sides with phase difference $\varphi_{1,2}$. The total current applied through the loop is $I = I_1 + I_2$ and the externally applied flux is Φ_0.

phase difference δ_1, δ_2 respectively. The SQUID encloses a reduced flux ϕ and its own critical current is denoted $I_{C,SQUID}$.

The DC-SQUID set-up is extremely advantageous for nanowire junctions, as these junctions can be completely switched off via local gating. Thus a DC-SQUID with nanowire junctions can be operated as individual junctions as well a SQUID, allowing to easily measure individual junction properties and quantum interference on the same sample.

As in the previous section, we can safely assume for devices presented in this thesis that the geometric inductance of the loop and the kinetic inductance of the leads is negligible compared to the Josephson inductance, and therefore $\phi \approx \frac{2\pi}{\Phi_0}\Phi_{ext}$.

Flux quantization imposes:

$$\delta_1 - \delta_2 = \phi + 2\pi n \tag{2.64}$$

In general it is no longer possible to tune the phase over both junctions independently, except some limiting cases as we will see below.

The total current I passing through the DC-SQUID is

$$I = \mathrm{CPR}_1(\varphi_1) + \mathrm{CPR}_2(\varphi_2). \tag{2.65}$$

We define the junction asymmetry parameter α as

$$\alpha = \frac{I_{C1} - I_{C2}}{I_{C1} + I_{C2}}$$

and the average phase

$$\chi = \frac{\delta_1 + \delta_2}{2}.$$

We now assume that the CPR of both junctions in the SQUID can be well approximated by the tunnel junction CPR $I(\varphi_i) = I_{Ci}\sin(\varphi_i)$. This assumption holds for the nanowire junctions presented in this thesis.

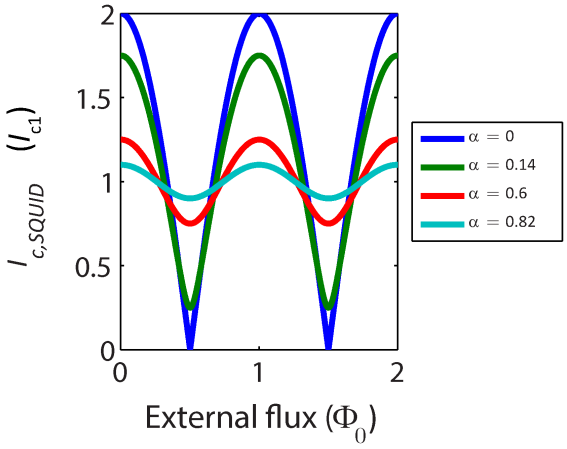

Figure 2.18: **Critical current of a DC-SQUID for varying junction symmetries.** The two junctions composing the DC-SQUID are assumed to have sinusoidal CPR $I_{1,2} = I_{C1,2}\sin\varphi_{1,2}$

The total bias current through the SQUID I_b can then be written

$$\begin{aligned} I_b &= I_{C1}\sin(\delta_1) + I_{C2}\sin(\delta_2) \\ &= I_{C1}\sin(\chi + \delta_1/2) + I_{C2}\sin(\chi - \delta_2/2) \\ \Rightarrow I_b &= I_{C,squid}\sin(\chi + \delta_0(\phi)) \end{aligned} \tag{2.66}$$

The SQUID basically can be regarded as a JJ of which the critical current $I_{C,squid}$ can be tuned via the flux:

$$I_{C,squid} = (I_{C1} + I_{C2})\sqrt{(1-\alpha^2)\cos^2\left(\frac{\phi}{2}\right) + \alpha^2} \tag{2.67}$$

and $\delta_0(\phi)$ satisfies

$$\sin(\delta_0(\phi)) = \frac{\alpha\sin\left(\frac{\phi}{2}\right)}{\sqrt{(1-\alpha^2)\cos^2\left(\frac{\phi}{2}\right) + \alpha^2}}$$

$$\cos(\delta_0(\phi)) = \frac{\cos\left(\frac{\phi}{2}\right)}{\sqrt{(1-\alpha^2)\cos^2\left(\frac{\phi}{2}\right) + \alpha^2}}$$

We plot $I_{C,squid}$ for different values of α in Figure 2.18. It is minimal when the two junctions interfere destructively at flux $\phi = \pi$ and maximal when they interfere constructively at flux $\phi = 0$.

CASE OF SYMMETRIC JJS

If the two JJs are identical and $\alpha = 0$ in 2.67 and $I_{C,SQUID}$ becomes

$$I_{C,SQUID} = 2I_C \left| \cos\left(\pi \frac{\Phi_{ext}}{\Phi_0}\right) \right| \tag{2.68}$$

i.e. the critical current of the SQUID vanishes at $\Phi_{ext} = \Phi_0/2 + n\Phi_0$.

Since the two junctions are idential the phase drop must be equal $\delta_1 = \delta_2 = \delta$.

CASE OF ASYMMETRIC JJS

If the critical current of one JJ is much higher than the other, say $\alpha \gg 1$, the observed total critical current of the SQUID will approximately be constant around I_{C1} with a superimposed oscillation of amplitude I_{C2}. Thus the phase drop over junction 1 will be locked at $\varphi_1 \approx \pi/2$, whereas 2.64 guarantees that φ_2 winds from 0 to 2π as the flux is ramped. This setup is useful when the SQUID is composed of a well-behaved reference junction and of one junction of interest of which we would like to extract the CPR of, as the experiment presented in Chapter 6.

BIBLIOGRAPHY

[1] H. K. Onnes, "The resistance of pure mercury at helium temperatures.," *Commun. Phys. Lab. Univ. Leiden*, vol. 120, no. 12, p. 1, 1911.

[2] J. Bardeen, L. N. Cooper, and J. R. Schrieffer, "Theory of Superconductivity," *Phys. Rev.*, vol. 108, pp. 1175–1204, Dec. 1957.

[3] S. Datta and P. F. Bagwell, "Can the Bogoliubov-de Gennes equation be interpreted as a 'one-particle' wave equation?," *Superlattices and Microstructures*, vol. 25, pp. 1233–1250, May 1999.

[4] J.-D. Pillet, *Tunneling spectroscopy of the Andreev Bound States in a Carbon Nanotube*. PhD thesis, CEA Saclay, 2011.

[5] L. Bretheau, *Localized Excitations in Superconducting Atomic Contacts: PROBING THE ANDREEV DOUBLET*. phdthesis, Ecole Polytechnique X, Feb. 2013.

[6] G. E. Blonder, M. Tinkham, and T. M. Klapwijk, "Transition from metallic to tunneling regimes in superconducting microconstrictions: Excess current, charge imbalance, and supercurrent conversion," *Phys. Rev. B*, vol. 25, pp. 4515–4532, Apr. 1982.

[7] M. Tinkham, *Introduction to Superconductivity: Second Edition*. Mineola, N.Y.: Dover Publications, second edition edition ed., June 2004.

[8] K. Flensberg, J. B. Hansen, and M. Octavio, "Subharmonic energy-gap structure in superconducting weak links," *Phys. Rev. B*, vol. 38, pp. 8707–8711, Nov. 1988.

[9] M. Büttiker, Y. Imry, R. Landauer, and S. Pinhas, "Generalized many-channel conductance formula with application to small rings," *Phys. Rev. B*, vol. 31, pp. 6207–6215, May 1985.

[10] C. W. J. Beenakker and H. van Houten, "Josephson current through a superconducting quantum point contact shorter than the coherence length," *Phys. Rev. Lett.*, vol. 66, pp. 3056–3059, June 1991.

[11] T. Yokoyama, M. Eto, and Y. V. Nazarov, "Josephson Current through Semiconductor Nanowire with Spin-Orbit Interaction in Magnetic Field," *J. Phys. Soc. Jpn.*, vol. 82, p. 054703, Apr. 2013.

[12] T. Yokoyama, M. Eto, and Y. V. Nazarov, "Anomalous Josephson effect induced by spin-orbit interaction and Zeeman effect in semiconductor nanowires," *Phys. Rev. B*, vol. 89, p. 195407, May 2014.

[13] L. P. Kouwenhoven, D. G. Austing, and S. Tarucha, "Few-electron quantum dots," *Rep. Prog. Phys.*, vol. 64, no. 6, p. 701, 2001.

[14] P. W. Anderson, "Localized Magnetic States in Metals," *Phys. Rev.*, vol. 124, pp. 41–53, Oct. 1961.

[15] S. De Franceschi, L. Kouwenhoven, C. Schönenberger, and W. Wernsdorfer, "Hybrid superconductor-quantum dot devices," *Nat Nano*, vol. 5, pp. 703–711, Oct. 2010.

[16] P. Coleman, "Local moment physics in heavy electron systems," in *AIP Conference Proceedings*, vol. 629, pp. 79–160, AIP Publishing, Sept. 2002.

[17] A. C. Hewson, *The Kondo Problem to Heavy Fermions.* Cambridge University Press, 1993.

[18] M. Buttiker, "Coherent and sequential tunneling in series barriers," *IBM Journal of Research and Development*, vol. 32, pp. 63–75, Jan. 1988.

[19] A. Martín-Rodero and A. L. Yeyati, "Josephson and Andreev transport through quantum dots," *Advances in Physics*, vol. 60, pp. 899–958, Dec. 2011.

[20] L. I. Glazman and K. A. Matveev, "Resonant Josephson current through Kondo impurities in a tunnel barrier," *JETP Letters*, vol. 10, no. 49, pp. 659–662, 1989.

[21] J. A. van Dam, Y. V. Nazarov, E. P. A. M. Bakkers, S. De Franceschi, and L. P. Kouwenhoven, "Supercurrent reversal in quantum dots," *Nature*, vol. 442, pp. 667–670, Aug. 2006.

[22] A. V. Rozhkov and D. P. Arovas, "Josephson Coupling through a Magnetic Impurity," *Phys. Rev. Lett.*, vol. 82, pp. 2788–2791, Mar. 1999.

[23] E. Vecino, A. Martín-Rodero, and A. L. Yeyati, "Josephson current through a correlated quantum level: Andreev states and π junction behavior," *Phys. Rev. B*, vol. 68, p. 035105, July 2003.

[24] H. I. Jørgensen, T. Novotný, K. Grove-Rasmussen, K. Flensberg, and P. E. Lindelof, "Critical Current $0-\pi$ Transition in Designed Josephson Quantum Dot Junctions," *Nano Lett.*, vol. 7, pp. 2441–2445, Aug. 2007.

[25] J.-P. Cleuziou, W. Wernsdorfer, V. Bouchiat, T. Ondarçuhu, and M. Monthioux, "Carbon nanotube superconducting quantum interference device," *Nat Nano*, vol. 1, pp. 53–59, Oct. 2006.

[26] R. Maurand, T. Meng, E. Bonet, S. Florens, L. Marty, and W. Wernsdorfer, "First-Order $0-\pi$ Quantum Phase Transition in the Kondo Regime of a Superconducting Carbon-Nanotube Quantum Dot," *Phys. Rev. X*, vol. 2, p. 011009, Feb. 2012.

[27] R. Delagrange, D. J. Luitz, R. Weil, A. Kasumov, V. Meden, H. Bouchiat, and R. Deblock, "Manipulating the magnetic state of a carbon nanotube Josephson junction using the superconducting phase," *Phys. Rev. B*, vol. 91, p. 241401, June 2015.

[28] J.-F. Liu and K. S. Chan, "Relation between symmetry breaking and the anomalous Josephson effect," *Phys. Rev. B*, vol. 82, p. 125305, Sept. 2010.

[29] R. P. Feynman, R. B. Leighton, and M. Sands, *The Feynman Lectures on Physics, Vol. 3*. Reading/Mass. u.a.: Addison Wesley, later printing edition ed., Jan. 1971.

[30] A. Zazunov, R. Egger, T. Jonckheere, and T. Martin, "Anomalous Josephson Current through a Spin-Orbit Coupled Quantum Dot," *Phys. Rev. Lett.*, vol. 103, p. 147004, Oct. 2009.

[31] H. Sickinger, A. Lipman, M. Weides, R. G. Mints, H. Kohlstedt, D. Koelle, R. Kleiner, and E. Goldobin, "Experimental Evidence of a φ Josephson Junction," *Phys. Rev. Lett.*, vol. 109, p. 107002, Sept. 2012.

[32] S. M. Frolov, *Current-phase relations of josephson junctions with ferromagnetic barriers*. PhD thesis, University of Illinois at Urbana-Champaign, 2005.

[33] J. Clarke and A. I. Braginski, *The SQUID Handbook: Fundamentals and Technology of SQUIDs and SQUID Systems*. Weinheim: Wiley-VCH, 1 edition ed., July 2004.

3

SUPERCURRENT INTERFERENCE IN FEW-MODE NANOWIRE JOSEPHSON JUNCTIONS

Junctions created by coupling two superconductors via a semiconductor nanowire are the basis for detection, fusion, and braiding of Majorana bound states. A magnetic field parallel to the wire is used to obtain topological superconductivity in superconductor-semiconductor systems. We therefore study Josephson effect in nanowire junctions in the presence of large magnetic fields.

We find that critical currents in NbTiN-InSb-NbTiN Josephson junctions are strongly suppressed by the magnetic field. Moreover, the critical current exhibits gate-tunable nodes and kinks in the magnetic field. A numerical model that includes vector potential, Zeeman and spin-orbit effects in a quasi-ballistic multi-mode nanowire suggests that the field evolution of the critical current is mostly determined by the interference of supercurrents carried by different transverse modes. These findings inform the development of Majorana-based quantum circuits.

In collaboration with K. Zuo, V. Mourik, B. Nijholt, D. J. van Woerkom, A. Geresdi, J. Chen, V. P. Ostroukh, A. Akhmerov, S. R. Plissard, D. Car, E. P. A. M. Bakkers, D. Pikulin, L. P. Kouwenhoven. and S. M. Frolov.

3.1. INTRODUCTION

Semiconductor nanowires coupled to superconductors are a promising platform for investigating Majorana bound states [1–8]. Josephson weak links based on nanowires may provide additional evidence for Majorana bound states, e.g. through the fractional Josephson effect [9–11]. These weak links can also become elements of Majorana-based topological quantum circuits [12–15]. Previous work on semiconductor nanowire Josephson junctions demonstrated supercurrent transistors [16], nanowire SQUIDs[17, 18], and gate-tunable superconducting quantum bits[19, 20]. Recent works reported Josephson effects at high magnetic fields sufficient to generate unpaired Majorana bound states [18, 21–23].

In this chapter, we study mechanisms of supercurrent suppression through the simultaneous magnetic field and gate voltage evolution of critical currents in nanowire Josephson junctions tuned to the few-mode regime. The junctions consist of InSb weak links and NbTiN superconductor contacts. For magnetic fields parallel to the nanowire, we observe a strong suppression of critical current at magnetic fields on the scale of 100 mT. When the magnetic field exceeds $\sim 100\,\mathrm{mT}$ critical currents exhibit aperiodic local minima (nodes). The fields that correspond to the minima are tunable with local electrostatic gates. To understand our data, we develop a numerical model of a quasi-ballistic multimode nanowire of realistic geometry. We include spin-orbit field, orbital and Zeeman effects produced by magnetic field. Based on the simulation, we conclude that quantum interference between supercurrents carried by different transverse modes is the dominant mechanism responsible for our observations. Such an interference explains the critical current suppression, as well as the occurrence of gate-sensitive nodes in the critical current.

3.2. EXPERIMENTAL SETUP

The schematic of a few-mode nanowire Josephson junction is presented in Fig. 3.1(a). A device similar to those used in this study is shown in the inset of Fig. 3.1(b), and the detailed fabrication process followed is described in Ref. [4]. The junction consists of an InSb nanowire with a diameter of $80 \pm 10\,\mathrm{nm}$ with NbTiN contacts, fabricated on top of an array of local gates isolated from the junction by a dielectric layer. Some of the gates are 200 nm wide, while others are 50 nm wide. We report data from 2 different devices in the main text, data from an additional device is shown in the supplementary materials. Device 1 has a contact spacing of ~ 1 micron and the nanowire is oriented at an angle $25° \pm 5°$ with respect to $\boldsymbol{B}$; device 2 has a contact spacing of $\sim 625\,\mathrm{nm}$, with the wire at an angle of $0° \pm 5°$ with respect to $\boldsymbol{B}$. Device 3, with a shorter contact spacing of $\sim 150\,\mathrm{nm}$, showed similar behavior (see supplementary materials). Measurements were performed in a dilution refrigerator with a base temperature of $\sim 60\,\mathrm{mK}$. All electrical lines connecting the device are equipped with standard RC and copper powder filtering at the mixing chamber stage to ensure a low electrical noise environment. Voltage measurements are performed in the four-terminal geometry.

We set all the gates underneath the nanowire to positive voltages in the few-mode transparent regime in which no quantum dots are formed between the superconducting contacts and the normal state conductance exceeds $2e^2/h$ (see the full gate trace of

supercurrent in Section 3.9.1).

3.3. SUPERCURRENT MEASUREMENTS AS A FUNCTION OF MAGNETIC FIELD

Fig. 3.1(b) shows a typical example of differential resistance $\mathrm{d}V/\mathrm{d}I$ as a function of the magnitude of the magnetic field B and the current bias I_{bias} in this regime, with low resistance supercurrent regions in dark blue around zero current bias. Note that the data are asymmetric with respect to current reversal because the junction is in the underdamped hysteretic regime, and only one sweep direction is plotted.

A strong decrease of the switching current is observed from $B = 0\,\mathrm{T}$ to $B = 100 - 200\,\mathrm{mT}$. Beyond the initial decrease, the critical current exhibits non-monotonic behavior with multiple nodes and lobes. Despite the $1\,\mu\mathrm{m}$ contact separation, the supercurrent can be resolved up to fields as high as $B = 2\,\mathrm{T}$. The supercurrent at finite fields often lacks the sharp switching behavior when the critical current is exceeded. In voltage bias measurements, this feature corresponds to a smoothly increased conductance at zero bias. Thus, the supercurrent can be mistaken for a signature of Majorana fermions in devices with two superconducting contacts (see supplementary information for voltage-bias data).

3.4. POSSIBLE MECHANISMS CAUSING SUPERCURRENT OSCILLATIONS

We now qualitatively discuss the possible explanations for the behavior observed in Fig. 3.1(b). Zeeman splitting can induce $0-\pi$-junction transitions which result in an oscillatory Josephson energy as a function of the magnetic field [24–26]. This alternating $0-\pi$ junction behavior is due to spin-up and spin-down channels acquiring different phases as they travel across the junction [Fig. 3.1(a)]. However, in our junctions a strong spin-orbit effective field, which is believed to point perpendicular to the nanowire, reduces the relative phase shifts of spin-up and spin-down and lifts the nodes in the Josephson energy[27]. For the spin-orbit strength previously reported in InSb nanowires [28, 29], we estimate an effective spin-orbit field of order 1-2 T. We therefore do not expect $0-\pi$-transitions for in-plane fields below 1 T for any chemical potential other than in the close proximity to a transverse mode edge (within 1-2 meV). Given the typical mode spacing of 10-20 meV [30, 31], the Zeeman π-junction effect is an unlikely explanation for the non-monotonic supercurrents generically observed here.

In addition to spin-related effects, supercurrents carried by different transverse modes of the quasi-one-dimensional wire would generally acquire different phase shifts and interfere due to mode mixing within the wire or at the superconductor contact. Such Fraunhofer-like interference becomes relevant when a single superconducting flux quantum is threaded through the nanowire cross-section, a regime which is reached for $B \approx 0.25\,\mathrm{T}$, well within the range of the present study. Comparison of the experimental and numerical data in this paper suggest that this is the effect that dominates the magnetic field dependence of the critical current.

Transitions in and out of the topological superconducting phase were predicted to

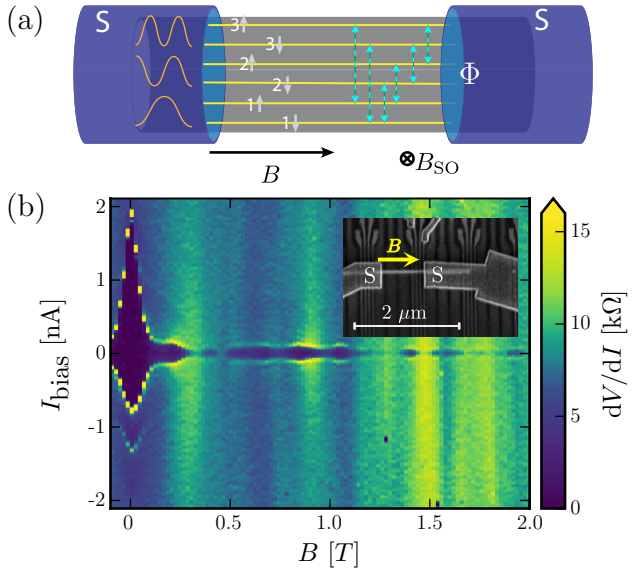

Figure 3.1: (a) Schematic Superconductor (SC)-nanowire-SC Josephson junction. The cross-section shows cartoon wavefunctions of $n = 3$ transverse modes and flux Φ penetrating the area of the nanowire. Arrows indicate spin-resolved modes, dotted lines are same-spin scattering events within the wire. All modes are coupled at the contacts (blue dashed lines). Directions of **B** and spin-orbit effective field $\mathbf{B_{SO}}$ are indicated. (b) Differential resistance dV/dI versus B and I_{bias}. Current bias sweep direction is from negative to positive. Data from device 1. Inset: Scanning electron microscope (SEM) image of a typical device similar to those studied here. S labels the superconducting contacts while B indicates the in-plane magnetic field for device 2.

induce fluctuations in the junction's critical current[32]. Although we used devices similar in this study to those used in recent Majorana experiments [4, 33, 34], here we did not gate-tune the regions of the wire underneath the superconducting contacts into the topological regime. An accidental topological regime occurring on both sides of the junction in multiple devices is an unlikely explanation to the generic observations reported here.

3.5. SUPERCURRENT EVOLUTION WITH MAGNETIC FIELD AND GATE POTENTIAL

Fig. 3.2 shows a sequence of magnetic field dependences of the critical current, obtained by adjusting one of the narrow local gates. The critical current exhibits kinks, multiple nodes [Fig. 3.2(c)], or just a single node in the same field range [Fig. 3.2(a)]. At some nodes the critical current goes to zero, while a non-zero supercurrent is observed at other nodes. No periodic patterns such as those characteristic of a DC-SQUID or a uniform junction are observed. Note that slight changes in the gate voltage are sufficient to dramatically alter the magnetic field evolution curve; the corresponding change in chemical potential $\Delta\mu$ is small ($\Delta\mu < 1$ meV) compared with the typical intermode spacing (~ 15 meV). Furthermore, the gate used only tunes a 100 nm segment of the 650 nm

long junction.

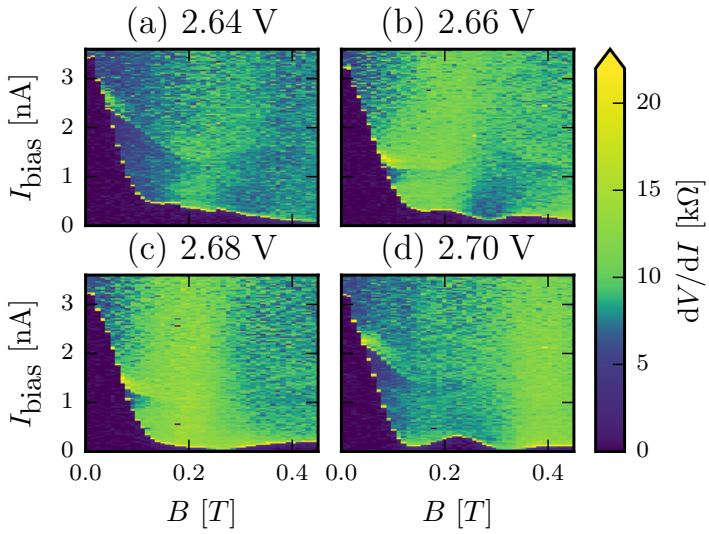

Figure 3.2: (a)-(d) $\mathrm{d}V/\mathrm{d}I$ versus B and I_{bias} for different gate voltage settings V_g indicated above each panel. Data from device 2, see Sec3.9.1 for the SEM image where the gate used for tuning is marked.

The gate dependences of the supercurrent are presented in Fig. 3.3. The critical current is strongly reduced at fields above 100 mT irrespective of the gate voltage. At all fields, the supercurrent is strongly modulated by the gate voltage. However, the gate voltage at which nodes in the critical current occur differs for each magnetic field value. Thus no straightforward connection can be made between the zero-field critical current and node positions at finite field, see also Fig. 3.5.

3.6. THEORETICAL MODELING

In order to establish which of the mechanisms depicted in Fig. 3.1(a) is dominating over the magnetic field evolution of the Josephson effect, we develop an effective low-energy model of a spin-orbit and Zeeman-coupled few-mode nanowire, covered by superconductors at both ends. In this three-dimensional model, the nanowire cross section is a regular hexagon. We define x as the direction along the wire, y perpendicular to the wire in the plane of the substrate, and z perpendicular to both wire and substrate. The

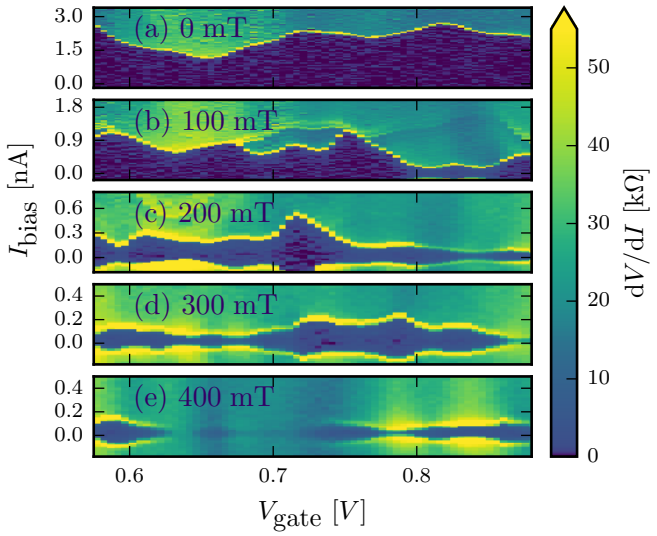

Figure 3.3: (a)-(e) dV/dI versus V_g at different B and I_{bias} indicated on the right. Data from device 2. The gate used for tuning is different from that used in Fig. 3.2, see Sec3.9.1 for details.

corresponding Hamiltonian reads:

$$H = \left(\frac{\boldsymbol{p}^2}{2m^*} - \mu\right)\tau_z + \alpha(k_x\sigma_y - k_y\sigma_x)\tau_z + g\mu_B\boldsymbol{B}\cdot\boldsymbol{\sigma} + \Delta\tau_x. \tag{3.1}$$

Here $\boldsymbol{p} = -i\hbar\nabla + e\boldsymbol{A}\tau_z$ is the canonical momentum, where e is the electron charge, and $\boldsymbol{A} = \left[B_y z - B_z y,\, 0,\, B_x y\right]^T$ is the vector potential chosen such that it does not depend on x. Further, m^* is the effective mass, μ the chemical potential controlling the number of occupied subbands in the wire, α the strength of Rashba spin-orbit interaction, g the Landé g-factor, μ_B the Bohr magneton, and Δ the superconducting pairing potential. σ_i and τ_i are the Pauli matrices acting in spin and electron-hole space respectively. The electric field generated by the substrate is most likely along the z direction, such that the Rashba spin-orbit acts in the xy-plane. Finally, we include the vector potential using the Peierls substitution [35].

We perform numerical simulations of the Hamiltonian (3.1) on a 3D lattice in a realistic nanowire Josephson junction geometry and calculate the supercurrent across the junction using the algorithm described in Ref. [36]. We perform the numerical simulations using the Kwant code [37]. The source code and the specific parameter values are available in Sec3.10.1.

3.7. DISCUSSION

Numerical results are presented in Figs. 3.4 and 3.5. First, we discuss the case of only a single transverse mode occupied [Fig. 3.4(a),(b)]. When all field-related terms of Eq. (3.1)

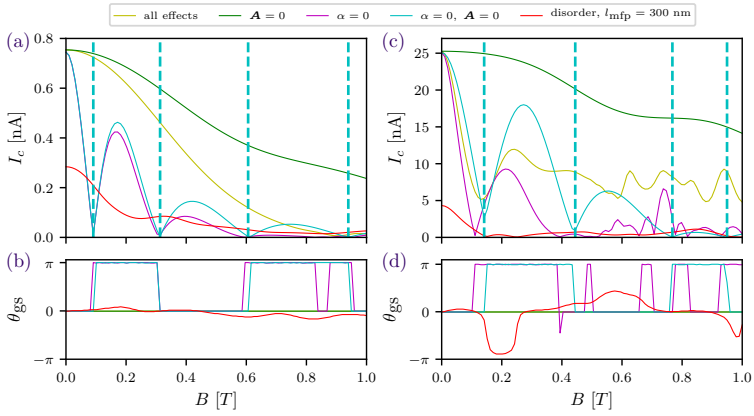

Figure 3.4: Critical currents and corresponding ground state phase for different combinations of interactions of the model Hamiltonian. Color coding upper legend panel: $\boldsymbol{A}=0$ corresponds to no orbital effect and $\alpha=0$ to no spin-orbit effect, Zeeman effect is always present. The curves in panel (a) and (b) are for the single transverse mode (two spin modes) regime, at low chemical potential, $\mu=10$ meV. The disorder curve corresponds to a mean-free path of $l_{\mathrm{mfp}}=300$ nm. Panel (c) and (d) show curves for the same Hamiltonian but in the multi-mode (5 transverse (10 spin-full) modes) regime at higher chemical potential, $\mu=50$ meV. Dashed light blue lines in (a) and (c) indicate the positions of $0-\pi$ transitions in the absence of disorder and with $\alpha=0$, $\boldsymbol{A}=0$. The $0-\pi$ transitions happening at non-zero disorder in (d) is due to chemical potential renormalization closer to the band bottom, illustrating a more exotic possibility (see supplementary materials for more details), deviations from 0 and π

are included ($\mathbf{A}\neq\mathbf{0}$, $g\neq 0$, $\alpha\neq 0$), we observe a monotonic decay of the critical current on the scale of 1 Tesla, which is much more gradual than in the experiment. Indeed a single mode cannot interfere with itself, thus the orbital effect of the magnetic field (described by $\mathbf{A}$) cannot cause nodes in the supercurrent in this regime.

The π-junction effect is suppressed up to fields of order 1 T due to the strong spin-orbit effective field, which keeps spin-up and spin-down at the same energy so that they acquire the same phase shifts traversing the junction. The critical current eventually decays because the Zeeman term overtakes the spin-orbit term at fields greater than 1 Tesla. When the Zeeman term is turned on while the spin-orbit term is turned off ($g\neq 0, \alpha=0$), we see several $0-\pi$ transitions taking place within the studied field range, confirmed by the critical current phase switching between $\pi/2$ and $-\pi/2$ [Fig. 3.4(b)]. Disorder within the nanowire suppresses the critical current at all fields, however the initial decay of critical current as well as the nodes at higher fields are present also in the disordered case (see Section 3.9).

In order to reproduce a rapidly decaying and non-monotonic critical current as in Figures 3.1 to 3.3, multiple transverse modes need to be occupied [Fig. 3.4(c)]. In this case, models that neglect the orbital effect display either a monotonic decay of the critical current ($\mathbf{A}=\mathbf{0}$), or critical current fluctuations due to $0-\pi$ transitions ($\mathbf{A}=\mathbf{0}$, $\alpha=0$), as in the single-mode case. In contrast, however, whenever $\mathbf{A}\neq\mathbf{0}$, a strong suppression of the critical current is observed in the simulation between $B=0$ and $B=100-200$ mT. At higher fields, the critical current exhibits nodes of variable depth. This behavior, ob-

tained for realistic device parameters with all relevant effects of the magnetic field included, is in qualitative agreement with the experiment, see Fig. 3.1 for example. We note that $0-\pi$ transitions survive when $\mathbf{A} \neq \mathbf{0}$ and $\alpha = 0$, but they cannot be distinguished from nodes caused by orbital interference based on two-terminal measurements; their identification requires phase-sensitive experiments [Fig. 3.4(d)]. Finally, we note that the critical phase can continuously change between $\pm\pi/2$ due to higher harmonics in the current-phase relationship present in realistic wires[38].

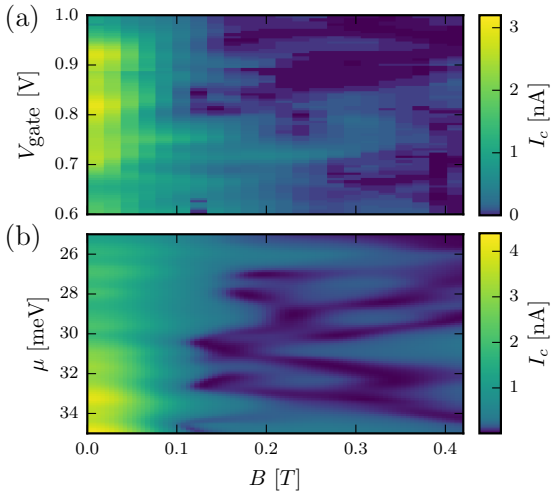

Figure 3.5: Comparison between experimental (a) and numerical results (b). The parameters for the numerical simulations are the same as Fig. 3.4(b) with a mean-free path of $l_{\text{mpf}} = 160\,\text{nm}$ and a gate size of 640 nm. The range of chemical potential is chosen using Ref. [39]. Experimental data from Device 2.

In Fig. 3.5 we compare side-by-side experiment and simulations via field-vs-gate maps of the critical current. In Fig. 3.5(a), the switching current from a set of $\mathrm{d}V/\mathrm{d}I$ vs. I_{bias} traces similar to those in Fig. 3.3 was extracted (see Sec3.10.1 for the details of the algorithm). Beyond the decay of critical current on the scale of 100 mT, the experimental data show a complex evolution of critical current maxima and minima in gate-field space. Remarkably, this evolution as well as the initial decay are well reproduced by the simulation that uses the nanowire parameters used in Fig. 3.4 including all effects of magnetic field and disorder[Fig. 3.5(b)]. This shows good applicability of our model to the experimental system.

3.8. CONCLUSION

Our results are instrumental for modeling Majorana setups. Specifically, the decrease of Josephson energy by an order of magnitude is observed at fields at which the onset of topological superconductivity is reported. This effect should be taken into account in efforts to realize recent proposals for fusion and braiding of Majorana fermions [12–15], especially those that rely on controlling the Josephson coupling [12, 13, 15]. We suggest that in such devices narrow multimode nanowires should be used. In this case strong

Josephson coupling due to many modes will not be strongly affected by magnetic field-induced supercurrent interference.

3.9. ADDITIONAL DATA

3.9.1. ZERO FIELD GATE DEPENDENCE: DEVICE 1

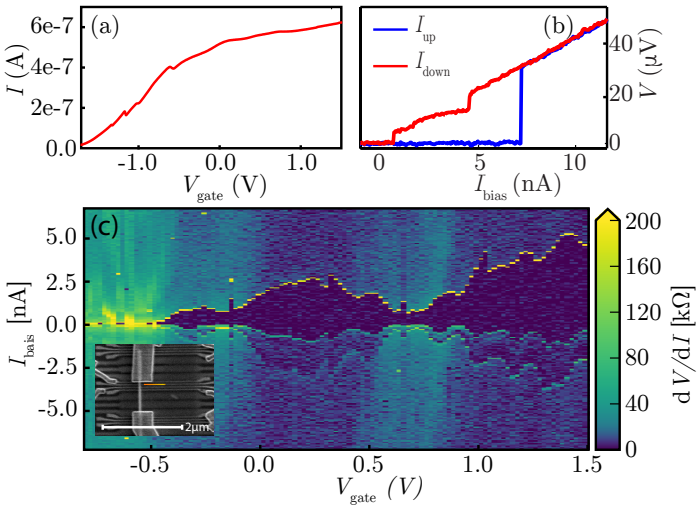

Figure 3.6: a) Device current as a function of gate voltage, V_{bias} = 10 mV. The varied gate is indicated in inset of c), all other gates are at +3 V. b) Voltage-current characteristic for both upwards (blue) and downwards (red) sweeping direction of current bias. The supercurrent of 8 nA is the maximum supercurrent observed in this device and corresponds to all gates at +3V. c) Numerical derivative dV/dI of V (I) as function of current and gate voltage. Current bias is swept from negative to positive.

Characterization of device 2 at B=0 T is shown in Figure 3.6. Current versus local gate voltage is measured at V_{bias} = 10 mV (Figure 3.6c). Taking known series resistances into account, the device resistance of ~6 kΩ is found, corresponding to the sum of the conduction channels and contact resistances.

As shown in Figure 3.6b, by optimizing the gate voltages a maximal supercurrent of 8 nA was found, with a corresponding voltage of 32 μV, which developed upon switching to the normal state. The junction is hysteretic as shown by the low retrapping current, and has a sharp transition to the normal state, indicating that the junction is in the underdamped regime. Note that self-heating may also contribute to the hysteresis [40].

3.9.2. SHAPIRO STEP MEASUREMENTS

Device 2 has been cooled down a second time with a radio frequency (RF) antenna near the sample. This enabled the study of Shapiro steps in the junction as a function of microwave power and frequency. Here, we focus on the power dependence of Shapiro steps for different magnetic fields. The device is again tuned to a multimode regime, comparable to V_{gate} = 0.5 V in Figure 3.6c. Due to the RF-antenna, the microwave background in the vicinity of the junction has increased, which led to an extra rounding of the V (I)-trace near the switching bias. Figure 3.7 summarizes the main findings of these measurements.

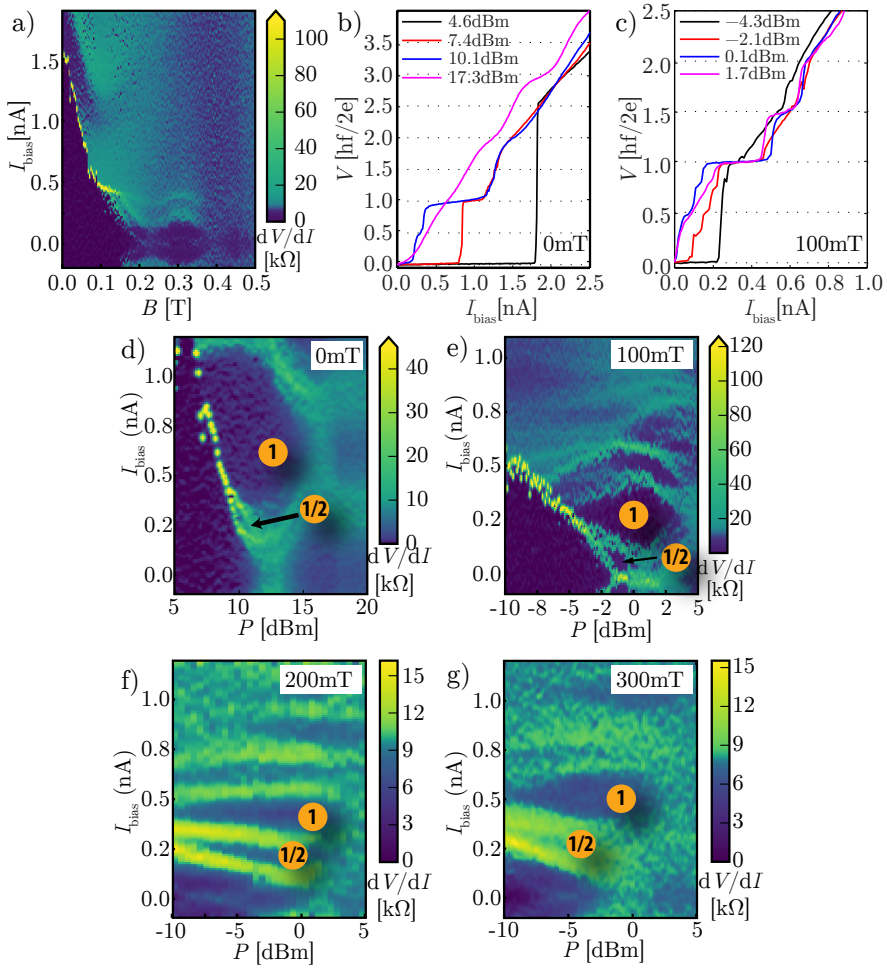

Figure 3.7: Shapiro steps in magnetic field. a) B dependence of supercurrent without microwave radiation applied. Numerical derivative dV/dI of the original $V(I)$ curves is shown. b) Shapiro steps at B = 0 T for different microwave powers. At the lowest RF power of 4.6 dBm (black line) no Shapiro steps are present. A half integer step is visible at 10.1 dBm (blue line). c) Shapiro steps at B = 100 mT for different microwave powers in a histogram. Half and quarter integer steps are visible. d)-g) Microwave power dependence of Shapiro steps for different B. Numerical derivative dV/dI of the original $V(I)$ curves is shown, in this representation the Shapiro step plateau corresponds to low differential resistance (blue color). At B = 0 T (panel d)), the power dependence is dominated by integer Shapiro steps and only a small contribution of half integer steps is visible. At B = 0.1 T (panel e)) fractional steps are visible. Here not only half integer steps, but also quarter steps are weakly present. B = 0.2T (panel f)) is closest to the minimum supercurrent at 0.25 T. Here the half integer and integer steps are almost equal in width. Finally, beyond the minimum of supercurrent, at B = 0.3 T (panel g)), the integer steps increase again in width relative to the half integer step. Curves in b) and c) are from the same datasets as shown in respectively d) and e). Values given for the RF power in panels b)-g) is the ouput power of microwave source, 60 dB attenuation, of which 20 dB at low T, is applied. Data is from device 2, second cooldown.

B (T)	I_{switch} (nA)	$w_{1/2}$ (nA)	w_1 (nA)	$w_{1/2}/w_1$
0.0	2.41	0.12	0.87	0.14
0.1	0.63	0.12	0.34	0.35
0.2	0.34	0.15	0.23	0.65
0.3	0.35	0.16	0.30	0.53

Table 3.1: Summary of switching current and maximum plateau widths of the 1/2 and 1st Shapiro steps for different magnetic fields. Data extracted from Figure 3.7b,d,e,f, except switching current at B = 0 T, which is taken from a larger dataset of which part is shown in Figure 3.7d.

Figure 3.7a is a B dependence of supercurrent in the absence of microwave drive. The supercurrent pattern as a function of magnetic field is similar to the one shown in Figure 1 of the main text. This indicates that thermally cycling the device did not change the qualitative behavior of the device, although the exact gate tunings are different.

We focus on the power dependence of Shapiro steps at different B strengths of 0, 100, 200 and 300 mT corresponding to Figure 3.7d,e,f,g respectively. The microwave frequency is kept fixed at 2.0 GHz. Shapiro steps show up at voltages corresponding to $V = n \cdot \frac{hf}{2e}$, where n may be a fraction. At B = 0 mT (Figure 3.7d), half integer steps are only weakly present. At B = 100 mT (Figure 3.7e), not only n = 1/2 steps but also weak n = 1/4 steps are visible. This is clearly visible in Figure 3.7c where the same data are plotted in a voltage histogram, where high voltage counts correspond to the plateaus of the Shapiro steps.

The B = 200 mT and B = 300 mT cases (Figure 3.7e,f) correspond to low critical current. Nevertheless, Shapiro steps can still be resolved. At B = 200 mT, which is closest to the minimum of critical current, the width of the 1/2 step is more than half the width of the 1st step, here the maximum step ratio is found. At 300 mT the 1/2 step is still large compared to the 1st step, but slightly less pronounced compared to 200 mT. This behavior is summarized in Table 3.1.

Shapiro steps at fractional frequencies, especially the half-integer steps, have been previously observed in Josephson junctions under various conditions[41, 42]. For instance, they can arise due to Josephson coupling of higher orders accompanied by a non-sinusoidal current-phase relationship[43]. In quasiballistic few-mode Josephson junctions the current-phase relation is expected to be non-sinusoidal, consistent with half-integer Shapiro steps observed here even at zero magnetic field. The higher order 1/4-steps are more exotic and deserve a deeper study in the future, though they may also originate from non-sinusoidal current-phase relationship.

In a non-sinusoidal Josephson junction tuned to the 0-π transition the first order Josephson effect which is responsible for strong integer Shapiro steps vanishes, thus the current phase relationship is dominated by higher harmonics. In this case, Shapiro steps at half-integer and integer frequencies are expected to appear with the same step widths. The results presented here show that the ratio of step widths for half integer to integer steps indeed increases near a field-induced node in the critical current. However, the results are not conclusive as to whether this is due to a 0-π transition.

On the other hand, Majorana zero modes coupled across a junction barrier are predicted to result in disappearing odd-integer Shapiro steps[2, 3]. Thus the behavior observed here is opposite that expected due to Majorana modes: extra fractional steps in

addition to integer steps are observed.

3.9.3. ANGLE DEPENDENCE OF FLUCTUATIONS

In this section we present results from device 3 (Figure 3.9 b)) with contact spacing of 150 nm on which we performed current bias measurements with similar conditions as reported in the main text.

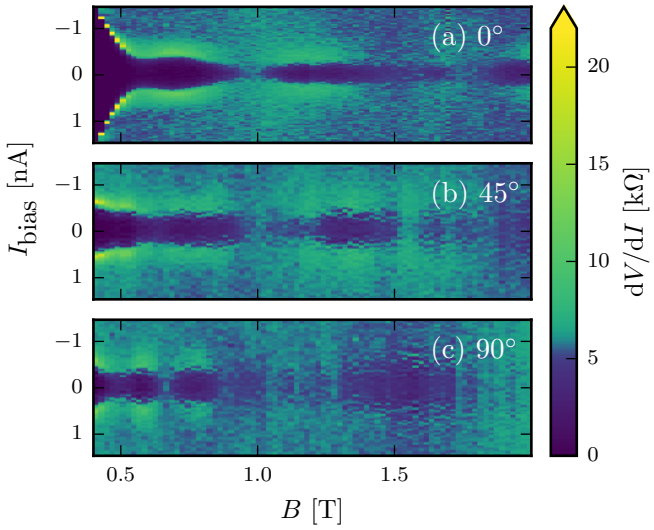

Figure 3.8: **Differential resistance measured as a function of current bias and magnetic field strength of Device 3.** The angle indicated in each panel is the angle of the magnetic field relative to the wire axis, in the plane of the substrate.

The device shows a monotonic decrease of the critical current for magnetic field up to 400 mT (not shown in the figure). This extended initial decay is attributed to shorter contact separation. Beyond 400 mT, the critical current fluctuates at a period depending on the direction of the magnetic field. Figure 3.8 shows the differential resistance of the device for three different field directions. The top panel shows data where the field is pointed along the nanowire. The critical current decays until the field reaches 600 mT, beyond which it exhibits a weakly pronounced maximum and disappears at 900 mT after which it reappears again. As the field angle is rotated in the plane of the substrate (Figs.3.8(b),(c)), the critical current decays faster as a function of the field strength, and the subsequent nodes of the critical current are closer spaced in field. We associate this behavior with increased flux through the nanowire at finite angles between the field and the wire.

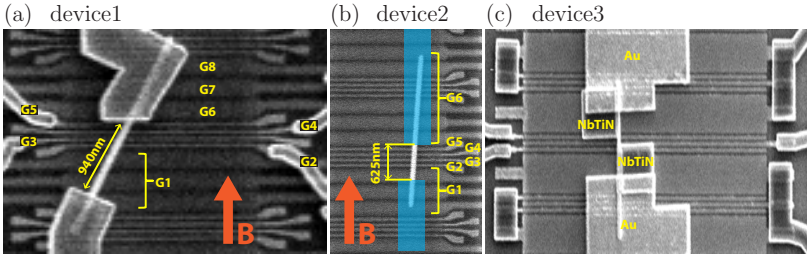

Figure 3.9: Schematics based on SEM picture of device 1, device 2 and device 3. a) Device 1, with an angle of $25^\circ \pm 5^\circ$ with the magnetic field. In all devices, not all local gates are operated independently: as indicated in the figures, larger gates are formed by shorting some of the local gates together, e.g G1. b) Device 2, shown with the superconducting electrode design superimposed on top of the SEM image, as this device has not been imaged after the final fabrication step. The device has a contact spacing of ~ 625 nm, with the wire at an angle of $0^\circ \pm 5^\circ$ with respect to magnetic field. c) Device 3, incorporating two quasi-particles traps next to the superconducting contacts. The length of the Josephson junction is ~ 150 nm. Device 3 is cooled down in a setup where the magnetic field could be rotated using a 3D vector magnet.

3.9.4. ZERO BIAS PEAKS DUE TO SUPERCURRENT CAN ONSET AT FINITE MAGNETIC FIELD

Devices used in this study were initially fabricated in order to search for Majorana zero modes. In fact, they pre-date devices used in REF. However, effects reported in this section illustrate why devices with two superconducting contacts, even if the contacts are almost 1 micron apart, cannot be used for unambiguous detection of Majorana zero modes [5, 44, 45]. Specifically, we show that in a voltage-biased measurement, supercurrent can appear as a zero-bias peak that onsets at finite magnetic field, thus mimicking a key Majorana signature. If devices have two hard-gap superconducting contacts, peaks due to Majorana appear at Δ, and this can be used to distinguish between Majorana and supercurrent. However, no hard gap has so far been demonstrated at finite fields in the Majorana regime, and therefore a finite density of states is expected at zero bias, thus Majorana and supercurrent peaks may coexist at the same bias. We show here the survival of small supercurrents in the quantum-dot regime and up to high magnetic fields of 2 T (Figure 1 in main text), thus supercurrents are found in the same range of parameters as those used in Majorana experiments.

The results presented in Figure 3.10 show our main finding. By putting a negative voltage on one of the local gates in between the superconducting contacts and varying a gate next to it, a tunneling regime is realized with quantum dot-like features. This corresponds to a regime comparable to V_{gate} < -0.5 V shown in Figure 3.6a for device 2. The result of a current biased measurement in this regime is shown in Figure 3.10a. A very small (down to 1 pA) supercurrent is resolved in this gate range. Interestingly, for gate regimes with lower resistance the supercurrent initially grows, as expected, but then the dV/dI peak related to the switching current broadens and is no longer visible. We focus here on the B dependent behavior as shown in Figure 3.10b,c,d. Picking a gate position with no initially resolved supercurrent, in a current biased measurement, at around 200 mT a small supercurrent shows up in a slightly more resistive regime. Such a small supercurrent may show up in a differential conductance measurement as a small zero

bias peak (ZBP). Indeed, upon switching to a voltage biased differential conductance measurement, a small ZBP with height $\sim 0.01\frac{2e^2}{h}$ is found. The ranges in which the supercurrent is visible in a current biased measurement and in which the ZBP is visible in a voltage biased measurement are not identical due to a minor charge switch between the two measurements.

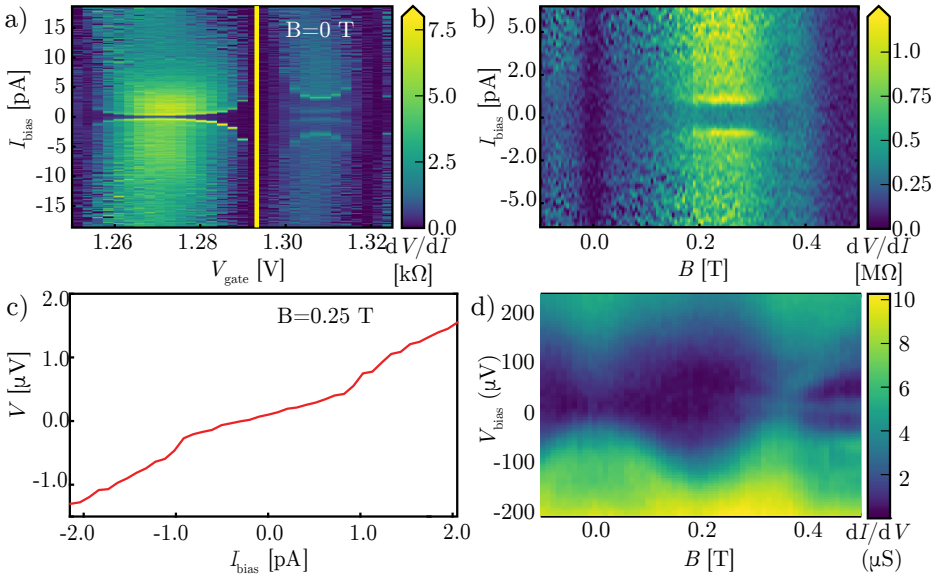

Figure 3.10: Supercurrents and zero bias peaks at finite B. a) Differential resistance vs gate. In this scan, one of the local gates is set at -0.45 V and all other gates are at +1.5 V.b) Differential resistance vs B at the indicated gate position in a). c) Linecut from b) at B = 0.25 T. d) Differential conductance vs B corresponding to b). Numerical derivative of original $V(I)$ curves is shown in a) and b). Data from device 1.

3.10. EXTRACTING SWITCHING CURRENT FROM EXPERIMENTAL DATA

To obtain Fig. 3.5(a) of the main text, switching currents are extracted from a large set of voltage-current characteristics by numerically detecting the voltage step upon switching from the superconducting to the resistive regime. First an initial low-pass filter is applied to the data reducing spurious fast fluctuations. Next, a numerical derivative of the $V(I)$-curve is taken. This first derivative has a clear maximum for an $V(I)$-curve with a sharp transition, allowing for straightforward identification of the switching current. However, the finite B-field $V(I)$-curves typically display smooth transitions from superconducting to resistive state, resulting in unclear or even absent maximums in the first derivative. A smooth transition still generates a maximum of second derivative, allowing for identification of the switching current. We therefore introduced a threshold for a first derivative maximum, below which a second derivative is taken of the $V(I)$-curve with its maximum identified as the switching current. A second threshold is introduced for the

maximum of second derivative, below which the switching current is considered to be zero. Algorithm parameters are optimized to both correctly identify the sharp transitions of large switching currents and to avoid false positives of small switching current.

3.10.1. DETAILS OF THE MODELING

The nanowire cross section has a diameter of 104 nm and the superconductor on top of the semiconductor nanowire adds two more layers of unit cells partially covering the nanowire (135° of the wire's circumference). The superconductor has the same lattice constant and effective mass as the nanowire, justified by the long-junction limit. This means that the wave function has most of its weight in the nanowire and that the superconducting shell merely serves as an effective boundary condition that ensures that all particles are Andreev-reflected. Further, the superconductor lacks the Zeeman effect and spin-orbit interaction, but has a superconducting order parameter Δ set such that the induced inside the nanowire superconducting gap at zero field is $\Delta_{\text{ind}} = 0.250\,\text{meV}$. We use realistic parameters of an InSb nanowire [4]: $\alpha = 20\,\text{meV}\cdot\text{nm}$, $m^* = 0.015 m_e$, and $g = 50$.

The geometry of the modeled system is shown in Fig. 3.11

3.10.2. DETAILED THEORETICAL ESTIMATES

In this section we estimate the strength of different possible mechanisms that can cause supercurrent oscillations in the nanowire Josephson junction.

Interference between orbital channels. The area of the cross section of the nanowire is $\sim \pi \times (50\,\text{nm})^2$. This means that the magnetic field value of $B \approx 0.26\,\text{T}$ corresponds to one flux quantum penetrating the cross section of the nanowire. At this value of the magnetic field we expect the phase shifts between different bands propagating between the two superconductors to be comparable to π. This sets the typical B scale for the interference of different orbital modes carrying current, and its value is well within the range of the experimentally observed distance between local minima and maxima of supercurrent. This simple estimate neglects the magnetic field expulsion of the superconductor, which may create a higher flux in the nanowire near the superconducting contacts, thus lowering the effective field scale.

Interference between spin channels. Supercurrent oscillations can be produced by $0-\pi$ transitions due to the Zeeman splitting of the Andreev bound states inside the Josephson junction. The characteristic B scale of such supercurrent oscillations is determined by the ratio of Zeeman energy to the Thouless energy. This sets the relative phase θ_{B} of the Andreev bound states, $\theta_{\text{B}} = E_{\text{Z}} L/\hbar v_{\text{F}}$. Here E_{Z} is the Zeeman energy, L the length of the nanowire junction, and v_{F} the Fermi velocity in the nanowire. For $\theta_{\text{B}} = \pi/2$, a $0-\pi$ transition happens, resulting in a 'cusp' in the curve of the supercurrent as function of B. Because with a small Fermi velocity θ_{B} becomes more sensitive to changes in B, given $v_{\text{F}} \approx \sqrt{2\mu/m^*}$, the lowest B value at which a $0-\pi$ transition happens is for low chemical potential. Therefore, the relevant behavior is captured within the typical μ range of the intermode spacing of $\sim 15\,\text{meV}$. Assuming a junction length of $L = 1\,\text{um}$, the B field for the first cusp to appear has an upper bound of $B \sim 0.5\,\text{T}$. Generally, for smaller μ, this value is significantly lower, therefore purely Zeeman induced su-

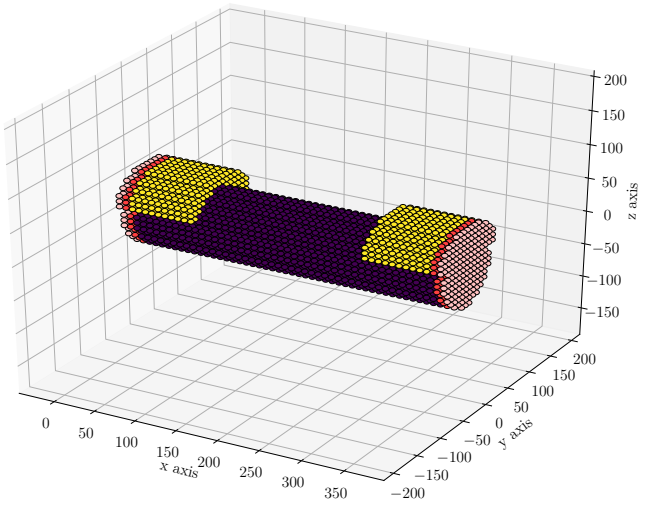

Figure 3.11: The modeled tight-binding system. The purple sites indicate the semi-conductor and the sites show the superconductor. The red and light red colored cross sections indicate that the wire extends infinitely in that direction. We defined the length of the wire L as the part that is not covered with the superconductor. In this figure for clarity we plot a shorter wire ($L = 200\,\text{nm}$), while in the simulations we chose $L = 640\,\text{nm}$. The other dimensions used in the simulations are as depicted. Specifically, the wire diameter is 104 nm, the thickness of the superconductor is $16 - 24\,\text{nm}$, and the coverage angle of the superconductor is 135°.

percurrent oscillations are well within the range of the experimental observations. These points are confirmed in our numerical simulations, see $\alpha = 0$ lines of Fig. 3.12

Interference between spin, Zeeman and spin-orbit.

The previous discussion on spin related interference considered the Zeeman effect only. However, the nanowire has a strong spin-orbit interaction as well. Following Ref. [27], the characteristic parameter for spin-orbit is $\theta_{SO} = \frac{\alpha k_F L}{\hbar v_F} = \frac{\alpha m^* L}{\hbar^2} = L/L_{SO}$. Here L_{SO} is the spin-orbit length, which is expected to be in the $50 - 250\,\text{nm}$ range, so much shorter than L. Consequentially, for the Zeeman effect to cause a $0 - \pi$ transition it needs to overcome the spin-orbit interaction, i.e. one needs to consider L_{SO} instead of L in the expression for θ_B. This increases the value of B at which the first cusp in supercurrent appears by at least a factor of ~ 5, suggesting that only for very small μ near the bottom of the mode cusps are expected. Experimentally, this would result in supercurrent variations at low B that are restricted in gate potential range. This interplay between Zeeman and spin-orbit interaction is expected to be highly anisotropic in the direction of B; the

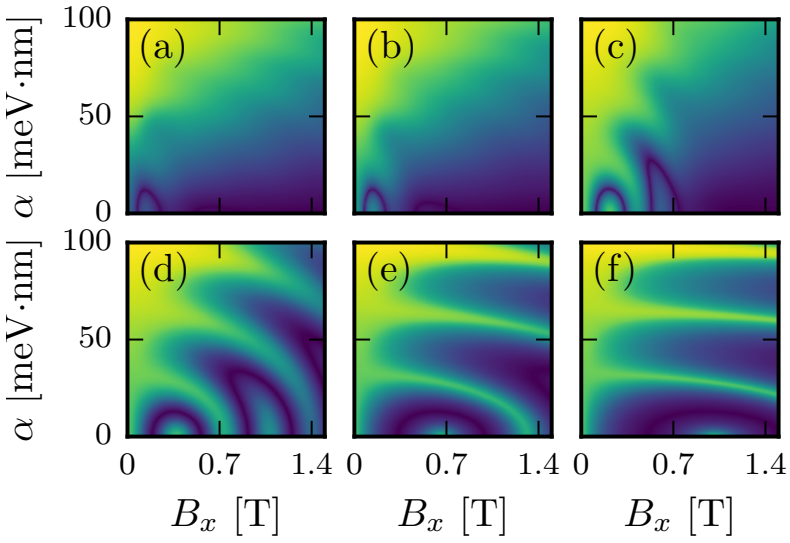

Figure 3.12: Critical currents in a simple one-dimensional toy model nanowire as a function of spin-orbit coupling strength α and magnetic field along the wire B_x. The different panels (a)-(f) are taken at different chemical potentials, 0.1, 0.3, 1, 3, 10, 30 meV respectively. The color scales are not normalized across the in the different panels, but are all separately scaled to optimally show all features in every plot. We observe how the $0-\pi$ transitions at finite B_x get mutually annihilated upon increasing α.

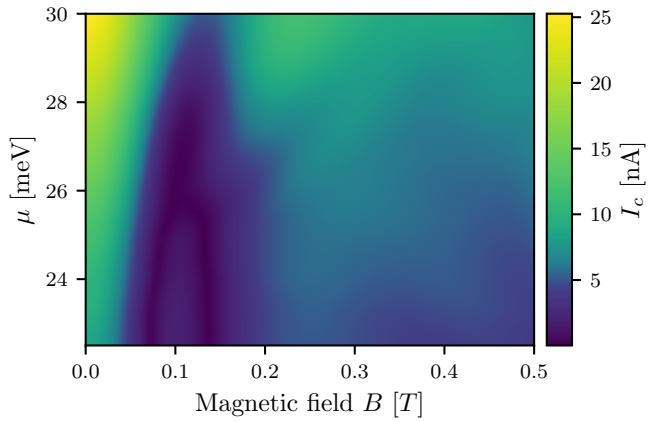

Figure 3.13: Critical current as a function of the magnetic field and the gate voltage on a gate. The simulation parameters are identical to the ones used in Fig. 5 in the main paper, except that there is no disorder.

scenario described above assumes the external B field and effective spin-orbit field to be perpendicular, as is expected for applying B along the nanowire axis. This discussion is illustrated in Fig. 3.12.

In summary, the above estimates suggest that orbital interference is present regardless of the exact value of μ, whereas spin related interference is highly restricted in μ range. This favors an orbital interference interpretation of the experimental observations, since the supercurrent variations in the experiment are present whenever there are large ranges in gate potential.

To illustrate this reasoning we produced Fig. 3.12, which shows supercurrent fluctuations as a function of the distance to the bottom of the band in a single-band wire. With increasing the distance to the bottom of the bands $0-\pi$ transitions happen at higher fields. Upon ramping up spin-orbit strength the $0-\pi$ transitions disappear.

3.10.3. ADDITIONAL ESTIMATES

EFFECT OF DISORDER

Here we prove the essential effect of disorder on the supercurrent dependence on gate voltage. For that we compare the Fig. 5b of the main text and Fig. 3.13, where we have switched off disorder. We see that in the clean case the gate voltage almost does not cause fluctuations of the supercurrent even at finite field. In the disordered case changing the gate voltage effectively changes the realization of disorder in the region of the wire above the gate, thus causing the supercurrent fluctuations. In the clean case the main effect of the gate is in gradual suppressing transmission through the wire.

ROTATING MAGNETIC FIELD

Here we model the supercurrent fluctuations for different directions of the magnetic field, from parallel to the wire to perpendicular to it. The results of the modeling are in Fig. 3.14. We see that for all directions of the field, besides one perpendicular to the

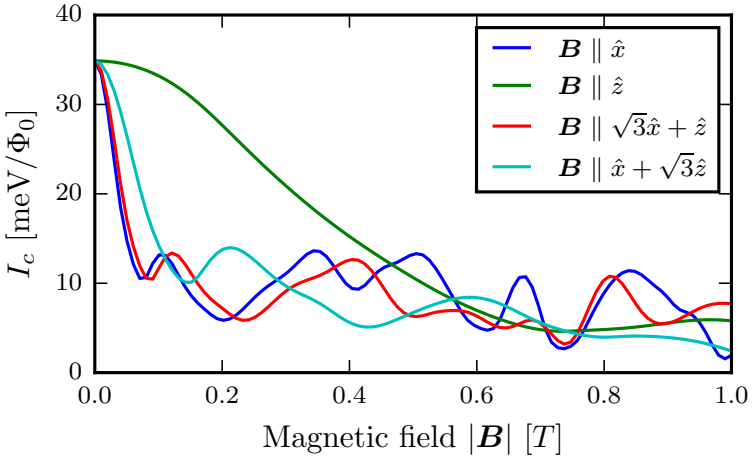

Figure 3.14: Supercurrent as a function of magnetic field for different directions of the applied field: $\hat{x}$ parallel to the wire, $\hat{z}$ perpendicular to the wire and to the substrate. We use the same parameters as in Fig. 5 of the main text. Besides the field purely along $\hat{z}$ the fluctuations pattern is qualitatively similar in all the directions.

wire, the fluctuation pattern is basically the same. This is in accordance with the experimental observations of Fig. 3.8

BIBLIOGRAPHY

[1] A. Y. Kitaev, "Unpaired majorana fermions in quantum wires," *Physics-Uspekhi*, vol. 44, no. 10S, p. 131, 2001.

[2] Y. Oreg, G. Refael, and F. von Oppen, "Helical liquids and majorana bound states in quantum wires," *Phys. Rev. Lett.*, vol. 105, p. 177002, Oct 2010.

[3] R. M. Lutchyn, J. D. Sau, and S. Das Sarma, "Majorana fermions and a topological phase transition in semiconductor-superconductor heterostructures," *Phys. Rev. Lett.*, vol. 105, p. 077001, Aug 2010.

[4] V. Mourik, K. Zuo, S. M. Frolov, S. R. Plissard, E. P. A. M. Bakkers, and L. P. Kouwenhoven, "Signatures of majorana fermions in hybrid superconductor-semiconductor nanowire devices," *Science*, vol. 336, no. 6084, pp. 1003–1007, 2012.

[5] M. Deng, C. Yu, G. Huang, M. Larsson, P. Caroff, and H. q. Xu, "Anomalous zero-bias conductance peak in a nb-insb nanowire-nb hybrid device," *Nano Letters*, 2012.

[6] M. Deng, S. Vaitiekėnas, E. Hansen, J. Danon, M. Leijnse, K. Flensberg, J. Nygård, P. Krogstrup, and C. Marcus, "Majorana bound state in a coupled quantum-dot hybrid-nanowire system," *Science*, vol. 354, no. 6319, pp. 1557–1562, 2016.

[7] S. M. Albrecht, A. Higginbotham, M. Madsen, F. Kuemmeth, T. S. Jespersen, J. Nygård, P. Krogstrup, and C. Marcus, "Exponential protection of zero modes in majorana islands," *Nature*, vol. 531, no. 7593, pp. 206–209, 2016.

[8] J. Chen, P. Yu, J. Stenger, M. Hocevar, D. Car, S. R. Plissard, E. P. Bakkers, T. D. Stanescu, and S. M. Frolov, "Experimental phase diagram of a one-dimensional topological superconductor," *arXiv preprint arXiv:1610.04555*, 2016.

[9] J. Wiedenmann, E. Bocquillon, R. Deacon, S. Hartinger, O. Herrmann, T. M. Klapwijk, L. Maier, C. Ames, C. Brüne, C. Gould, A. Oiwa, K. Ishibashi, S. Tarucha, H. Buhmann, and L. W. Molenkamp, "4π-periodic josephson supercurrent in hgte-based topological josephson junctions," *Nature Communications*, vol. 7, 2015.

[10] E. Bocquillon, R. S. Deacon, J. Wiedenmann, P. Leubner, T. M. Klapwijk, C. Brüne, K. Ishibashi, H. Buhmann, and L. W. Molenkamp, "Gapless andreev bound states in the quantum spin hall insulator hgte," *Nature Nanotechnology*, vol. 12, pp. 137—-143, 2016.

[11] R. S. Deacon, J. Wiedenmann, E. Bocquillon, F. Domínguez, T. M. Klapwijk, P. Leubner, C. Brüne, E. M. Hankiewicz, S. Tarucha, K. Ishibashi, H. Buhmann, and L. W. Molenkamp, "Josephson radiation from gapless andreev bound states in hgte-based topological junctions," *arXiv: 1603.09611*, 2016.

[12] T. Hyart, B. van Heck, I. C. Fulga, M. Burrello, A. R. Akhmerov, and C. W. J. Beenakker, "Flux-controlled quantum computation with majorana fermions," *Phys. Rev. B*, vol. 88, p. 035121, Jul 2013.

[13] D. Aasen, M. Hell, R. V. Mishmash, A. Higginbotham, J. Danon, M. Leijnse, T. S. Jespersen, J. A. Folk, C. M. Marcus, K. Flensberg, and J. Alicea, "Milestones toward majorana-based quantum computing," *Phys. Rev. X*, vol. 6, p. 031016, Aug 2016.

[14] T. Karzig, C. Knapp, R. M. Lutchyn, P. Bonderson, M. B. Hastings, C. Nayak, J. Alicea, K. Flensberg, S. Plugge, Y. Oreg, C. M. Marcus, and M. H. Freedman, "Scalable designs for quasiparticle-poisoning-protected topological quantum computation with majorana zero modes," *arxiv: 1610.05289*, 2016.

[15] S. Plugge, A. Rasmussen, R. Egger, and K. Flensberg, "Majorana box qubits," *arXiv preprint arXiv:1609.01697*, 2016.

[16] Y.-J. Doh, J. A. van Dam, A. L. Roest, E. P. Bakkers, L. P. Kouwenhoven, and S. De Franceschi, "Tunable supercurrent through semiconductor nanowires," *Science*, vol. 309, no. 5732, pp. 272–275, 2005.

[17] J. A. Van Dam, Y. V. Nazarov, E. P. Bakkers, S. De Franceschi, and L. P. Kouwenhoven, "Supercurrent reversal in quantum dots," *Nature*, vol. 442, no. 7103, pp. 667–670, 2006.

[18] D. Szombati, S. Nadj-Perge, D. Car, S. Plissard, E. Bakkers, and L. Kouwenhoven, "Josephson φ_0-junction in nanowire quantum dots," *Nature Physics*, vol. 12, pp. 568—572, 2016.

[19] G. de Lange, B. van Heck, A. Bruno, D. J. van Woerkom, A. Geresdi, S. R. Plissard, E. P. A. M. Bakkers, A. R. Akhmerov, and L. DiCarlo, "Realization of microwave quantum

circuits using hybrid superconducting-semiconducting nanowire josephson elements," *Phys. Rev. Lett.*, vol. 115, p. 127002, Sep 2015.

[20] T. W. Larsen, K. D. Petersson, F. Kuemmeth, T. S. Jespersen, P. Krogstrup, J. Nygård, and C. M. Marcus, "Semiconductor-nanowire-based superconducting qubit," *Phys. Rev. Lett.*, vol. 115, p. 127001, Sep 2015.

[21] J. Paajaste, M. Amado, S. Roddaro, F. S. Bergeret, D. Ercolani, L. Sorba, and F. Giazotto, "Pb/inas nanowire josephson junction with high critical current and magnetic flux focusing," *Nano Letters*, vol. 15, no. 3, pp. 1803–1808, 2015. PMID: 25671540.

[22] J. Paajaste, E. Strambini, M. Amado, S. Roddaro, P. San-Jose, R. Aguado, F. Bergeret, D. Ercolani, L. Sorba, and F. Giazotto, "Magnetically-driven colossal supercurrent enhancement in inas nanowire josephson junctions," *arXiv: 1601.02955*, 2016.

[23] K. Gharavi, G. W. Holloway, R. R. LaPierre, and J. Baugh, "Nb/inas nanowire proximity junctions from josephson to quantum dot regimes," *arXiv:1611.08653*, 2016.

[24] E. A. Demler, G. Arnold, and M. Beasley, "Superconducting proximity effects in magnetic metals," *Physical Review B*, vol. 55, no. 22, p. 15174, 1997.

[25] A. Buzdin, L. Bulaevskii, and S. Panyukov, "Critical-current oscillations as a function of the exchange field and thickness of the ferromagnetic metal (f) in an sfs josephson junction," *JETP Lett*, vol. 35, no. 178, pp. 103–104, 1982.

[26] L. Bulaevskii, V. Kuzii, and A. Sobyanin, "Superconducting system with weak coupling to the current in the ground state," *JETP lett*, vol. 25, no. 7, pp. 290–294, 1977.

[27] T. Yokoyama, M. Eto, and Y. V. Nazarov, "Anomalous josephson effect induced by spin-orbit interaction and zeeman effect in semiconductor nanowires," *Physical Review B*, vol. 89, no. 19, p. 195407, 2014.

[28] S. Nadj-Perge, V. Pribiag, J. Van den Berg, K. Zuo, S. Plissard, E. Bakkers, S. Frolov, and L. Kouwenhoven, "Spectroscopy of spin-orbit quantum bits in indium antimonide nanowires," *Physical review letters*, vol. 108, no. 16, p. 166801, 2012.

[29] I. Van Weperen, B. Tarasinski, D. Eeltink, V. Pribiag, S. Plissard, E. Bakkers, L. Kouwenhoven, and M. Wimmer, "Spin-orbit interaction in insb nanowires," *Physical Review B*, vol. 91, no. 20, p. 201413, 2015.

[30] I. van Weperen, S. R. Plissard, E. P. Bakkers, S. M. Frolov, and L. P. Kouwenhoven, "Quantized conductance in an insb nanowire," *Nano letters*, vol. 13, no. 2, pp. 387–391, 2012.

[31] J. Kammhuber, M. C. Cassidy, H. Zhang, O. Gül, F. Pei, M. W. de Moor, B. Nijholt, K. Watanabe, T. Taniguchi, D. Car, *et al.*, "Conductance quantization at zero magnetic field in insb nanowires," *Nano letters*, vol. 16, no. 6, pp. 3482–3486, 2016.

[32] P. San-Jose, E. Prada, and R. Aguado, "Mapping the topological phase diagram of multiband semiconductors with supercurrents," *Physical review letters*, vol. 112, no. 13, p. 137001, 2014.

[33] H. Zhang, O. Gül, S. Conesa-Boj, K. Zuo, V. Mourik, F. K. de Vries, J. van Veen, D. J. van Woerkom, M. P. Nowak, M. Wimmer, D. Car, S. R. Plissard, E. P. A. M. Bakkers, M. Quintero-Pérez, S. Goswami, K. Watanabe, T. Taniguchi, and L. P. Kouwenhoven, "Ballistic majorana nanowire devices," *arxiv: 1603.04069*, 2016.

[34] J. Chen, P. Yu, J. Stenger, M. Hocevar, D. Car, S. R. Plissard, E. P. Bakkers, T. D. Stanescu, and S. M. Frolov, "Experimental phase diagram of a one-dimensional topological superconductor," *arxiv: 1610.04555*, 2016.

[35] D. R. Hofstadter, "Energy levels and wave functions of Bloch electrons in rational and irrational magnetic fields," *Phys. Rev. B*, vol. 14, pp. 2239–2249, Sept. 1976.

[36] V. P. Ostroukh, B. Baxevanis, A. R. Akhmerov, and C. W. J. Beenakker, "Two-dimensional josephson vortex lattice and anomalously slow decay of the fraunhofer oscillations in a ballistic sns junction with a warped fermi surface," *Phys. Rev. B*, vol. 94, p. 094514, Sep 2016.

[37] C. W. Groth, M. Wimmer, A. R. Akhmerov, and X. Waintal, "Kwant: a software package for quantum transport," *New J. Phys.*, vol. 16, p. 063065, June 2014.

[38] A. Buzdin, "Peculiar properties of the josephson junction at the transition from 0 to π state," *Physical Review B*, vol. 72, no. 10, p. 100501, 2005.

[39] A. Vuik, D. Eeltink, A. R. Akhmerov, and M. Wimmer, "Effects of the electrostatic environment on the majorana nanowire devices," *New Journal of Physics*, vol. 18, no. 3, p. 033013, 2016.

[40] H. Courtois, M. Meschke, J. Peltonen, and J. P. Pekola, "Origin of hysteresis in a proximity josephson junction," *Physical review letters*, vol. 101, no. 6, p. 067002, 2008.

[41] R. C. Dinsmore III, M.-H. Bae, and A. Bezryadin, "Fractional order shapiro steps in superconducting nanowires," *Applied physics letters*, vol. 93, no. 19, p. 192505, 2008.

[42] H. Sellier, C. Baraduc, F. m. c. Lefloch, and R. Calemczuk, "Half-integer shapiro steps at the $0-\pi$ crossover of a ferromagnetic josephson junction," *Phys. Rev. Lett.*, vol. 92, p. 257005, Jun 2004.

[43] Z. Radović, L. Dobrosavljević-Grujić, and B. Vujičić, "Coexistence of stable and metastable 0 and π states in josephson junctions," *Phys. Rev. B*, vol. 63, p. 214512, May 2001.

[44] M. T. Deng, C. L. Yu, G. Y. Huang, M. Larsson, P. Caroff, and H. Q. Xu, "Parity independence of the zero-bias conductance peak in a nanowire based topological superconductor-quantum dot hybrid device," *Scientific reports*, vol. 4, 2014.

[45] A. D. Finck, D. J. Van Harlingen, P. K. Mohseni, K. Jung, and X. Li, "Anomalous modulation of a zero-bias peak in a hybrid nanowire-superconductor device," *Physical review letters*, vol. 110, no. 12, p. 126406, 2013.

4

SUPERCONDUCTING INSB NANOCROSS

Signatures of Majorana fermions have recently been reported from measurements on hybrid superconductor-semiconductor nanowire devices. Majorana fermions are predicted to obey special quantum statistics, known as non-Abelian statistics. To probe this requires an exchange operation, in which two Majorana fermions are moved around one another, which requires at least a simple network of nanowires. Here, we report on the electrical characterization of crosses of InSb nanowires. The InSb wires grow horizontally on flexible vertical stems, allowing nearby wires to meet and merge. In this way, near-planar single-crystalline nanocrosses are created, which can be measured by four electrical contacts. Our transport measurements show that the favourable properties of the InSb nanowire devices-high conductance and the ability to induce superconductivity-are preserved in the cross devices. Our nanocrosses thus represent a promising system for the exchange of Majorana fermions.

In collaboration with I. van Weperen, D. Car, M. A. Verheijen, G. W. G. Immink, J. Kammhuber, L. J. Cornelissen, A. Geresdi, S. M. Frolov, L. P. Kouwenhoven and E. P. A. M. Bakkers.
Parts of this chapter has been published in Nature Nanotechnology **8** 859 (2013).

4.1. INTRODUCTION

Majorana fermions[1] can arise as pairs of quasi-particles located at the ends of a semiconductor nanowire in contact with a superconductor[2–4]. Interestingly, the quantum properties of Majorana fermions are expected to be protected by topology, becoming insensitive to perturbations, which could make them robust quantum bits[5–7]. Logical operations can be performed by exchanging the positions of two Majorana fermions, that is, by braiding, thereby exploiting their non-Abelian exchange statistics[8]. Following proposals in refs [9] and [10], signatures of Majorana fermions were recently detected in a one-dimensional semiconductor nanowire (with strong spin–orbit interactions) in contact with a superconductor[2–4]. However, currently available single-nanowire devices are not suitable for demonstrating braiding, because Majorana fermions annihilate when they come into close proximity with one another. Recent theories have proposed the use of nanowire junctions to make braiding possible[11–14], by temporarily storing one Majorana fermion in an auxiliary leg of a T-junction while moving the other particle across, or by using a flux-controlled interaction between Majorana fermions in a double T-junction.

Braiding of Majorana fermions imposes three strong requirements on the semiconductor materials. First, to generate Majoranas the material should exhibit strong spin-orbit coupling. Second, the branched wires must form a planar structure to enable electronic device fabrication by standard lithography. Finally, the branched structures should be of high crystalline quality, because for Majorana particles it is important to have nearly ballistic transport, and defects in the wires and at the interface will induce unwanted Majoranas. Despite continuous progress in the control and understanding of nanowire growth[15–17], there are only a few studies that focus on three-dimensional branched nanowire networks[18–24]. Here, we study electric transport through InSb T- and X-shaped nanostructures grown from the strong spin–orbit coupling semiconductor InSb, using a vapour-liquid-solid (VLS) mechanism[25] and gold as the catalyst. We show that the junctions have high conductance and supercurrents can be established through all branches of a nanocross despite extremely long junction, thus these structures can be considered as an ideal platform for future braiding experiments.

4.2. NANOWIRE GROWTH

The initial step to grow InSb nanocrosses are similar to growing single wires: an InAs stem is grown on an InP substrate (Fig. 4.1**a**) in MOVPE chamber via the VLS mechanism[26]. The InAs stem is then partially evaporated such that the gold particle which catalyses the growth slides from the top of the stem to one of the sides (Fig. 4.1**b**), thus changing the growth direction allowing further growth of InSb parallel to the substrate instead of perpendicular (Fig. 4.1**c**). The co-planar InSb stems can merge at various angles φ depending on the relative positions of the stems, their orientation and the gold particle position on the stem (Fig. 4.1**d**). For a single crystalline interface $\varphi = 70.5°$. When φ differs from this value a grain boundary develops at the intersection of the wires. For the device presented here $\varphi \approx 90°$. More details on nanocross growth can be found in Ref [27].

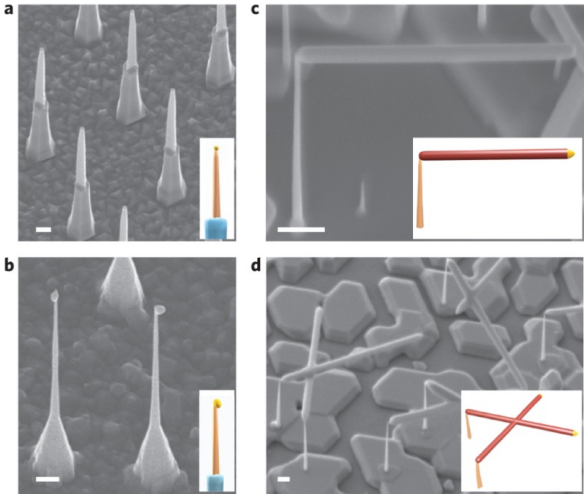

Figure 4.1: **Steps in nanocross growth. a,** A 30° tilted SEM image of the InP/InAs stems. **b,** Au-In droplets on side facets after the annealing step. **c,** InSb nanowire grown parallel to the substrate surface. **d,** InSb nanocrosses resulting from the merging process between two InSb nanowires. All scale bars, 200 nm. Growth times in (a-d) are different. Insets: InP, InAs and InSb segments are in blue, orange and red, respectively, and the Au-In droplet is in yellow.

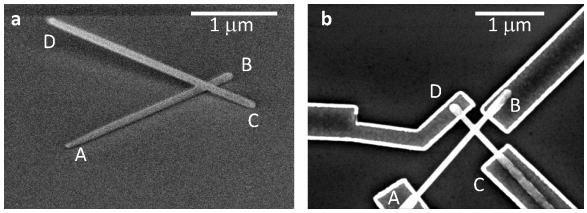

Figure 4.2: **SEM image of the measured nanocross with labelled arms. a,** nanocross on a SiO_2 substrate after deposition via the nanomanipulator (side view). **b,** nanocross after superconducting contact deposition (top view).

4.3. DEVICE FABRICATION

Following growth, the nancrosses are transferred from the growth chip to a backgated SiO_x wafer using the nanomanipulator (Fig. 4.2**a**) and then contacts are patterned by standard ebeam lithography over all four arms of the nanocross. Subsequently the contact area is etched in an Ar-plasma environment and the contacts are sputtered both in-situ (see Appendix B for methods). For the particular device in this chapter we sputtered NbTiN followed by an Al capping layer with approximate thickness 50nm / 70 nm. We thus obtain a cross device with four contacts, with three nearly equal and one longer branch (Fig. 4.2**b**). After sample fabrication the device is mounted and cooled down in a 20 mK base temeperature dilution refrigerator equipped with high frequency noise filtering where DC and low frequency lock-in measurements are performed.

Let us label the four contacts of the device A-D as shown in 4.2. We measure elec-

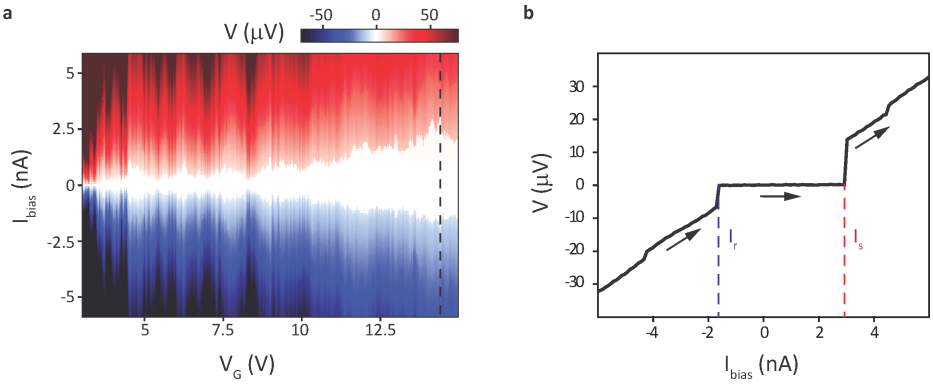

Figure 4.3: **Current biased measurement through contacts B-D. a,** Measured voltage as a function of current bias and V_G. The white region of zero resistance indicates the wire is superconducting. **b,** Measured voltage as a function of current bias for V_G = 14.4V (vertical cut from **a**). Arrows signal the direction of the current bias sweep. Switching and retrapping currents I_s and I_r are indicated.

tron transport through the device by applying a current/voltage bias to two arms while the other two arms are floating. We tune the electron density of our nanocross via the applied voltage V_G over our global back gate.

4.4. SUPERCURRENT MEASUREMENTS

First we investigate whether supercurrent can flow through our cross: we apply a current bias to two electrodes and measure the voltage difference between them. Figure 4.3 shows the voltage measured across contacts B and D as a function of the current bias and the back gate voltage. The white region in the middle of the plot is where the voltage drop over the device vanishes. This can be seen more clearly if we make a cut along a fixed back gate voltage value V_G = 14.4 V and plot the measured voltage vs current bias (Fig. 4.3**b**). We see that the switching(retrapping) current, i.e. the current bias value at which the device switches from superconducting(finite resistance) to finite resistance (superconducting), and thus the critical current, is widely tunable with the back gate.

We extract this switching current and plot it in Figure 4.4 as a function of V_G with the switching current for the three other contact pairs not involving contact A. The three curves look qualitatively the same, and even the smaller scale fluctuations in I_s can be matched for the red and the black curve (contacts B-C and B-D). For these two paths the current flows through the joint of the nanocross whereas C-D involves a single wire junction section. The strong similarities in I_s as a function of V_G suggests that the joining does affect the electron transport, however the switching current values are of the same order as for the single wire section, implying the lack of a potential barrier at the intersection point.

We were also interested to see if any sign of superconductivity could be measured through the longer junction A-C. To observe non-linearities in the V-I relation through the long branch a we measure the differential resistance via a lock-in amplifier. Figure

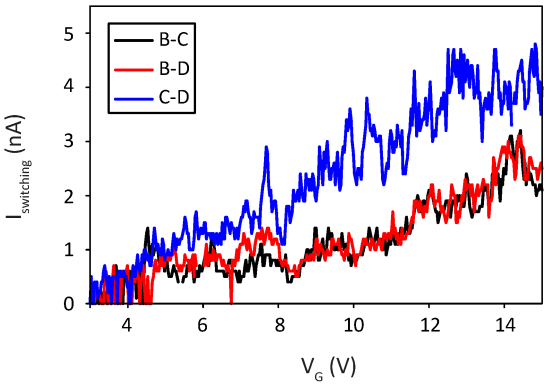

Figure 4.4: **Switching currents for three pairs of contacts as a function of V_G**

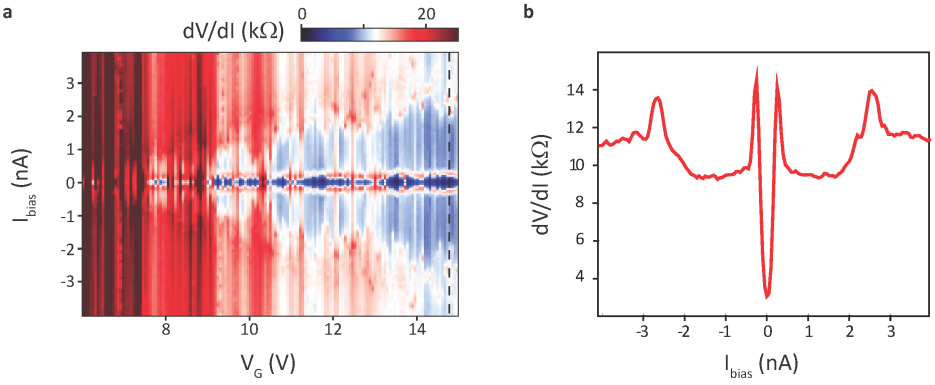

Figure 4.5: **Differential resistance measurement for contacts A-C. a,** $\frac{dV}{dI}$ as a function of current bias and V_G. The deep-blue region indicates induced superconductivity. **b,** $\frac{dV}{dI}$ as a function of I_{bias} for V_G = 14.8 V (vertical cut from a).

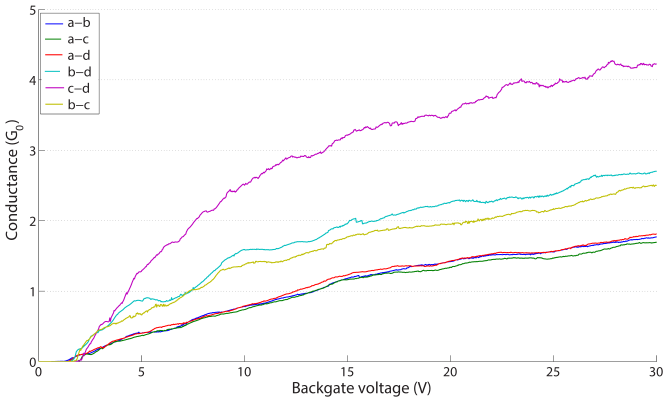

Figure 4.6: **Measured current as a function of backgate V_G for all six contact pairs.** Each gate curve is taken at a constant voltage bias of V_{bias} = 10 mV. A series resistance of 7 kΩ has been subtracted.

4.5 shows $\frac{dV}{dI}$ measured as a function of V_G. As the back gate voltage is increased, a region develops where the differential resistance of the junction for low current bias is substantially smaller than for high bias, although the resistance does not drop to zero (see Fig. 4.5**b**). This is a clear sign of phase diffusion where the junction is superconducting but its Josephson energy is not large enough to fix the phase across the superconducting leads. In the phase diffusive regime the switching current can be substantially lower than the critical current [28], but this still allows us to give a lower estimate of E_J. If we assume that for $I_s \simeq 0.25$ nA our I_c is not larger than 2.5 nA (i.e. an order of magnitude difference as in Ref. [28]) we obtain $E_J = \hbar \frac{I_c}{2e} \simeq 5\mu$eV. This value of E_J is comparable to $k_b T_{electron}$ and thus we do expect phase diffusion in our Josephson junction due to temperature. However it is still remarkable that a finite E_J and hence phase coherence can be established across contacts A and C making a 1.5 μm long JJ.

4.5. VOLTAGE BIAS SPECTROSCOPY

We also performed voltage bias measurements over our nanocross to extract information about the normal state conductance of our device. First we apply a 10 mV bias over each contact pair of our cross and measure the current passing through. We plot in Figure4.6 the conductance $G = \frac{I_{measured}}{V_{bias}}$ vs V_g for all six combination of contact pairs.

All conductance curves saturate for $V_g > 25$V and go to zero for $V_g < 2$V, hence the nanocross can be completely pinched off. This implies that our junction is fully semiconducting and with no metallic links between contacts. The three conductance curves related to the long brach a saturate at a lower conductance value (1.8 g_0) than the curves related to the shorter branches of the cross, suggesting that the resistance across the nanowire junctions is dominated by the nanowire segment instead of the contact resistance of the electrodes. The maximum conductance for the other branches are comparable to the conductance measured in single nanowires of similar length. More importantly, the maximum conductance through all branches exceeds the conductance quantum g_0, hence there is no hard constriction at the crossing point which could cre-

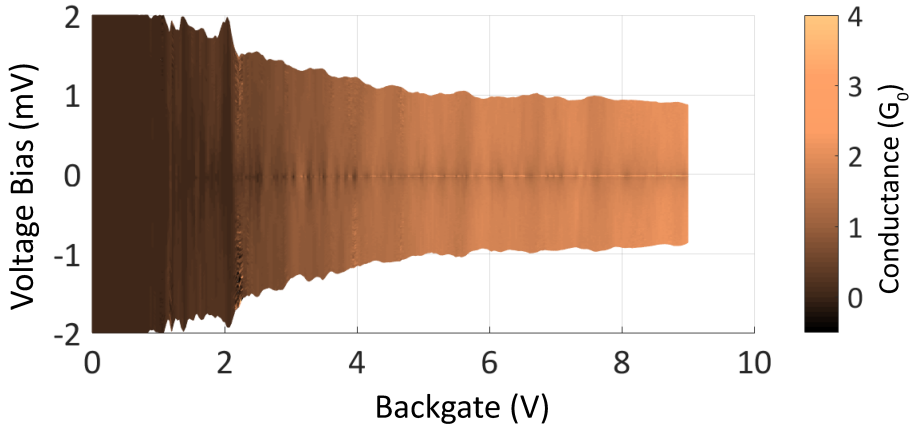

Figure 4.7: **Measured differential conductance for contact pair b-d as a function of backgate V_G and bias V_{bias}.** The bright peak at zero bias reveals that the wire segment is superconducting. A series resistance of 7 kΩ has been subtracted.

ate a quantum dot and would limit the conductance through the crossing.

We further investigate if any quantum dot features can be found in the nanocross by measuring the differential conductance $\frac{dI}{dV}$ across contacts B and D as a function of V_{bias} and V_g (Figure4.7). For $V_g > 1$V, $\frac{dI}{dV}$ does not go to zero even for small V_{bias} and there is no indication of Coulomb diamond features, indicating that the crossing is transparent and no barrier is present.

4.6. SUITABILITY FOR BRAIDING MAJORANA ZERO MODES

We now discuss our results on nanocrosses in the context of using them as a platform for braiding Majorana bound states. Several schemes were suggested to achieve braiding [11–14] in nanowire networks. They commonly rely on the wide-range tuning of the Josephson energy between two neighbouring topologically non-trivial pieces of nanowire. We rely on Ref. [14] for our discussion: the braiding operation is realized by turning the coupling on and off between a series of bulk superconductors and Majorana islands in the correct sequence. The coupling is ideally on if $\frac{E_J}{E_C} \to \infty$ and ideally off if $\frac{E_J}{E_C} = 0$. This is of course only a theoretical limit and the error of the braiding operation is of the order $\mathcal{O}(\exp(-\sqrt{8\frac{E_J}{E_C}})$. As pointed out in Ref. [14] a ratio of $\frac{E_J}{E_C} \approx 15$ should already provide suitable time frames to perform the braiding sequence.

Since we want to braid in a dilution refrigerator with an electron temperature less than 50 mK, we would like $E_C \geq 0.25$ K which implies $E_J \sim 4$ K is necessary for braiding. This translates to a critical current of the JJ of $I_C = \frac{2eE_J}{\hbar} = 170$ nA.

While in the device presented in this chapter the critical currents are 2 orders of magnitude less then required, in single junction devices we have already achieved promising I_C values of 150 nA. As discussed in the following section, E_J can be increased by improv-

ing nanocross mobilities, fabricating higher transparency superconductor/nanowire contacts and designing shorter JJs.

4.7. CONCLUSION

In conclusion, we have induced superconductivity in a four terminal InSb nanocross and performed voltage biased spectroscopy. The measured finite supercurrent across all branches of the cross, including through a wire section more than 1.5 um long, indicates that phase coherence in our NC $l \approx 3$ μm. Voltage biased spectroscopy revealed that there is no barrier or quantum dot formed in our system.

Although we measured a sizable critical current through the NC it is not large enough to perform braiding operations with the current technology. Future experiments should focus on improving the yield of NC devices and increasing the critical current above 150 nA for each branch.

BIBLIOGRAPHY

[1] E. Majorana, "Theory of the symmetry of electrons and positrons," *Nuovo Cim*, vol. 14, no. 171, p. 50, 1937.

[2] V. Mourik, K. Zuo, S. M. Frolov, S. R. Plissard, E. P. a. M. Bakkers, and L. P. Kouwenhoven, "Signatures of Majorana Fermions in Hybrid Superconductor-Semiconductor Nanowire Devices," *Science*, vol. 336, pp. 1003–1007, May 2012.

[3] A. Das, Y. Ronen, Y. Most, Y. Oreg, M. Heiblum, and H. Shtrikman, "Zero-bias peaks and splitting in an Al-InAs nanowire topological superconductor as a signature of Majorana fermions," *Nat Phys*, vol. 8, pp. 887–895, Dec. 2012.

[4] M. T. Deng, C. L. Yu, G. Y. Huang, M. Larsson, P. Caroff, and H. Q. Xu, "Anomalous Zero-Bias Conductance Peak in a Nb-InSb Nanowire-Nb Hybrid Device," *Nano Lett.*, vol. 12, pp. 6414–6419, Dec. 2012.

[5] M. Freedman, A. Kitaev, M. Larsen, and Z. Wang, "Topological quantum computation," *Bull. Amer. Math. Soc.*, vol. 40, no. 1, pp. 31–38, 2003.

[6] C. Nayak, S. H. Simon, A. Stern, M. Freedman, and S. Das Sarma, "Non-Abelian anyons and topological quantum computation," *Rev. Mod. Phys.*, vol. 80, pp. 1083–1159, Sept. 2008.

[7] A. Y. Kitaev, "Fault-tolerant quantum computation by anyons," *Annals of Physics*, vol. 303, pp. 2–30, Jan. 2003.

[8] F. Wilczek, "Majorana returns," *Nat Phys*, vol. 5, pp. 614–618, Sept. 2009.

[9] R. M. Lutchyn, J. D. Sau, and S. Das Sarma, "Majorana Fermions and a Topological Phase Transition in Semiconductor-Superconductor Heterostructures," *Phys. Rev. Lett.*, vol. 105, p. 077001, Aug. 2010.

[10] Y. Oreg, G. Refael, and F. von Oppen, "Helical Liquids and Majorana Bound States in Quantum Wires," *Phys. Rev. Lett.*, vol. 105, p. 177002, Oct. 2010.

[11] J. Alicea, Y. Oreg, G. Refael, F. von Oppen, and M. P. A. Fisher, "Non-Abelian statistics and topological quantum information processing in 1d wire networks," *Nat Phys*, vol. 7, pp. 412–417, May 2011.

[12] B. v. Heck, A. R. Akhmerov, F. Hassler, M. Burrello, and C. W. J. Beenakker, "Coulomb-assisted braiding of Majorana fermions in a Josephson junction array," *New J. Phys.*, vol. 14, no. 3, p. 035019, 2012.

[13] T. Hyart, B. van Heck, I. C. Fulga, M. Burrello, A. R. Akhmerov, and C. W. J. Beenakker, "Flux-controlled quantum computation with Majorana fermions," *Phys. Rev. B*, vol. 88, p. 035121, July 2013.

[14] D. Aasen, M. Hell, R. V. Mishmash, A. Higginbotham, J. Danon, M. Leijnse, T. S. Jespersen, J. A. Folk, C. M. Marcus, K. Flensberg, and J. Alicea, "Milestones toward Majorana-based quantum computing," *arXiv:1511.05153 [cond-mat, physics:quant-ph]*, Nov. 2015. arXiv: 1511.05153.

[15] R. E. Algra, M. A. Verheijen, M. T. Borgsträm, L.-F. Feiner, G. Immink, W. J. P. van Enckevort, E. Vlieg, and E. P. A. M. Bakkers, "Twinning superlattices in indium phosphide nanowires," *Nature*, vol. 456, pp. 369–372, Nov. 2008.

[16] C.-Y. Wen, J. Tersoff, K. Hillerich, M. C. Reuter, J. H. Park, S. Kodambaka, E. A. Stach, and F. M. Ross, "Periodically Changing Morphology of the Growth Interface in Si, Ge, and GaP Nanowires," *Phys. Rev. Lett.*, vol. 107, p. 025503, July 2011.

[17] F. Glas, J.-C. Harmand, and G. Patriarche, "Why Does Wurtzite Form in Nanowires of III-V Zinc Blende Semiconductors?," *Phys. Rev. Lett.*, vol. 99, p. 146101, Oct. 2007.

[18] K. A. Dick, K. Deppert, M. W. Larsson, T. Mårtensson, W. Seifert, L. R. Wallenberg, and L. Samuelson, "Synthesis of branched 'nanotrees' by controlled seeding of multiple branching events," *Nat Mater*, vol. 3, pp. 380–384, June 2004.

[19] S. H. Yun, J. Z. Wu, A. Dibos, X. Zou, and U. O. Karlsson, "Self-Assembled Boron Nanowire Y-Junctions," *Nano Lett.*, vol. 6, pp. 385–389, Mar. 2006.

[20] X. Jiang, B. Tian, J. Xiang, F. Qian, G. Zheng, H. Wang, L. Mai, and C. M. Lieber, "Rational growth of branched nanowire heterostructures with synthetically encoded properties and function," *PNAS*, vol. 108, pp. 12212–12216, July 2011.

[21] L. Manna, D. J. Milliron, A. Meisel, E. C. Scher, and A. P. Alivisatos, "Controlled growth of tetrapod-branched inorganic nanocrystals," *Nat Mater*, vol. 2, pp. 382–385, June 2003.

[22] X. Dai, S. A. Dayeh, V. Veeramuthu, A. Larrue, J. Wang, H. Su, and C. Soci, "Tailoring the Vapor-Liquid-Solid Growth toward the Self-Assembly of GaAs Nanowire Junctions," *Nano Lett.*, vol. 11, pp. 4947–4952, Nov. 2011.

[23] D. B. Suyatin, J. Sun, A. Fuhrer, D. Wallin, L. E. Fröberg, L. S. Karlsson, I. Maximov, L. R. Wallenberg, L. Samuelson, and H. Q. Xu, "Electrical Properties of Self-Assembled Branched InAs Nanowire Junctions," *Nano Lett.*, vol. 8, pp. 1100–1104, Apr. 2008.

[24] D. Dalacu, A. Kam, D. G. Austing, and P. J. Poole, "Droplet Dynamics in Controlled InAs Nanowire Interconnections," *Nano Lett.*, vol. 13, pp. 2676–2681, June 2013.

[25] R. S. Wagner and W. C. Ellis, "Vapor liquid solid mechanism of single crystal growth," *Applied Physics Letters*, vol. 4, pp. 89–90, Mar. 1964.

[26] S. R. Plissard, D. R. Slapak, M. A. Verheijen, M. Hocevar, G. W. Immink, I. van Weperen, S. Nadj-Perge, S. M. Frolov, L. P. Kouwenhoven, and E. P. Bakkers, "From InSb nanowires to nanocubes: looking for the sweet spot," *Nano letters*, vol. 12, no. 4, pp. 1794–1798, 2012.

[27] S. R. Plissard, I. van Weperen, D. Car, M. A. Verheijen, G. W. G. Immink, J. Kammhuber, L. J. Cornelissen, D. B. Szombati, A. Geresdi, S. M. Frolov, L. P. Kouwenhoven, and E. P. A. M. Bakkers, "Formation and electronic properties of InSb nanocrosses," *Nat Nano*, vol. 8, pp. 859–864, Nov. 2013.

[28] H. I. Jørgensen, T. Novotný, K. Grove-Rasmussen, K. Flensberg, and P. E. Lindelof, "Critical Current 0–π Transition in Designed Josephson Quantum Dot Junctions," *Nano Lett.*, vol. 7, pp. 2441–2445, Aug. 2007.

5

RESONANT ANDREEV REFLECTION THROUGH A THREE TERMINAL QUANTUM DOT

The density of states of a proximized quantum dot confined in an InSb nanocross is measured via low temperature transport. The nanowire geometry allows for three terminal dot measurement where the superconducting leads phase bias the dot while the third normal contact acts as a tunnel probe as well as an electron reservoir controlling the population of the dot states. When the dot level is tuned to the electron-hole symmetry point, we observe phase dependent Andreev current through the wire provided the empty and singlet states are filled via a sufficiently large bias on the normal lead. The oscillations survive up to 600 mT field applied along the wire, demonstrating the particular material combination of NbTiN superconductor and InSb T-junctions are suitable for Majorana braiding schemes. Our device may also be used as a flux to current converter to measure small magnetic moments at finite in-plane field.

In collaboration with A. Geresdi, D. Car, S. R. Plissard, E. P. A. M. Bakkers and L. P. Kouwenhoven.

5.1. INTRODUCTION

When a superconductor(S) is attached to a normal conductor(N), the superconducting order parameter can leak inside the normal type conductor via a phenomenon known as the proximity effect, inducing superconducting correlations and a gap in the excitation spectrum in N. Current at subgap energies is transferred through Andreev reflection process, where two electrons with opposite spin and momentum from the normal sides tunnels into the superconducting reservoir forming a Cooper pair at the Fermi level. Incorporating a low dimensional semiconductor between N and S reservoirs such as a quantum dot (QD), offers the possibility to investigate the interplay between many-body physics exerted on the electrons via the superconducting order and single electron control realized via gating the quantum dot [1–4]. More precisely, the Coulomb interactions inside the dot impose sequential filling of the dot one by one with electrons, whereas the superconducting order pairs electrons together and prefers the even spin singlet ground state. Adding a second superconducting lead allows the dot to be phase biased [5, 6] and thus provide a clear experimental signal for superconducting correlations.

Previous works on proxmized QD focused on measuring the supercurrent in the ground state [7–10] or investigating the singlet-doublet transition in both S-QD-S [11–13] and S-QD-N devices [14–16]. The low energy excitations have been probed by weakly coupling a normal lead to a proximitized QD without [17, 18] and with phase biasing [19–21]. Phase-controlled QPT from singlet to doublet has been demonstrated [22, 23]. In proximitized normal metals, effects on correlations have been reported by controlling the junction state population via normal reservoirs [24, 25]. Phase periodic DOS oscillations have also been measured in proximitized metals connected to a superconducting ring and a normal lead, a device dubbed superconducting quantum interference proximity transistor (SQUIPT)[1] [26–29]. Combining phase biasing with enhancement via injection of non-equilibrium charge carriers from normal reservoir, however, has never been done before.

Here we present results from a three terminal quantum dot formed in a T-shaped InSb nanocross with one normal lead and two superconducting leads joined in a loop. This configuration allows us to measure phase dependent transport between the normal and superconducting leads through the dot. We measure non-equilibrium phase biased Andreev current in each diamond around vanishing detuning at finite voltage, indicating a finite Josephson coupling over the dot. We can detect the oscillations up to several hundreds of milli-Teslas, making the InSb T-junction suitable for Majorana braiding experiments.

5.2. ANDREEV TUNNELING THROUGH A QD

To model the supercurrent flow through the nanowire quantum dot, we assume the QD has a single orbital of energy ϵ. The relevant energy scales determining the spin of the ground state in such a system are the dot charging energy E_C, the coupling of the dot to the leads $\Gamma = \Gamma_S + \Gamma_N$ (where Γ_S and Γ_N are the coupling to the superconducting and normal leads respectively) and the superconducting gap in the leads Δ. In the strong

[1] SQUIPTs are used as a flux to voltage and flux to current converters by making use of the flux periodic interference over the superconducting ring.

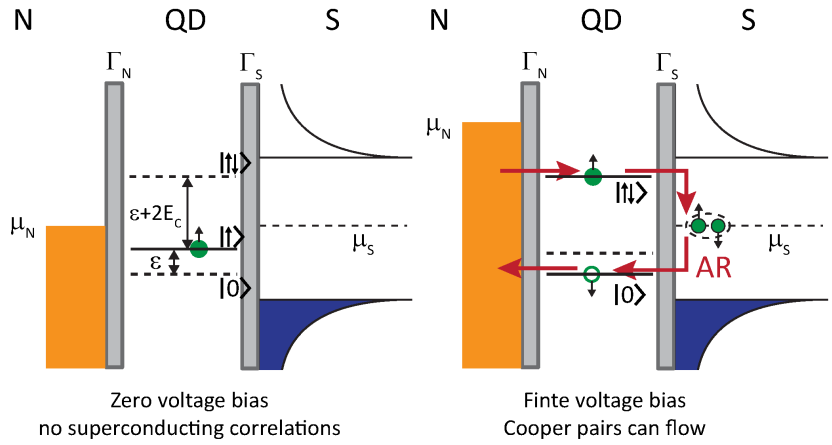

Figure 5.1: **Andreev tunneling from normal to superconducting lead via a quantum dot. a,** Dot states with $\delta = 0$ and $\mu_N = \mu_S = 0$. Only the singly occupied state is full and no Andreev current flows. **b,** Same as **a** but now $\mu_N > \mu_S$, populating the singlet $|S\rangle$ state and allowing Andreev current to flow. The $|0\rangle$ and $|\uparrow\downarrow\rangle$ states are coupled via Andreev reflection from the SC lead.

5

coupling limit $\Gamma \gg E_C, \Delta$ the singlet ground state dominates due to the Kondo effect [3].

In the opposite limit $\Gamma \ll E_C, \Delta$ the QD levels are well defined. Its four possible energy levels are $|0\rangle$, $|\uparrow\rangle$, $|\downarrow\rangle$, $|\uparrow\downarrow\rangle$ corresponding to zero electron on the dot, one electron on the dot with down spin and up spin and two electrons on the dot respectively, with energies $0, \epsilon, \epsilon, 2\epsilon + E_C$ in the absence of magnetic field. The energy of these levels with respect to the Fermi energy of the leads and hence to dot population can be controlled via gating the QD.

The coupling of the QD to the superconducting lead Γ_S proximizes the QD by pairing the zero and doubly occupied singlet states in into a Bogoliubon-like superposition spin zero state $|S\rangle = u|0\rangle - v^\star|\uparrow\downarrow\rangle$. Superconducting correlations and Andreev current are maximized therefore when the $|0\rangle$ state and the $|\uparrow\downarrow\rangle$ state are degenerate in energy, which corresponds to the condition $\delta \equiv 2\epsilon + U = 0$ where we defined the detuning δ [6]. We draw this scenario in Figure 5.1. When the detuning δ is too large a superposition of the $|0\rangle$ and $|\uparrow\downarrow\rangle$ states is not possible and no Andreev current flows.

A detunin value $\delta \approx 0$ does not guarantee a non-vanishing Andreev current, however. If the chemical potentials of the normal and the superconducting lead are equal (Figure 5.1**a**), the QD will be occupied by an odd number of electrons. Due to a finite E_C, no supercurrent can flow to first order in Γ_N. An even number of electron occupation on the QD is necessary for a superconducting pairing to arrise. This can be achieved by applying a bias on the normal lead (Figure 5.1**b**).

In summary, for Andreev current to flow, two conditions need to be met for the QD:

- Superconducting pairing potential on the dot needs to be large, meaning the detuning $\delta \approx 0$. The detuning can be adjusted via the backgate V_{BG}.

- The QD must be populated by an even number of electrons. This can be achieved

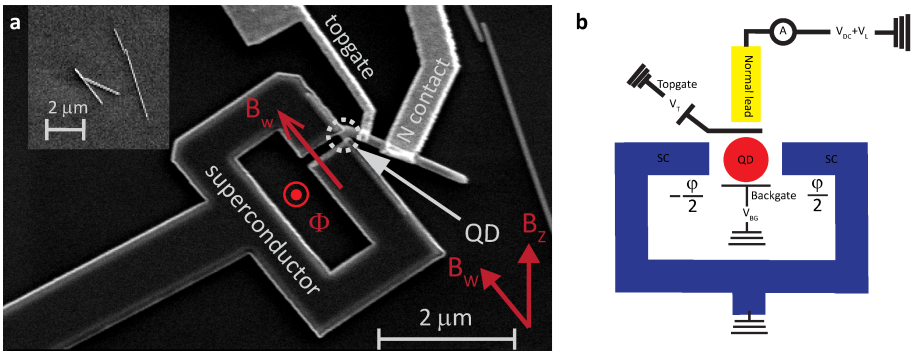

Figure 5.2: **SEM picture of the device and measurement schematics. a,** SEM picture of the three terminal device, with a gold N contact and topgate and NbTiN superconducting contacts. The direction of the applied flux, field along the wire and field along Z are shown. Inset: bare T-shaped wire before contact deposition. **b,** Measurement schematics of the experiment. The normal contact is DC biased superimposed on an AC lockin signal while the superconducting loop is grounded. Topgate voltage V_G and backgate voltage V_{BG} are used to adjust the barriers of the QD and its chemical potential. A phase drop φ is applied across the dot adjusted via the flux Φ.

by applying a finite bias V_{DC} over the dot.

5.3. DEVICE FABRICATION AND EXPERIMENTAL SETUP

The InSb nanowire crosses were grown by merging individual nanowires grown on an InP substrate with an InAs stem in an MOVPE chamber, as describe in Reference [30]. Cross wires are transferred from the growth chip via nanomanipulator to a SiO substrate with Si doped backgate. We use a T-shaped wire with three legs (see inset of Figure 5.2**a**) where the long section is used to contact with two superconductors and the third leg is used as the normal tunnel probe. First superconducting contacts are defined via Ebeam lithography in a loop shape, leaving a 150 nm sized gap at the wire intersection. The contacts are in-situ Ar etched before sputtering NbTiN of thickness 120 nm. The normal contact is fabricated similarly but is evaporated Ti/Au. Finally the top gate also made of Ti/Au is evaporated (no Ar etch).

The device is measured in a dilution fridge including electric filtering, with base electron temperature 100 mK .

We apply a DC voltage bias V_{DC} superimposed on an AC oscillation provided by a lockin amplifier V_{AC} on the normal lead while the superconducting leads are grounded. This allows us to measure simultaneously the current through the dot as well as the differential conductance $\frac{dI}{dV}$ as shown in the schematics in Figure 5.2**b**.

A 3D vector magnet firstly allows us to impose a flux Φ through the SQUID, guaranteeing a phase difference $\varphi = \frac{2\pi}{\Phi_0}\Phi$ over the quantum dot. Secondly, the magnet imposes an in-plane field B_w along the wire. Large fields beyond 1 T are applicable along the magnet Z axis, lying in plane of the substrate at 29.5° to B_w.

The QD level energy ϵ and superconducting coupling Γ_S can be tuned with the backgate voltage V_G and the coupling to the normal side Γ_N is tuned via the topgate voltage V_T.

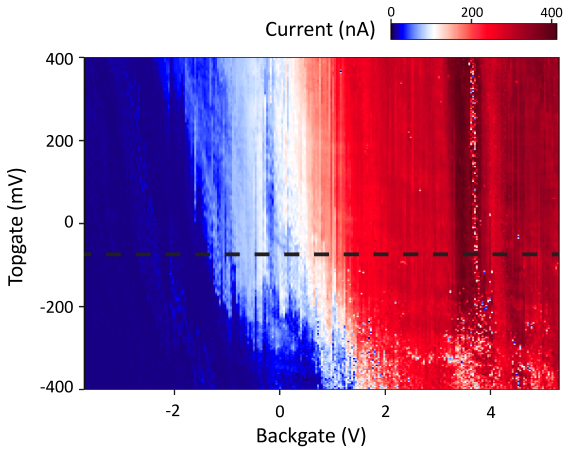

Figure 5.3: **Current as a function of topgate vs backgate at constant voltage bias.** The voltage bias is fixed to $V_{DC} = 2$ mV. The dashed line is a cut at $V_T = -70$ mV where the topgate voltage is set for the rest of the measurements.

5.4. COULOMB DIAMOND MEASUREMENTS

At a constant voltage bias $V_{DC} = 2$ mV over the dot, we measure the current as a function of topgate and backgate voltage, presented in Figure 5.3. The current responds to both V_T and V_{BG}, showing both gates couple to the dot as required. For very negative topgate voltages the device becomes unstable as it is visible from the charge jumps in the lower right half of the plot.

For the following measurements we choose a value for V_T as low as possible with the device still stable, in order to minimize Γ_N so the level broadening is not too large. The value $V_T = -70$ mV is suitable. Hereafter V_T is unchanged to minimize noise through the device.

By applying a large magnetic field of 9T in the Z-direction the dot can be driven normal and the differential conductance map reveals diamonds closing at periodic backgate values (Figure 5.4**a**). The diamonds allow to estimate the charging energy $E_C \approx 300\mu eV$, as well as the coupling strengths Γ_N, Γ_S. Following Reference [17], the Coulomb peak at $V_{DC} = 0$ is fitted to the Breit-Wigner conduction lineshape defined by the formula

$$G(\Delta V_{BG}) = \frac{e^2}{h} \frac{\Gamma_N \Gamma_S}{\Delta E^2 + (\Gamma_N + \Gamma_S)^2/4} \tag{5.1}$$

where $\Delta E = -e\alpha(V_{BG} - V_{BG}^0)$, α being the leverarm. We obtain $\Gamma_S \approx 50$ μeV,$\Gamma_N \approx 1$ μeV (Figure 5.4**b**). Since $\Delta^\star > \Gamma$ we do not expect any Kondo physics which is in agreement with the lack of a zero-bias conductance peak at $V_{DC} = 0$.

We plot the differential conductance $\frac{dI}{dV}$ as a function of voltage bias and V_{BG} at zero magnetic field in Figure 5.5**a**. The conductance shows Coulomb diamond features typical for quantum dots. A finite induced gap of size 200 μV(Figure 5.5**b**) in the differential conductance at the charge degeneracy point indicates the presence of the proximity effect on the dot.

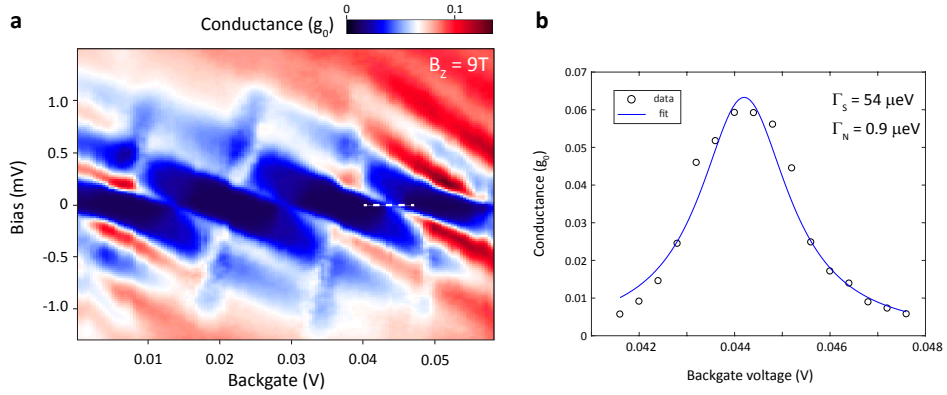

Figure 5.4: **Coulomb diamond measurement where QD leads are driven normal by applying an in-plane magnetic field of 9T. a,** Differential conductance measurement as a function of volage bias and backgate. Dashed line shows the cut at zero bias presente in the adjacent panel. **b,** Fitting the Coulomb peak via the Breit-Wigner formula. The extracted coupling strengths $\Gamma_{S,N}$ are shown.

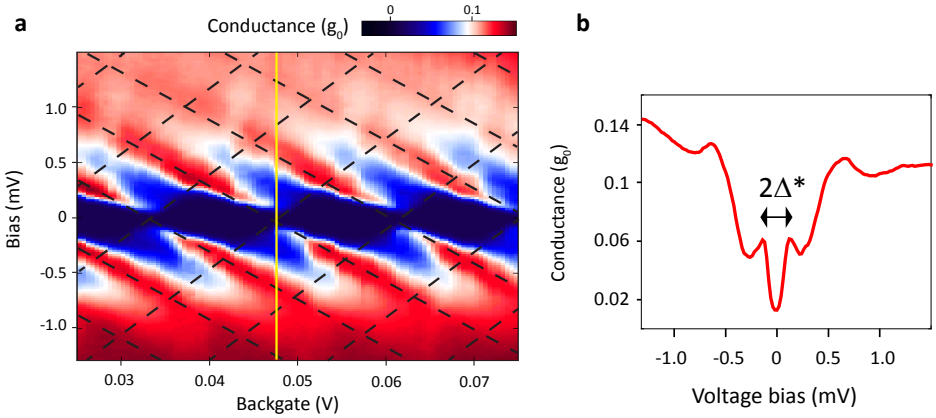

Figure 5.5: **Voltage bias scan of the Coulomb diamonds at zero-field. a,** Differential conductance measured as a function of voltage bias V_{DC} vs backgate V_{BG}. The dashed lines are guides to the eye for the edges of the diamonds. Yellow line shows linecut in (b). **b,** Line cut from the scan in (a) at fixed V_{BG}. The dip in conductance around zero bias reveals an induced superconducting gap in the dot DOS.

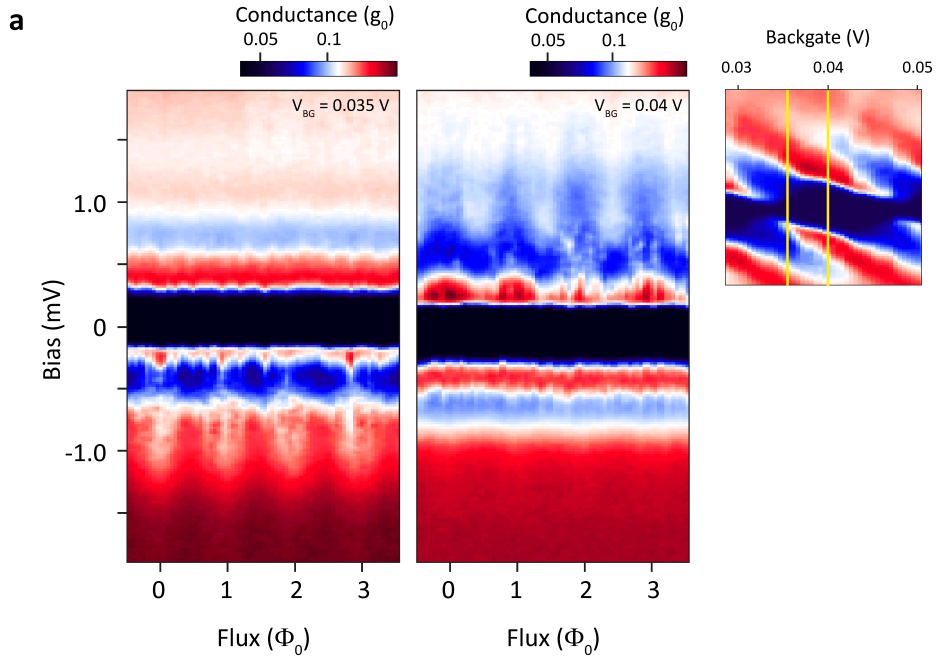

Figure 5.6: **Voltage bias vs flux for different backgate voltages showing oscillations periodic with the flux quantum.** Measured conductance as a function of voltage bias V_{DC} and flux Φ. Left panel shows flux periodic oscillations below -200 μV bias, while the middle panel shows oscillations for positive bias above 200 μV. Right panel is a cut from Figure 5.5**a** showing backgate values of the left and middle panel.

5.5. PHASE-DRIVEN NON-EQUILIBRIUM AR

We now measure $\frac{dI}{dV}$ as a function of voltage bias and flux φ for different values of the backgate voltage V_{BG}. In Figure 5.6 we plot these phase biased measurements for two different V_{BG} values.

For $V_{BG} = 0.035$V we observe flux periodic oscillations below $V_{DC} = -0.2$ mV. The oscillations are visible down to a bias value of $V_{DC} = -1.5$ mV. Transport is suppressed in the bias region -0.2 mV$< V_{DC} < 0.3$ mV. No oscillations are discernible for positive voltage bias.

For $V_{BG} = 0.041$ V no oscillations are visible for negative bias. On the other hand, oscillations appear at $V_{DC} \geq 0.18$ mV and are visible up to $V_{DC} = 1.8$mV.

To ensure the oscillations are due to phase-dependent Andreev reflection, we rotate the out-of plane magnetic field angle used to ramp the flux and plot the periodicity for each angle in Figure 5.7. The period fits well the inverse cosine function $B_{period} = B_0 \cos^{-1} \alpha$ expected for a SQUID, where α is the angle normal to the plane. The minimal period $B_0 = 640\mu$T corresponds to a SQUID area of 3.2μm^2, in agreement with the geometric area 1.8μm^2 of the inner loop corrected by a penetration depth of 200 nm.

In order to map out the region in backgate and bias space where these Andreev oscillations are visible, we measure the current as a function of V_{DC} and V_{BG} at flux values

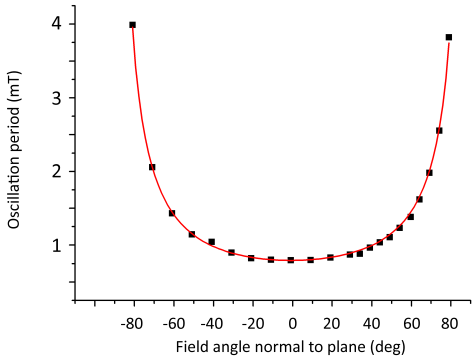

Figure 5.7: **Fit of the oscillation period as a function of the magnetic field angle normal to the plane.** Black squares are the measured period of the oscillations shown in Figure 5.6 as the magnetic field applying the flux is rotated in the plane perpendicular to the sample plane. The zero angle is normal to the sample plane. The red curve is the theoretical fit $B = B_0 \cos^{-1} \alpha$ for a SQUID with period B_0.

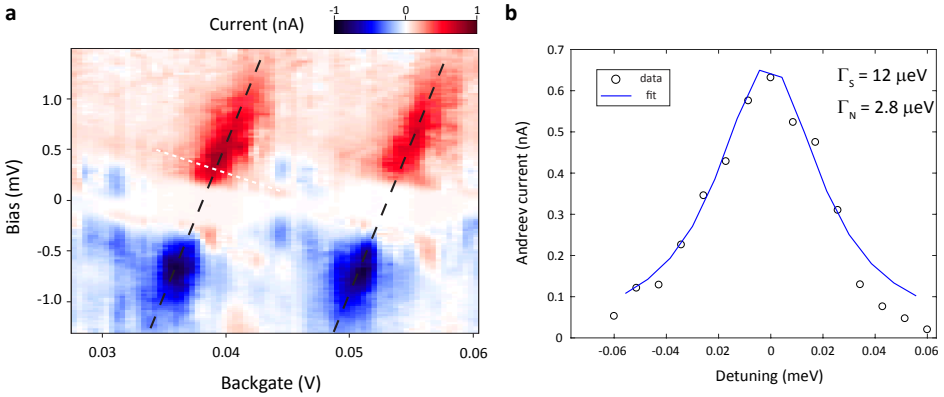

Figure 5.8: **Andreev current through the quantum dot. a,** Change in current of voltage bias vs backgate measurement for $\Phi = 0$ and $\Phi = \frac{\Phi_0}{2}$. The plot is created by measuring the current through the dot as a function of voltage bias V_{DC} and backgate V_{BG} for two different values of the flux, $\Phi = 0$ and $\Phi = \frac{\Phi_0}{2}$. The two plots are superimposed and the current values subtracted. The plot shows the difference in current for the same bias and backgate values, taken at different enclosed flux. The dashed lines are guide to the eye for the maximal current variation, i.e. where the oscillations due to Andreev current is maximum.**b,** Fitting the Andreev current using 5.2 with paramters $E_C = 0.3$meV, $V_{DC} = 0.32$meV, $\Phi = 0$ and $T = 0.1$K.

$\Phi = 0$ and $\Phi = \frac{\Phi_0}{2}$. We then subtract the current values measured at different phases and plot the difference in measured current in Figure 5.8**a**. In regions where the current does not oscillate with flux there should be no difference in the measured current, as opposed to regions where we do see Andreev oscillations.

Most of the current variation in Figure 5.8**a** lies on a fixed line $V_{DC} = \beta V_{BG}$ with in bias vs backgate space with $\beta = 0.2V/V$. This indicates that most Andreev process happen at a fixed detuning δ, or equivalently at fixed dot orbital energy. The bias also has to exceed $\pm 250\mu$V to enable the oscillations.

As mentioned before, the pairing amplitude on the dot is maximized when the detuning $\delta = 2\epsilon - E_C \approx 0$. Ideally this condition corresponds to a fixed vertical line in the V_{bias} vs V_{BG} space where $\alpha V_{BG} = \epsilon = -E_C/2$, however due to the finite capacitive coupling between the bias lead and the dot the condition changes to $\alpha(V_{BG} + \frac{C_{bias}}{C_{BG}} V_{DC}) = \epsilon = -E_C/2$.

For $|V_{bias}| < 250\ \mu$eV there is no change in current between $\Phi = 0$ and $\Phi = \frac{\pi}{2}$. This can be explained by the finite charging energy blocking transport as well as the equilibrium dot population which does not allow for Cooper pair transport as explained in section 5.2. The phase modulation is not observed above bias voltages $|V_{DC}| > 1.3$ mV, which is a reasonable estimate of the bulk gap of NbTiN. Beyond this bias window current flows via phase-independent quasiparticle states. This is in accordance with the requirements for Andreev current to flow.

As derived in Reference [5], in the regime $E_C \gg k_b T, \Gamma$ the Andreev current J_{and} can be expressed as

$$J_{and} = \frac{e\Gamma_S}{\hbar} \frac{2\Gamma_N\Gamma_S[1+\cos(\Phi)]}{4\Gamma_S^2\cos^2(\Phi/2) + (\delta + \Gamma_N B)^2 + \Gamma_N^2[1 + f(-E_C/2) - f(E_C/2)]^2} \times [1 - f(-E_C/2) - f(E_C/2)] \quad (5.2)$$

where B is a real valued function of E_C, V_{DC} and T[2]. The fitting yields tunneling coefficients $\Gamma_S = 12\ \mu$eV and $\Gamma_N = 2.8\ \mu$eV, in reasonable agreement with the coefficients obtained from fitting the Coulomb blockade peak in section 5.4.

5.6. MAGNETIC FIELD DEPENDENCE OF AR OSCILLATIONS

We now turn to measurements performed with a large in-plane magnetic field B_w and study the behavior of the Andreev oscillations.

We fix the voltage at $V_{DC} = 700\ \mu$V and scan the backgate in the range 0.035 V - 0.04 V to include the maximum of the Andreev current. We perform backgate vs flux scans to measure the current oscillations for several values of B_w. One such scan at $B_w = 300$ mT is presented in Figure 5.9**a**, with a line cut at fixed backgate in Figure 5.9**b** along with the same measurement performed at $B_w = 0$.

Although the oscillation amplitude is smaller at $B_w = 300$ mT than at $B_w = 0$ mT, the current vs flux oscillations are still substantial, demonstrating that our device can be used as a flux to current converter, or magnetic field sensor (SQUIPT) even at finite in-plane field, with a flux sensitivity of $\frac{\partial I}{\partial \Phi} \approx 1 \frac{\text{nA}}{\Phi_0}$.

To compare the oscillation amplitude of the Andreev current for increasing B_w, we take the Fourier transform of the current vs flux traces and plot the FFT amplitude vs

[2] $B = \frac{1}{\pi}\Re\left[\psi\left(\frac{1}{2} + i\frac{E_C/2 - V_{DC}}{2\pi T}\right) - \psi\left(\frac{1}{2} + i\frac{-E_C/2 - V_{DC}}{2\pi T}\right)\right]$, where $\psi(z)$ is the Digamma function.

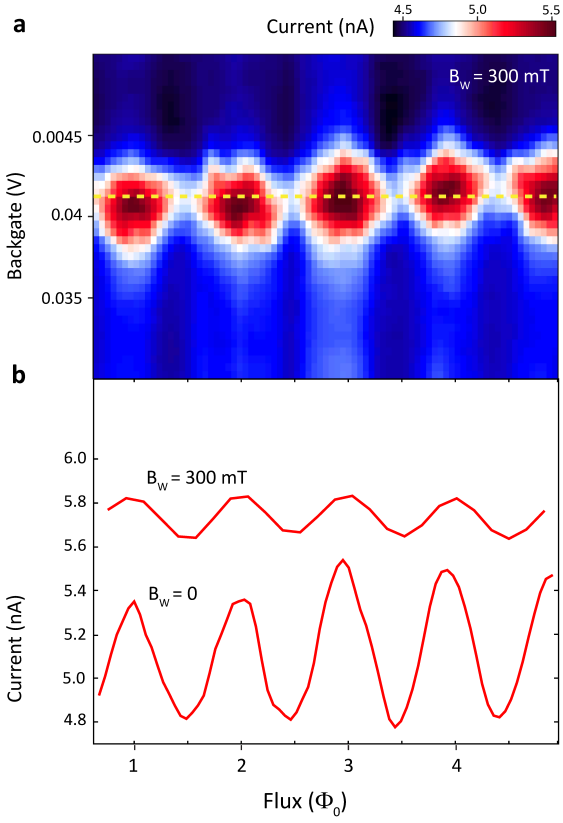

Figure 5.9: **Current as a function of backgate voltage and flux. a,**Current measurement at constant voltage bias of 700μV as a function of V_{BG} and flux at B_w = 300 mT. The oscillations are due to the constructive and destructive interference of the Andreev current. Yellow dashed line shows the cut in (b). **b,** Measured current as a function of flux Φ at fixed bias and backgate. The 300 mT curve is a vertical cut from (a) at V_{BG} = 0.042V, while the 0 mT curve is a cut from the middle panel of Figure 5.6. Although the oscillation amplitude is reduced at finite field along the wire, it is still substantial.

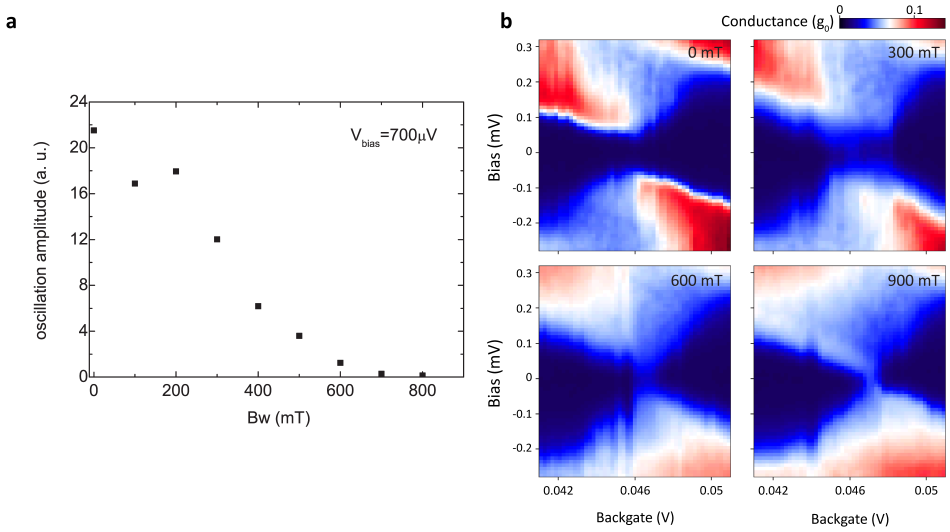

Figure 5.10: **Persisting Andreev current and superconducting gap at high mangetic field. a,**Amplitude of FFT of the oscillations as a function of magnetic field along the wire. The FFT is taken from curves shown in Figure 5.9**b** and similar measurements at different values of B_w. **b,** Closing of the induced superconducting gap at finite in-plane magnetic field. The four panels show differential conductance measurements of V_{DC} vs backgate V_{BG} in the region of the induced gap. The panels are taken at different values of B_w shown in the top right corner. The gap closes beyond $B_w = 600$ mT.

B_w in Figure 5.10**a**. We measure oscillations up to $B_w = 600$ mT. This is consistent with the field magnitude at which the minigapgap closes, which can be seen in Figure 5.10**b**, where we plot the gap for several values of the in-plane field B_w. This is well beyond the critical field necessary to drive this system into the topological regime where Majorana bound states arise, reported to be in the 100-200 mT range [31]. A finite Josephson coupling at 600 mT signifies that InSb T-shaped wires combined with NbTiN leads are suitable elements for a future Majorana braiding circuit.

5.7. CONCLUSION

In summary, we have created a three terminal quantum dot with two superconducting leads and a normal tunnel probe from a single T-shaped InSb nanowire. The coupling to the dot as well as the dot chemical potential was controlled via a global backgate and a local topgate. Flux periodic conductance and current was measured across the dot and identified as resonant Andreev tunneling. The Andreev current can be turned on or off via the quantum dot detuning and bias, as the proximity effect requires both degenerate energies of the two even parity states and a finite probability for even charge occupation. Our results fit well the the theory which allows us to extract coupling strengths of $\Gamma_S \approx$ 10-50 μeV and $\Gamma_N \approx$ 1-3 μeV. The Andreev current persists up to an in-plane magnetic field value 600 mT. Our experiments show that T-shaped InSb nanowires are suitable elements for the Majorana braiding circuit due to their compatibility with finite field superconductivity. Our device also performs well as a finite field SQUIPT.

BIBLIOGRAPHY

[1] R. Fazio and R. Raimondi, "Resonant Andreev Tunneling in Strongly Interacting Quantum Dots," *Phys. Rev. Lett.*, vol. 80, pp. 2913–2916, Mar. 1998.

[2] P. Schwab and R. Raimondi, "Andreev tunneling in quantum dots: A slave-boson approach," *Phys. Rev. B*, vol. 59, pp. 1637–1640, Jan. 1999.

[3] J. C. Cuevas, A. Levy Yeyati, and A. Martín-Rodero, "Kondo effect in normal-superconductor quantum dots," *Phys. Rev. B*, vol. 63, p. 094515, Feb. 2001.

[4] M. Krawiec and K. I. Wysokiński, "Electron transport through a strongly interacting quantum dot coupled to a normal metal and BCS superconductor," *Supercond. Sci. Technol.*, vol. 17, no. 1, p. 103, 2004.

[5] M. G. Pala, M. Governale, and J. König, "Nonequilibrium Josephson and Andreev current through interacting quantum dots," *New J. Phys.*, vol. 9, no. 8, p. 278, 2007.

[6] M. Governale, M. G. Pala, and J. König, "Real-time diagrammatic approach to transport through interacting quantum dots with normal and superconducting leads," *Phys. Rev. B*, vol. 77, p. 134513, Apr. 2008.

[7] H. I. Jørgensen, T. Novotný, K. Grove-Rasmussen, K. Flensberg, and P. E. Lindelof, "Critical Current 0-π Transition in Designed Josephson Quantum Dot Junctions," *Nano Lett.*, vol. 7, pp. 2441–2445, Aug. 2007.

[8] A. Eichler, R. Deblock, M. Weiss, C. Karrasch, V. Meden, C. Schönenberger, and H. Bouchiat, "Tuning the Josephson current in carbon nanotubes with the Kondo effect," *Phys. Rev. B*, vol. 79, p. 161407, Apr. 2009.

[9] J. A. van Dam, Y. V. Nazarov, E. P. A. M. Bakkers, S. De Franceschi, and L. P. Kouwenhoven, "Supercurrent reversal in quantum dots," *Nature*, vol. 442, pp. 667–670, Aug. 2006.

[10] J.-P. Cleuziou, W. Wernsdorfer, V. Bouchiat, T. Ondarçuhu, and M. Monthioux, "Carbon nanotube superconducting quantum interference device," *Nat Nano*, vol. 1, pp. 53–59, Oct. 2006.

[11] M. R. Buitelaar, T. Nussbaumer, and C. Schönenberger, "Quantum Dot in the Kondo Regime Coupled to Superconductors," *Phys. Rev. Lett.*, vol. 89, p. 256801, Dec. 2002.

[12] R. S. Deacon, Y. Tanaka, A. Oiwa, R. Sakano, K. Yoshida, K. Shibata, K. Hirakawa, and S. Tarucha, "Tunneling Spectroscopy of Andreev Energy Levels in a Quantum Dot Coupled to a Superconductor," *Phys. Rev. Lett.*, vol. 104, p. 076805, Feb. 2010.

[13] E. J. H. Lee, X. Jiang, R. Aguado, G. Katsaros, C. M. Lieber, and S. De Franceschi, "Zero-Bias Anomaly in a Nanowire Quantum Dot Coupled to Superconductors," *Phys. Rev. Lett.*, vol. 109, p. 186802, Oct. 2012.

[14] R. S. Deacon, Y. Tanaka, A. Oiwa, R. Sakano, K. Yoshida, K. Shibata, K. Hirakawa, and S. Tarucha, "Kondo-enhanced Andreev transport in single self-assembled InAs quantum dots contacted with normal and superconducting leads," *Phys. Rev. B*, vol. 81, p. 121308, Mar. 2010.

[15] M. R. Gräber, T. Nussbaumer, W. Belzig, and C. Schönenberger, "Quantum dot coupled to a normal and a superconducting lead," *Nanotechnology*, vol. 15, no. 7, p. S479, 2004.

[16] E. J. H. Lee, X. Jiang, M. Houzet, R. Aguado, C. M. Lieber, and S. De Franceschi, "Spin-resolved Andreev levels and parity crossings in hybrid superconductor-semiconductor nanostructures," *Nat Nano*, vol. 9, pp. 79–84, Jan. 2014.

[17] J. Gramich, A. Baumgartner, and C. Schönenberger, "Resonant and Inelastic Andreev Tunneling Observed on a Carbon Nanotube Quantum Dot," *Phys. Rev. Lett.*, vol. 115, p. 216801, Nov. 2015.

[18] J. Gramich, A. Baumgartner, and C. Schönenberger, "Subgap resonant quasiparticle transport in normal-superconductor quantum dot devices," *arXiv:1601.00672 [cond-mat]*, Jan. 2016.

[19] J.-D. Pillet, C. H. L. Quay, P. Morfin, C. Bena, A. L. Yeyati, and P. Joyez, "Andreev bound states in supercurrent-carrying carbon nanotubes revealed," *Nat Phys*, vol. 6, pp. 965–969, Dec. 2010.

[20] W. Chang, V. E. Manucharyan, T. S. Jespersen, J. Nygård, and C. M. Marcus, "Tunneling Spectroscopy of Quasiparticle Bound States in a Spinful Josephson Junction," *Phys. Rev. Lett.*, vol. 110, p. 217005, May 2013.

[21] T. Dirks, T. L. Hughes, S. Lal, B. Uchoa, Y.-F. Chen, C. Chialvo, P. M. Goldbart, and N. Mason, "Transport through Andreev bound states in a graphene quantum dot," *Nat Phys*, vol. 7, pp. 386–390, May 2011.

[22] R. Maurand, T. Meng, E. Bonet, S. Florens, L. Marty, and W. Wernsdorfer, "First-Order $0-\pi$ Quantum Phase Transition in the Kondo Regime of a Superconducting Carbon-Nanotube Quantum Dot," *Phys. Rev. X*, vol. 2, p. 011009, Feb. 2012.

[23] R. Delagrange, D. J. Luitz, R. Weil, A. Kasumov, V. Meden, H. Bouchiat, and R. Deblock, "Manipulating the magnetic state of a carbon nanotube Josephson junction using the superconducting phase," *Phys. Rev. B*, vol. 91, p. 241401, June 2015.

[24] J. J. A. Baselmans, A. F. Morpurgo, B. J. van Wees, and T. M. Klapwijk, "Reversing the direction of the supercurrent in a controllable Josephson junction," *Nature*, vol. 397, pp. 43–45, Jan. 1999.

[25] J. Huang, F. Pierre, T. T. Heikkilä, F. K. Wilhelm, and N. O. Birge, "Observation of a controllable π junction in a 3-terminal Josephson device," *Phys. Rev. B*, vol. 66, p. 020507, July 2002.

[26] F. Giazotto, J. T. Peltonen, M. Meschke, and J. P. Pekola, "Superconducting quantum interference proximity transistor," *Nat Phys*, vol. 6, pp. 254–259, Apr. 2010.

[27] M. Meschke, J. T. Peltonen, J. P. Pekola, and F. Giazotto, "Tunnel spectroscopy of a proximity Josephson junction," *Phys. Rev. B*, vol. 84, p. 214514, Dec. 2011.

[28] A. Ronzani, C. Altimiras, and F. Giazotto, "Highly Sensitive Superconducting Quantum-Interference Proximity Transistor," *Phys. Rev. Applied*, vol. 2, p. 024005, Aug. 2014.

[29] E. Strambini, S. D'Ambrosio, F. Vischi, F. S. Bergeret, Y. V. Nazarov, and F. Giazotto, "The ω-SQUIPT: phase-engineering of Josephson topological materials," *arXiv:1603.00338 [cond-mat]*, Mar. 2016.

[30] S. R. Plissard, I. van Weperen, D. Car, M. A. Verheijen, G. W. G. Immink, J. Kammhuber, L. J. Cornelissen, D. B. Szombati, A. Geresdi, S. M. Frolov, L. P. Kouwenhoven, and E. P. A. M. Bakkers, "Formation and electronic properties of InSb nanocrosses," *Nat Nano*, vol. 8, pp. 859–864, Nov. 2013.

[31] V. Mourik, K. Zuo, S. M. Frolov, S. R. Plissard, E. P. a. M. Bakkers, and L. P. Kouwenhoven, "Signatures of Majorana Fermions in Hybrid Superconductor-Semiconductor Nanowire Devices," *Science*, vol. 336, pp. 1003–1007, May 2012.

6

JOSEPHSON φ_0-JUNCTION IN INSB NANOWIRE QUANTUM DOT

The Josephson effect describes supercurrent flowing through a junction connecting two superconducting leads by a thin barrier[1]. This current is driven by a superconducting phase difference φ between the leads. In the presence of chiral and time reversal symmetry of the Cooper pair tunneling process[2] the current is strictly zero when φ vanishes. Only if these underlying symmetries are broken the supercurrent for $\varphi = 0$ may be finite[3–5]. This corresponds to a ground state of the junction being offset by a phase φ_0, different from 0 or π. Here, we report such Josephson φ_0-junction based on a nanowire quantum dot. We use a quantum interferometer device in order to investigate phase offsets and demonstrate that φ_0 can be controlled by electrostatic gating. Our results may have far reaching implications for superconducting flux and phase defined quantum bits as well as for exploring topological superconductivity in quantum dot systems.

In collaboration with S. Nadj-Perge, D. Car, S. R. Plissard, E. P. A. M. Bakkers and L. P. Kouwenhoven
This chapter has been published Nature Physycs **12** 568 (2016).

6.1. INTRODUCTION

The process of Cooper pair tunneling through a Josephson junction (JJ) is, in general, symmetric with respect to time inversion. This has a profound consequence for the JJ current-phase relation, $I(\varphi)$. In particular it imposes the condition $I(-\varphi) = -I(\varphi)$ which in turn results in $I(\varphi = 0)$ being strictly zero. The $I(\varphi = 0) = 0$ condition is a consequence of the fact that for each process contributing to current flowing in one direction there is an opposite time reversed process, in which spin-up and spin-down electrons are reversed, that exactly cancels this current. However, time inversion is not the only symmetry which can protect the $I(\varphi = 0) = 0$ condition. For example, in JJs based on single domain ferromagnets, time inversion is broken but still the supercurrent is zero for $\varphi = 0$ due to chiral symmetry, i.e. the symmetry between leftward and rightward tunneling. This symmetry assures that the tunneling coefficient describing the electron tunneling from the left lead to right lead is exactly the same as the one describing the tunneling vice versa, from the right lead to the left. The two tunneling processes (leftward and rightward) cancel each other which again results in $I(\varphi = 0)$ being strictly zero. This is even the case for so-called π-junctions[6] in which the current flow is reversed compared to usual JJs but still the underlying symmetries warrant zero current for $\varphi = 0$. In order to create conditions for a non-zero supercurrent to flow at $\varphi = 0$, both symmetries need to be broken[7]. Various ways were proposed theoretically to create φ_0-junctions, including ones based on non-centrosymmetric or multilayer ferromagnets[3, 8] quantum point contacts[4], topological insulators[9, 10], diffusive systems[11, 12], nanowires[13, 14] and quantum dots[5, 15, 16]. Alternatively, an effective built-in phase offset can be obtained by combining 0- and π-junctions in parallel[17, 18]. However no experimental demonstration of φ_0-junction was reported until now.

6.2. BREAKING TIME-REVERSAL AND CHIRAL SYMMETRY IN QUANTUM DOTS

In quantum dots (QDs), breaking of both symmetries can possibly be achieved by the combination of an external magnetic field and spin-orbit interaction (SOI)[5, 15, 16]. Finite Zeeman splitting between spin-up and spin-down electrons breaks the time reversal symmetry. On the other hand, breaking of the chiral symmetry is more subtle. It requires interplay between the SOI and the direction of the magnetic field and it can only occur when multiple orbitals are accessible for electron transport, see Figure 6.1a . When an electron goes in and out from the QD via only one orbital (Figure 6.1a, upper panel) the tunneling coefficient is exactly the same for the forward and the backward tunneling direction. As a result the chiral symmetry is preserved. If, however, the electron changes orbital within the quantum dot (Figure 6.1a, lower panel), an extra phase factor is acquired in the process of orbital mixing. This phase factor, arising from the SOI enabled orbital mixing, depends now on the tunneling direction and it is different for the leftward and rightward tunneling process. As a consequence, the two processes cannot cancel each other and the chiral symmetry is broken. Although we discussed here the case of a single electron tunneling through the QD, the same argument holds for the breaking of the chiral symmetry in the tunneling of Cooper pairs (see section 6.8.1 and Ref[5]). Note that in this scenario both symmetries are explicitly broken by the combin-

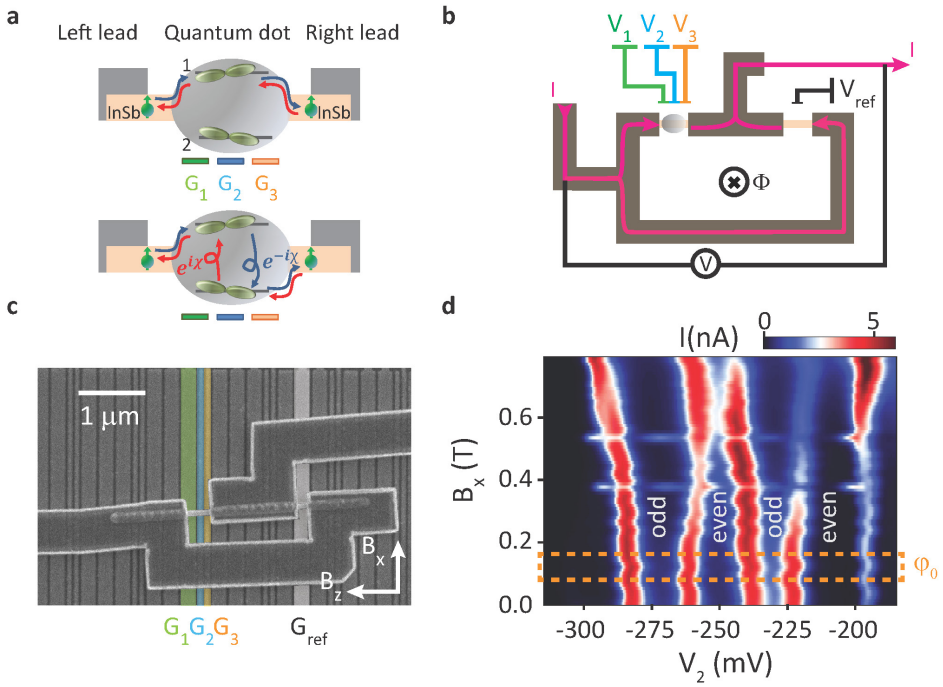

Figure 6.1: **Schematics of the experiment. a,** Schematics showing tunneling of an electron through the QD with two orbitals labelled 1 and 2 which are mixed by the SOI. The blue (red) line describes tunneling of an electron from the left (right) to the right (left) lead. When there is no change in orbital the two processes cancel each other (upper panel). In contrast when the orbital is changed during the tunneling (lower panel), due to interplay between the SOI and a magnetic field $\boldsymbol{B}$, forward and backward tunneling processes do not cancel. In this case an extra phase χ is obtained in the process, which depends on the strength of the SOI and on $\boldsymbol{B_{in-plane}}$. Note that the phase for forward and backward tunneling is different. **b,** Device schematic showing a dc-SQUID measured in a four terminal geometry. Voltages V_1, V_2, V_3, and V_{ref} are applied on underlying gates to control the conductance of the JJs. **c,** Scanning electron microscopy (SEM) image of the actual device. Gates G_1, G_2 and G_3 are used to define a quantum dot in the long JJ while G_{ref} tunes the current through the reference JJ. Orientation of the in-plane magnetic fields B_X and B_Z are marked. B_Y is used for tuning flux Φ through the SQUID. **d,** Current as a function of V_2 and B_X showing QD evolution of the Coulomb peak spacing in the field which gives g-factor $g_x \approx 51$. From similar data taken for B_Z we obtain $g_z \approx 44$ and spin-orbit gap $\Delta_{SO} \approx 170$ μeV. The extracted Δ_{SO} corresponds to $l_{SO} \approx 350$ nm and $E_{SO} \approx 20$ μeV [19]. Measurements are performed in the voltage bias regime, $V_{bias} = 500$ μV. The dashed rectangle indicates the range of B_X for which the φ_0-junction is observed.

ation of magnetic field and SOI[5].

6.3. GATE DEFINED QUANTUM DOT EMBEDDED IN A SQUID

The device geometry is shown in Figure 6.1b and Figure 6.1c. A single nanowire, made of Indium Antimonide (InSb), is contacted using Niobium Titanium Nitride (NbTiN) as a superconductor to make two JJs forming a quantum interference device (SQUID). We choose InSb nanowires due to their large spin-orbit coupling and g-factors both of which are important for breaking time inversion and chiral symmetry at relatively low magnetic fields [19],[20]. Electrostatic gates below the wire are used to create a tunable quantum dot in the longer JJ and control the switching supercurrent of the shorter reference JJ [19] (Figure 6.1b).). Our coordinate system is defined such that the in-plane magnetic field coincides with the x- and z-axis, while the flux through the SQUID is applied along the y direction (Figure 6.1c). Standard quantum dot characterization, while the reference junction is pinched off, is used to determine the values of the charging (E_C) and orbital (E_{orb}) energies as well as g-factors. Depending on the confinement details and QD occupation number we find $E_C = 2-3$ meV, $E_{orb} = 0.3-1.5$ meV and $g = 40-50$ (Figure 6.1d). We identify small peaks around zero bias as an onset of superconductivity and estimate the induced superconducting gap in the QD to be $\Delta^* = 20-50$ μeV (see section 6.8.2).

First we measure the SQUID response in current bias for zero in-plane magnetic field (Figure 6.2). Switching currents for the reference and quantum dot JJ, $I_{c_{ref}}$ and $I_{c_{QD}}$, satisfy $I_{c_{ref}} >> I_{c_{QD}}$, ensuring that the phase drop is mainly across the QD. The measured voltage as a function of flux and bias current I_{bias} shows oscillations with a period of $B_Y = 1.2$ mT (Figure 6.2a) corresponding to an effective area of 1.8 μm^2, which is consistent with the SQUID geometry and the penetration depth of NbTiN ($\lambda \approx 170$ nm). Both junctions are in the phase diffusive regime such that no hysteresis is observed (Figure 6.2b). This allows probing of the phase response by applying a finite $I_{bias} = 100-500$ pA close to $I_{c_{ref}}$ and monitoring the voltage drop across the SQUID, V, as a function of gate voltage V_2 and flux Φ, see Figure 6.2b as well as section 6.8.2.

6.4. ZERO-FIELD π-JUNCTION

In this QD regime, the phase of the SQUID pattern depends crucially on the dot occupation number (Figure 6.2b). For example, for $V_2 \approx -247$ mV, the measured voltage oscillates as a function of Φ with a particular phase (purple colored line in Figure 6.2b). When V_2 is increased to around -240 mV the oscillations disappear and the overall voltage drops as the charge degeneracy point is reached. By increasing V_2 further, the oscillations recover with an extra π phase corresponding to the sign reversal of the supercurrent in a QD [21] (light blue line in Figure 6.2b). The change of phase by π is repeated for several consecutive charge states.

The change in phase measured for zero in-plane field occurs due to the change in the electron parity of the ground state. In a simple physical picture, for odd QD occupancy, the order of electrons forming a Cooper pair is reversed in the process of co-tunneling through a single quantum dot orbital. This results in the sign reversal of the supercurrent and the observed π shift, as previously reported in Ref.[21]. Note, however, that even if the phase of the ground state is changed, $I(\varphi = 0)$ remains zero which is anticipated

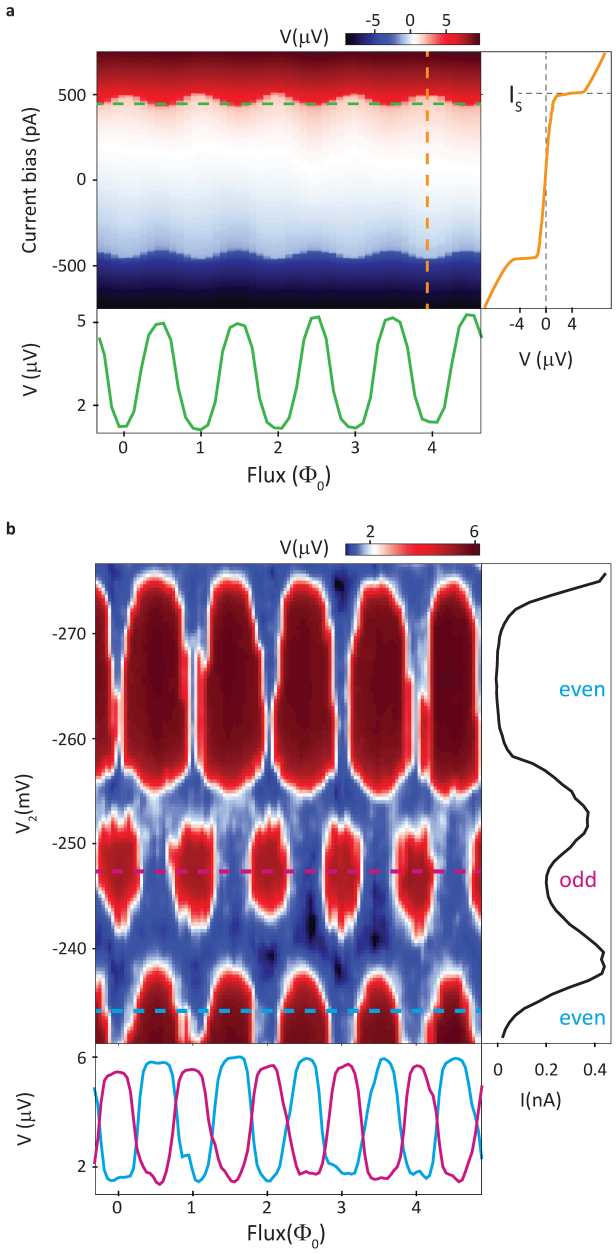

Figure 6.2: **Nanowire SQUID characterization. a,** Voltage across the SQUID, V, as a function of bias current I_{bias} and flux Φ through the SQUID. The right panel shows V vs I_{bias} measured at $\Phi = 4\Phi_0$ (cut along the orange dashed line). The switching current I_S separating low and high resistance regions is indicated. The lower panel shows voltage vs Φ for $I_{bias} = 450$ pA (cut across the green dashed line). **b,** V as a function of V_2 and Φ for $I_{bias} = 190$ pA. The phase of the SQUID oscillations is alternating between 0 and π depending on the electron parity of the ground state of the QD. The right panel shows Coulomb peaks in the voltage bias regime. The bottom panel shows V vs. flux cuts at $I_{bias} = 195$ pA for $V_2 = -247$ mV (purple) and $V_2 = -233$ mV (light blue).

since time reversal symmetry is preserved.

6.5. FINITE-FIELD φ_0-JUNCTION

Finite magnetic fields can substantially modify this simple picture in two ways. First, the QD levels split by Zeeman energy which results in different co-tunneling rates for spin-up and spin-down electrons and therefore breaks time reversal symmetry. Second, the spin split levels belonging to different orbitals move closer in energy which enables more than one orbital to contribute to the co-tunneling process. This in turn, combined with strong SOI induced orbital mixing and asymmetry in the barriers, results in the breaking of chiral symmetry (see section6.8.1). Under these conditions one can expect an anomalous current and shifts in the phase by an arbitrary φ_0 (See section 6.8.3 for details on the relation between the anomalous current and φ_0).

For finite in-plane magnetic fields we find regimes in which the shifts of the SQUID pattern are different from 0 or π. Instead, the shifts take non-universal values depending on the specific QD configuration and magnetic field direction and strength (Figure 6.3). Figure 6.3a and Figure 6.3b show an example taken close to the QD charge degeneracy point. The shift in SQUID response between the two Coulomb blockade regions is approximately 0.7π. This value is considerably different from the value π observed for the same QD regime when the in-plane field is zero (compare the data in Figure 6.3a and Figure 6.3b with the data in Figure 6.2). Note also that while effects related to finite temperature have impact on the critical current values and in general on the values and visibility of the SQUID response they do not contribute to any phase offset (see section 6.8.4).

The measured gate tunable phase shift directly implies a finite φ_0, different from 0 or π, for at least one of the Coulomb blockade regions. Importantly, this shift cannot be explained by simple higher harmonic terms in the JJ current-phase relation which can occur in various semiconductor based junctions[22–25]. Even if such terms were present, as long as $I(-\varphi) = -I(\varphi)$, the SQUID response would have to be symmetric around the points corresponding to integer values of the threaded flux. Since this is clearly not the case in the data shown in Figure 6.3 we conclude that the $I(-\varphi) = -I(\varphi)$ condition is violated. Note that both junctions in the SQUID are nanowire based so phase shifts can occur in the reference junction as well. For this reason shifts in the SQUID pattern should be interpreted as relative offsets in φ_0 of the QD based junction.

Typically, the phase of the SQUID oscillation is constant within the Coulomb blockade region and changes only at the charge degeneracy points. Depending on the exact gate settings the phase change appears either as a discrete jump or a continuous transition. In the investigated regimes, we measured jumps when the QD is strongly confined (as in Figure 6.3**a** and 6.3**b**). For a more open QD we observe a continuous change in the phase of the SQUID response as we tune the gate G2 across the charge degeneracy point (Figure 6.3**c** and 6.3**d**). This behavior is not fully understood but we note that transport for a strongly confined QD is dominated by the resonant tunneling process at the Coulomb peak and therefore can be very different compared to the transport deep in the blockaded regime. This effect is not pronounced for open QD in which higher order tunneling processes are relevant. In the regimes where the SQUID oscillations can be detected along the whole charge transition we observe a continuously changing phase.

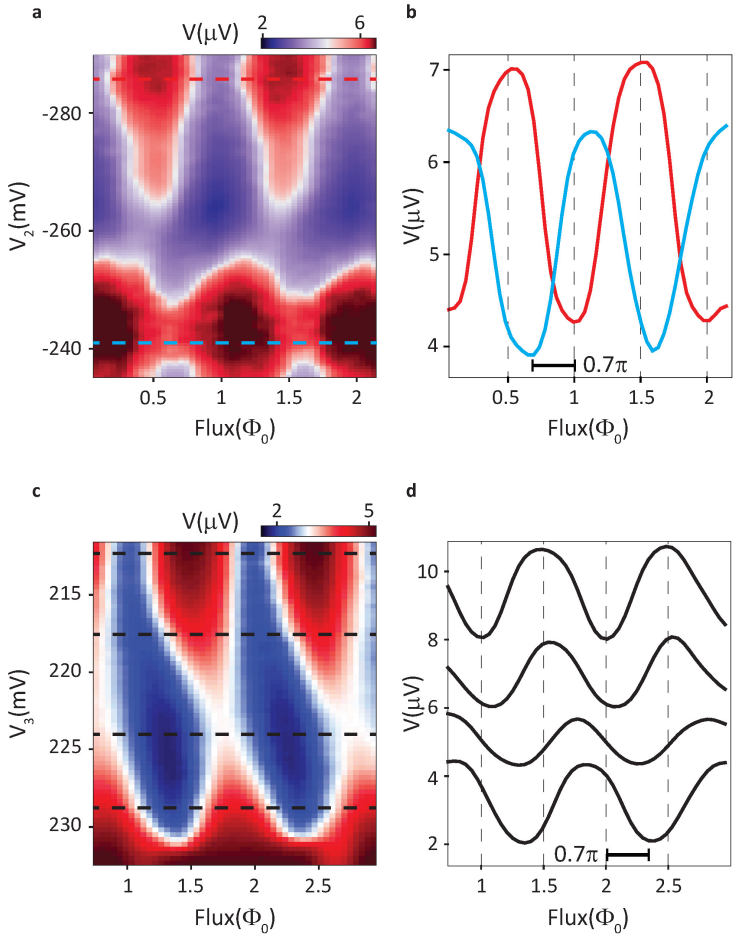

Figure 6.3: **Observation of a continuous phase change in the Josephson φ_0-junction. a** and **c:** V as a function of V_2 (V_3 in panel c) and Flux at fixed current bias (I_{bias} = 470 pA, $\boldsymbol{B_{in-plane}}$= 120 mT and $\theta = -135°$ for panel a; I_{bias} = 240 pA, $\boldsymbol{B_{in-plane}}$= 75 mT and $\theta = -35°$ for panel c). Here θ is the angle between the direction of the in-plane magnetic field and the nanowire axis. In contrast to the data taken at zero in-plane magnetic field, the phase shift of the voltage oscillations in flux is tunable with gate voltage V_2 (V_3 in panel c). **b** and **d,** V vs flux for values of V_2 (V_3 in panel d) marked by dashed lines on panels a and c showing phase shifts. In panel b the black curve is taken at $V_2 = -285$ mV and I_{bias} = 460 pA and the orange at $V_2 = -240$ mV and I_{bias} = 470 pA. The relative offset from the two curves is $0.35 \pm 0.1\Phi_0$. In panel d the curves are cuts from panel c taken at V_3 values of 213 mV; 218 mV; 225 mV; 229 mV. The corresponding offsets in phase compared to the top curve are $(0.1 \pm 0.05)\ \Phi_0$, $(0.3 \pm 0.05)\ \Phi_0$ and $(0.4 \pm 0.05)\ \Phi_0$. Note that in the QD regime shown in panel c and d we used gate G_3 for tuning.

Importantly in all regimes fields of $B_{in-plane} \approx 50-150$ mT are required to see a noticeable shift in the SQUID response (see additional data in section6.8). These fields are still around two to four times smaller compared to the critical fields of $B_{in-plane} = 200-300$ mT at which the SQUID response vanishes.

6.6. MAGNETIC FIELD ANGLE-DEPENDENCE OF THE φ_0-JUNCTION

Finally, we examine the magnetic anisotropy dependence of the SQUID pattern, in order to further study the microscopic origin of the φ_0-junction. The data showing phase shifts between neighboring charge states for various in-plane magnetic field angles is presented in Figure 6.4. Consistently, for many different QD regimes, we observe that the maximum shift of the SQUID pattern is most pronounced when an in-plane field is applied orthogonal to the nanowire. Previous quantum dot experiments have identified this field orientation with the preferential spin-orbit direction $\boldsymbol{B_{SO}}$ for quantum dots. These measurements are consistent with SOI enabled orbital mixing which predicts maximal phase φ_0 for $\boldsymbol{B_{in-plane}} || \boldsymbol{B_{SO}}$ 5,12,13. Note that other known mechanisms which could in principle lead to additional phase shifts, such as flux penetrating the JJ area, are not consistent with the observed data (see section6.8.5 and 6.8.6 for a more detailed discussion).

6.7. CONCLUSION

In summary, we demonstrated a gate tunable Josephson φ_0-junction. Results presented here imply that the breaking of the underlying symmetries can be achieved in superconductor-quantum dot structures while maintaining coherent transport of Cooper pairs. In this context, our experiment is directly related to the efforts of studying triplet superconductivity and superconducting spintronics[26] as well as in achieving topological superconducting phase in quantum dots coupled to an s-wave superconductor[16][27–32]. Aside from that, a gate tunable phase offset may open novel possibilities for the realization of electrically controlled flux and phase based quantum bits[33], superconducting computer memory components[34], as well as superconducting "phase" batteries and rectifiers[4, 35]. Finally, we note that that other one-dimensional materials, such as carbon nanotubes where spin-orbit is strong due the curvature of the tube, may be explored in the context of φ_0-junctions[36].

6.7.1. METHODS

DEVICE FABRICATION

The Indium Antimonide (InSb) wires used in the experiments were grown using MOVPE process[37]. The wires were transferred on a SiO chip with local electrostatic gates made of Ti/Au of thickness 5nm/10nm predefined via electron beam lithography. The superconducting contacts were subsequently designed and patterned over the wires and prior to deposition the wires were etched in Ar+ plasma for 120 seconds to remove native surface oxides. NbTiN was sputtered in similar conditions as in Ref. [38].

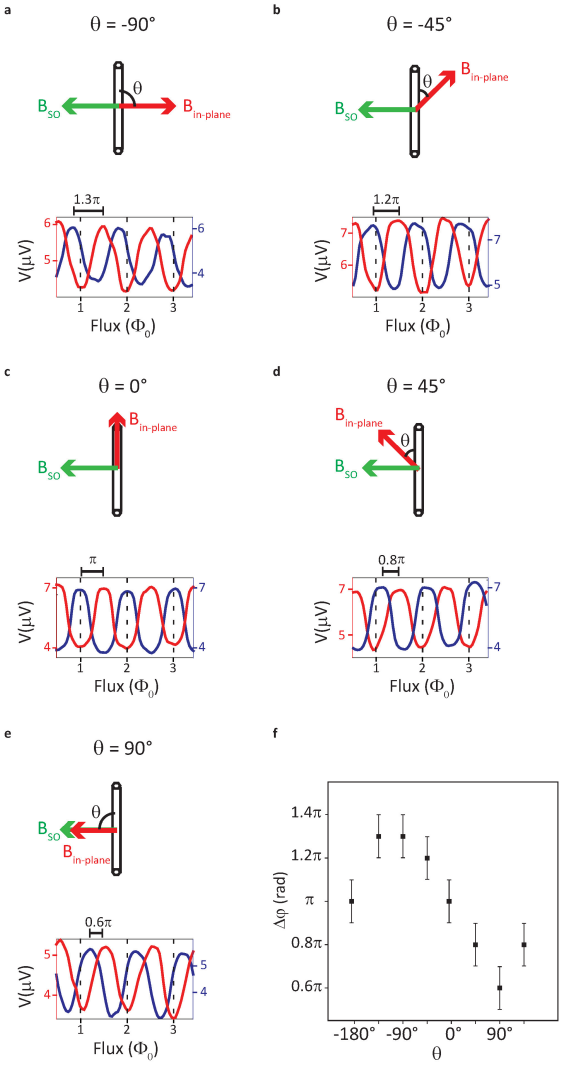

Figure 6.4: **Anisotropy of the SQUID phase shift for various angles of $B_{in-plane}$. a-e,** Voltage vs. flux for different orientations of $B_{in-plane}$ = 120 mT. Red and blue curves in each panel are taken at two neighboring charge occupations as in Figure 6.3**a** and the corresponding relative phase shift between is marked above each panel. The maximum shift from π was obtained when the field is perpendicular to the wire as expected from the SOI enabled orbital mixing (see also section6.8.7).**f,** Phase offset as a function of angle θ between the nanowire and $B_{in-plane}$.

MEASUREMENTS

All measurements are performed in a He3/He4 dilution refrigerator equipped with adequate high-frequency electronic filtering at a base temperature of T = 20 mK. The magnetic fields, both in-plane and for flux bias, are applied via a 3-axis vector magnetic.

To avoid hysteresis in magnetic field while performing flux biased measurements, we first step the magnetic field in the y-direction to adjust the flux to the desired value. We then set the gate and measure the voltage over our device for the gate values corresponding to different charge states of the quantum dot. When this is done we step the flux forward and repeat the voltage measurements for the same gate values and so on. Hence the flux is always monotonically increased for a data set related to a particular in-plane field value and we do not suffer from hysteresis from the vector magnet. Our measurements were reproducible and finite offsets in the SQUID response corresponding to φ_0-junction were observed in three separate cooldowns of the device.

6.8. SUPPLEMENTARY INFORMATION

6.8.1. BREAKING OF THE CHIRAL SYMMETRY IN QUANTUM DOTS

In one-dimensional systems in which the electron momentum is well defined, the interplay between the spin-orbit interaction (SOI) and the Zeeman splitting can create a difference between the dispersion of electrons moving forward and backward. This in turn can lead to the breaking of the chiral symmetry and, in the case of superconducting transport, to Josephson φ_0-junctions [4, 10, 13]. In quantum dots (QDs) there is no well-defined momentum since the QD states are localized. Nevertheless, the combination of the SOI and the external magnetic field still creates similar conditions for breaking of the chiral symmetry as shown in Refereneces [5, 15, 16] and discussed below.

Let us consider a process describing a Cooper pair tunnelling from the left to the right lead (forward tunnelling) at zero phase difference. Without SOI electrons forming the Cooper pair tunnel through the QD via a single orbital level, for example the first electron tunnels via level 1 and the second via level 2. The corresponding tunnelling coefficient (matrix element) for this process is given by $(t_{L1}t_{R1})(t_{L2}t_{R2})$. Here the t_{L1} and t_{L2} (t_{R1} and t_{R2}) are the hybridization amplitudes between QD levels 1 and 2 with the left (right) lead. The terms in brackets correspond to tunnelling coefficients for individual electrons. Assuming that the hybridization amplitudes are real, the matrix element describing tunnelling from the right to the left (backward tunnelling) is exactly the same. Since the backward tunnelling contributes to the current flow in the opposite direction, the net resulting current vanishes. Therefore, the tunnelling via single orbitals can not add to $I(\varphi = 0)$. The lowest order process which contributes to $I(\varphi = 0)$ is the one in which one electron tunnels through the dot directly via a single orbital, while the other electron changes the orbital during the tunnelling process. Finite SOI enables such orbital change.

In the simplest case when two quantum dot levels contribute to Cooper pair transport and the magnetic field is orientated along the effective spin-orbit axis the Hamiltonian of the dot can be written as

$$H_{QD} = (\mu\tau_0 + E_{orb}\tau_Z)\sigma_0 + B\tau_0\sigma_Z + \alpha\tau_Y\sigma_Z \tag{6.1}$$

Here μ is the chemical potential, E_{orb} is the orbital energy, α parametrizes the strength of the SOI and B the Zeeman splitting, $\tau_{X,Y,Z}(\sigma_{X,Y,Z})$ are Pauli matrices acting in orbital (spin) space ($\tau_0(\sigma_0)$ are identity matrices). Usually the terms describing the Zeeman splitting and the SOI are smaller in comparison to the first term in the Hamiltonian. In the presence of SOI the eigenstates of the QD are mixtures of the two orbital states. The hybridization between QD eigenstates and the left (right) lead becomes $t_{L(R)1'} = t_{L(R)1}\cos\varepsilon + t_{L(R)2}\, i\sin\varepsilon$ and $t_{L(R)2'} = t_{L(R)2}\cos\varepsilon - t_{L(R)1}\, i\sin\varepsilon$ for spin-up electrons (with $\sin\varepsilon = \alpha/E_{orb}$). For the spin down electrons + and - signs should be inverted.

Importantly, due to orbital mixing, the coefficients describing tunneling events become complex numbers implying that electrons crossing the junction gain a finite phase. This phase is opposite for the electrons tunneling in the other direction. Therefore the forward and backward tunneling coefficients are not exactly the same (the imaginary part is different) and the two tunneling processes do not cancel each other. If Cooper pairs also acquire a finite phase during the tunneling process, $I(\varphi = 0)$ becomes finite. However, if the magnetic field is zero, since spin-up and spin-down electrons obtain the opposite phases in the tunneling process, Cooper pairs do not gain phase even when SOI is present. For finite magnetic fields the tunneling probabilities for the tunneling of spin-up and spin-down electrons via different orbitals are no longer exactly the same. Only in this case can Cooper pairs obtain a finite phase.

Finally we stress that the complex tunnel coupling between superconductors always leads to finite $I(\varphi = 0)$. Interestingly, this follows even from Feynman's simplified description of the Josephson effect[39]. If we assume that the wave-functions describing the two superconductors are $\psi_L = |\psi_L|e^{i\varphi_L}$ and $\psi_R = |\psi_R|e^{i\varphi_R}$, the time dependent Hamiltonian describing the superconductors on the two side of the junction can be written as

$$i\hbar\frac{\partial}{\partial t}\psi_L = \mu_L\psi_L + T\psi_R \tag{6.2a}$$

$$i\hbar\frac{\partial}{\partial t}\psi_R = T^*\psi_R + \mu_L\psi_R \tag{6.2b}$$

Here μ_L and μ_R are the chemical potentials in the two superconductors and T is the tunnel coupling. Solving this set of equations for current directly gives

$$I \approx |\psi_L||\psi_R|\left(Re(T)\sin\varphi_L - \varphi_R + Im(T)\cos\varphi_L - \varphi_R\right) \tag{6.3}$$

When T is real current is proportional to $\sin\varphi$, with $\varphi = \varphi_L - \varphi_R$. However if the imaginary part is non -zero, the term $\cos\varphi$ also contributes to the current and gives rise to the finite $I(\varphi = 0)$.

6.8.2. CHARACTERIZATION OF THE QUANTUM DOT JUNCTION AND THE NANOWIRE BASED SQUID

In order to characterize the QD Josephson junction, we performed voltage and current bias measurements while the reference junction was pinched off. Depending on the exact gate configuration, the measured QD resistance varies between 40-600 kΩ and the switching currents are in the range 40-300 pA. In all measurements the sub-gap resistance is finite since the Josephson energy of the QD junction $E_J = \Phi_0 I_C/2\pi \approx 0.5-3\mu$eV is

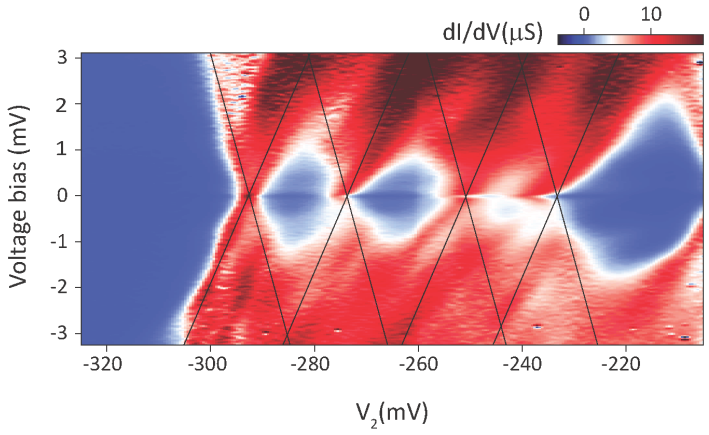

Figure 6.5: **Coulomb blockade diamonds**Gate configuration is the same as in Fig.6.1 and Fig.6.2 ($V_1 = 350$mV; $V_3 = 110$mV)

comparable to $k_B T \approx 5\mu$eV. The induced gap in the QD junction is of the order of 20-50 μeV (see Figure 6.6 (b), (d)).

When the reference junction is open we observe standard SQUID oscillations. In this regime it is even easier to resolve small supercurrents of the QD junction by simply estimating the amplitude of the flux dependent voltage oscillations. Note that the data presented in the main text is taken with the SQUID tuned to the overdamped regime. However, at low magnetic fields, the SQUID is usually underdamped (Figure 6.7). Due to hysteresis effects, in this case, phase offsets are difficult to track in the voltage vs flux measurements when the current bias is fixed. For this reason, before each measurement we made sure that SQUID is in the overdamped regime by tuning the switching current of the reference junction via G_{ref}.

6.8.3. ANOMALOUS CURRENT AND DIRECTION DEPENDENT CRITICAL CURRENT IN φ_0-JUNCTIONS

The subject of φ_0-junctions has been theoretically extensively studied in the past. They have been predicted to arise in many different systems besides quantum dots 1,5,16, such as conventional superconductors with spin-orbit coupling 17–19, with triplet correlations 20–22, superconductors in contact with topological materials 23,24 and also hybrid systems with nonconventional superconductors 25–27.

The current-phase relation (CPR) for conventional Josephson junctions states that the switching current varies with the sine of the phase difference across the junction: $I_S(\varphi) = I_0 \sin\varphi$, where the junction's critical current $I_C = I_0$. This CPR can be generalized by adding a cosine term:

$$I_S(\varphi) = I_0 \sin\varphi + I_{anomalous} \cos\varphi \equiv I_C \sin(\varphi + \varphi_0), \tag{6.4}$$

where the critical current is now expressed as $I_C = \sqrt{I_0^2 + I_{anomalous}^2}$. For conven-

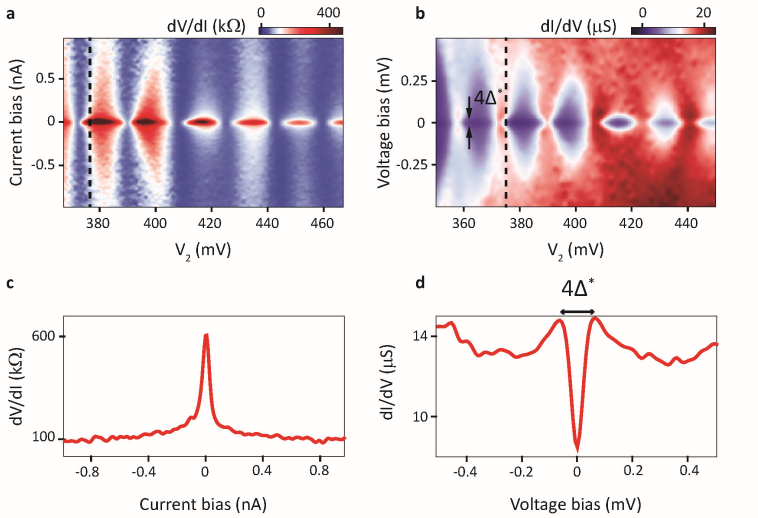

Figure 6.6: **Superconducting gap in Coulomb blockade** Current biased **(a)** and the corresponding voltage biased **(b)** regime ($V_1 = 350$ mV; $V_3 = 110$ mV) vs V_2. In this regime QD has 30 electrons more compared to Fig. 6.5. **c,d,** Linecuts for current (voltage) bias for the fixed gate voltage showing resistance (conductance) of the QD junction. The sudden increase in resistance corresponds to the suppression of the density of the states inside of the superconducting gap $\Delta^\star \approx 25\mu$eV in this regime. Note that the coupling between the QD and the leads is larger compared to $\Delta^\star$.

tional 0-junctions ($\varphi_0 = 0$) and π-junctions ($\varphi_0 = \pi, I_S = -|I_0|\sin(\varphi) \equiv I_0 \sin(\varphi + \pi)$), the anomalous term vanishes and there is no current flowing when the phase difference $\varphi_0 = 0$. This can be seen in Figure 6.8**a** where we plot the switching current as a function of the phase difference φ for a 0-junction and a π-junction.

It follows that a $\varphi_0 = 0$ term different from 0 or π directly implies the existence of a finite anomalous current. In Figure 6.8**b** we show the anomalous current for a junction with $\varphi_0 = 0.15\pi$. This is a shifted sine curve, hence $I_{C+} \equiv \max_\varphi I_S = I_{C-} \equiv |\min_\varphi I_S|$, meaning that the critical current is independent of the bias direction. In order to be able to measure a different critical current when the bias is reversed, i.e. to satisfy the condition $I_{C+} \neq I_{C-}$, the CPR needs to contain higher order terms, e.g. as in the experiment by Sickinger et al. 15. In Figure 6.8**c** we plot the switching current for a junction with $I_S(\varphi) = \sin(\varphi + 0.35\pi) - 0.5\sin 2\varphi$ and indeed obtain two different critical currents as shown on the plot.

6.8.4. SHIFTS OF THE SQUID PHASE SHIFT PATTERN

In order to understand the origin of the shifts in our SQUID pattern, we have performed simulations of the critical current of a dc-SQUID consisting of two Josephson junctions with current-phase relationships (CPR) $I_{S_{1,2}} = CPR_{1,2}(\varphi_{1,2})$, where I_{S_1} (I_{S_2}) is the switching current of junction 1 (junction 2) and φ_1 (φ_2) is the superconducting phase difference across junction 1 (junction 2).

Assuming negligible SQUID inductance, the phase difference across the junctions

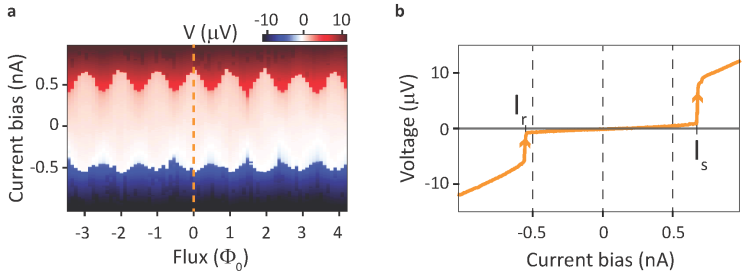

Figure 6.7: **SQUID in the underdamped regime at zero in-plane field. a,**Voltage as a function of flux and the current bias showing hysteresis effects in the switching and retrapping current. **b,** Line cut along the dashed line in (a) showing a difference of around 200 pA between switching and retrapping currents. Gate setting are: $V_1 = 100$ mV; $V_2 = 25$mV; $V_3 = 335$ mV; $V_{ref} = 420$ mV.

are related to each other by the equation $\varphi_2 = \varphi_1 - 2\pi\frac{\Phi_{ext}}{\Phi_0}$, where Φ_{ext} is the external flux applied through the SQUID. The critical current of the SQUID is the calculated using the equation

$$I_{C,SQUID} = \max_{\varphi}|\mathrm{CPR}_1 + \mathrm{CPR}_2(\varphi - 2\pi\frac{\Phi_{ext}}{\Phi_0} + 2\pi n)|.$$

In Figure 6.9**a** we plot the critical current of the SQUID assuming $I_{S_{1,2}}) = I_{C_{1,2}}\sin\varphi_{1,2}$ for several values of the ratio $\frac{I_{C_1}}{I_{C_2}}$. We observe that although the shape of the $I_{C,SQUID}$ vs. flux curve varies, the points in flux of the maxima and minima are fixed. In Figure 6.9**b** we plot the same curves but now CPR_1 is a periodic sawtooth, i.e. $I_{S_1} = I_{C_1}(\varphi/\pi - 1)$. Still the minima and the maxima of the critical current remain fixed, independent of the ratio $\frac{I_{C_1}}{I_{C_2}}$.

In Figure 6.9**c** we assume $I_{S_1} = 0.1I_{C_2}\sin(\varphi_1 - \varphi_0)$ and vary the value of φ_0. In contrast to the previous two cases, the maxima and minima of the critical current now shift by $\Phi_{ext} = \varphi_0/2\pi$. Considering that the maximum (minimum) of $I_{C,SQUID}$ corresponds to a minimum (maximum) in the measured voltage V over the SQUID, such $I_{C,SQUID}$ behaviour is qualitatively similar to the measured voltage pattern shown in Figure 6.3**b, c** and Figure 6.4 of the main text as well as Figure 6.11**b** of this supplementary. In our simulations the only way we could induce additional phase shifts in the SQUID pattern is to offset one of the junctions by φ_0. Therefore these are consistent with our interpretation that the origin of the shift in our measured SQUID patterns is indeed a consequence of the shift by φ_0 in CPR of the nanowire Josephson junction.

To be certain that the magnitude of the critical currents does not influence the phase of the SQUID oscillations, we repeated scans with the same gate voltages over the quantum dot V_1, V_2, V_3, and varied I_{Cref} by changing the gate voltage of the reference junction V_{ref} over a wide range and found no change of the induced shift, even when the SQUID is underdamped regime.

This is understandable since the phase difference between the junctions in a SQUID geometry is fixed by the external flux. So while the relative ratio between the critical currents (which is not exactly known due to phase diffusion) have impact on the critical current values and in general on the visibility of the SQUID response they do not change

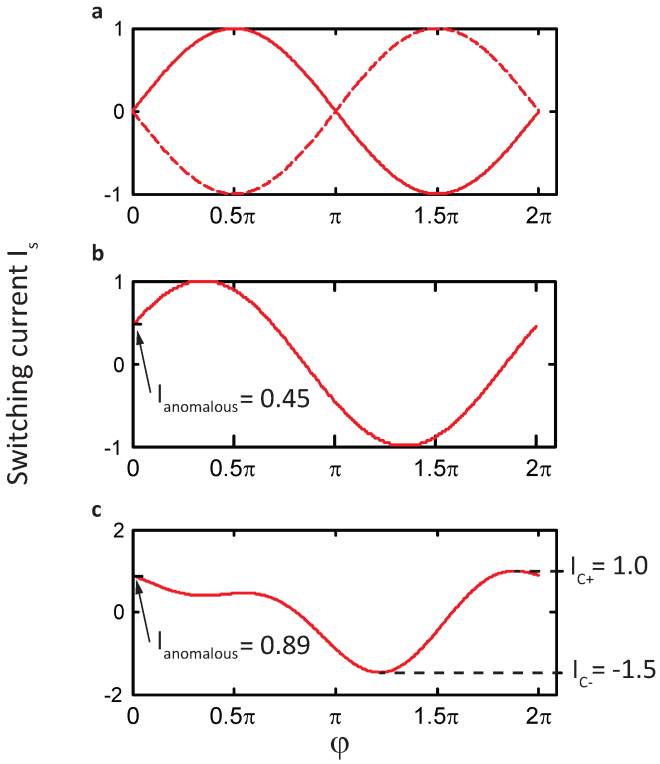

Figure 6.8: **Switching current for junctions with various CPR normalized to I_0. a,** $I_S(\varphi) = \sin\varphi$ (continuous line) and $I_S(\varphi) = \sin(\varphi+\pi)$ (dashed line). **b,** $I_S(\varphi) = \sin(\varphi+0.15\pi)$, $I_{anomalous} \equiv I_S(0)$ is shown. **c,** $I_S(\varphi) = \sin(\varphi+0.35\pi) - 0.5\sin 2\varphi$, anomalous current $I_{anomalous}$ and direction dependent critical current are shown.

the phase offset. This fact is illustrated in the experiment of Spathis et al. 8 , where the authors measured the nanowire SQUID response in the wide range of temperatures and found no shifts in the pattern.

6.8.5. ESTABLISHING THE ORIGIN OF THE SHIFT IN THE SQUID PATTERN

Our main experimental observations can be summarized as follows: (1) the observed shift in the SQUID pattern occurs for a finite in-plane magnetic field which exact value depends on the QD configuration; (2) the shift in pattern occurs mainly for gate values at which the QD electron occupation number changes; (3) the shift is the largest when the field is orthogonal to the nanowire and almost non-existing when the field is oriented along the nanowire.

These observations are qualitatively in agreement with SOI induced orbital mixing as the origin of the φ_0-junction. Based on (1) and (2) it is evident that QD orbital levels play a crucial role in the superconducting transport which is also in agreement with previous experiments on quantum dots [21, 40, 41]. Also, the observed anisotropy is consistent with reported SOI direction in QDs [42]. In the following we discuss other effects which

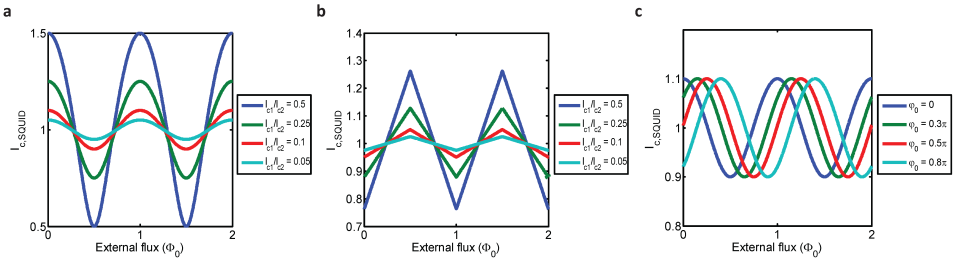

Figure 6.9: **Critical current simulations of a dc-SQUID. a,** Simulation including two sinusoidal junctions with varying critical current ratios. **b,** Simulation including a junction 1 with a sawtooth-like CPR and junction 2 with a sinusoidal CPR, with varying critical current ratios. **c,** Simulation including two sinusoidal junctions where the CPR of junction 1 is shifted by a phase φ_0. The ratio $\frac{I_{C_1}}{I_{C_2}} = 0.1$.

may also contribute to the observed shifts in the SQUID pattern.

a) Gate induced changes in the effective SQUID area. Gating off a part of the wire changes the effective SQUID area which may result in additional shifts of the interference pattern. This effect is rather small in our devices. The maximal change in the area, and therefore the phase offset, would be at most few percent estimated by comparing the gated nanowire area 100nm × 100nm with the total area of the SQUID. Even if assumed that the magnetic field is enhanced in the vicinity of the nanowire junction, due to complicated field profile caused by the nearby superconductor, the change in area has to be extremely large to account for the observed shift. Also, for substantial changes in the area, the flux periodicity of the SQUID response has to change substantially. These changes were not observed in the experiment which shows periodicity of 1.2mT being independent of the gate parameters. We also note that we didn't observe any discontinuous jumps in the interference pattern while sweeping the magnetic field which rules out phase shifts due to accidental events of flux trapping in the junction.

b) Phase offsets due to flux in the quantum dot. The observed shifts in the SQUID pattern were obtained in in-plane field values of 50-100 mT. Assuming the quantum dot area to be 60nm × 60nm (corresponding to $E_{orb} = 1.5$ meV), the total flux through the corresponding area would be of the order of $0.1 - 0.2\Phi_0$. Based on this estimate, even if the flux through the QD would fully add to the φ_0 offset, the resulting shift would be too small to explain the experimental data. Note that we verified that there is no significant modification of the field profile in the vicinity of the quantum dot by measuring the values of the g-factors.

c) Additional orbital effects. As discussed in Ref. [5,6], when the tunneling coefficients (matrix elements) describing the hybridization between the QD levels and the left (right) lead are complex numbers and contribute to additional phase factors, at finite magnetic field an anomalous Josephson current may occur. Orbital effects can also contribute to this complex phase instead of SOI. While this is in principle a possible scenario it is not consistent with the experimental data as one would not expect any magnetic field anisotropy in this case. Another possible scenario is that orbital effects alone can result in an anomalous current. As pointed out in Refs. [13,14] orbital effects alone may

have a significant influence on superconducting transport through the nanowire without any QD. Although these effects may indeed contribute, they are to the large degree linear in magnetic field strength in contrast to the experimental data. For this reason, we can rule out these effects as the main contribution of the observed shifts.

6.8.6. ESTIMATION OF THE ANOMALOUS CURRENT

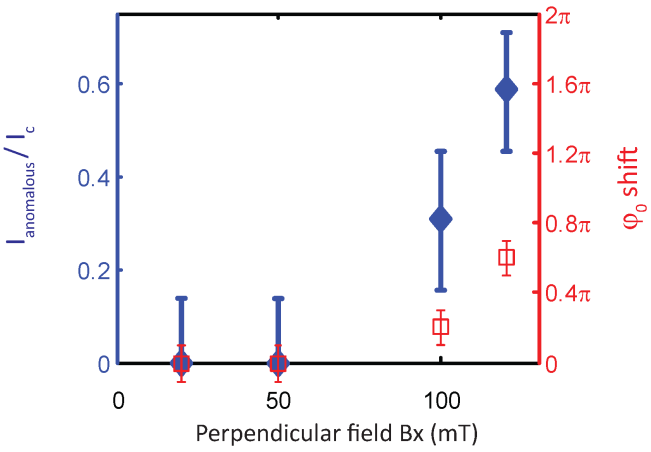

Figure 6.10: **Anomalous current as a function of magnetic field.** Estimates and measured phase shifts of $I_{anomalous}$ as a function of field magnitude for the regime shown in Figure 6.13 (perpendicular in-plane field).

Using the data from the regime presented in Figure 6.13**a** and the relation $I_{anomalous} = I_C \sin\varphi_0$, we estimate the minimum anomalous current through our quantum dot.

The procedure we use the estimate the anomalous current goes as following. We assume that the critical current I_C is constant along charge state transitions for a fixed $\mathbf{B_{in-plane}}$. Within a charge transition where we measure a relative change in phase of φ_0, we choose the larger value of the possible magnitude of the anomalous current, i.e. $\max(|I_C \sin\varphi|, |I_C \sin(\varphi+\varphi_0)|)$. However, since the phase difference φ across the quantum dot is unknown, we minimize this function over all possible values of φ. Thus we obtain our minimum estimate of the magnitude of the anomalous current $|I_{min,anomalous}|$ as

$$|I_{min,anomalous}| = \min_{\varphi\in[0,\pi]} \left\{\max(|I_C \sin\varphi|, |I_C \sin(\varphi+\varphi_0)|)\right\}.$$

$|I_{min,anomalous}|$ vanishes for $\varphi_0 = 0, \pi$ as expected for zero and π-junctions, and is positive otherwise. Figure 6.10 shows the values extracted for particular φ_0-shifts measured. Note that shift is non-linear function of the field. While for a small magnitude values of Bin-plane the anomalous current is negligible, above certain critical value of the field the shift abruptly increases.

6.8.7. ADDITIONAL DATA

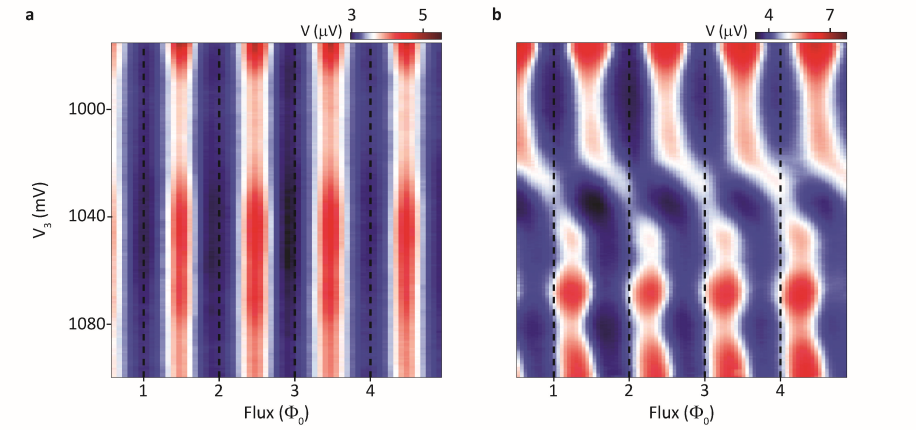

Figure 6.11: **Measured voltage as a function of flux and V_3 a,** $B_{in-plane} = 0$. **b,** $B_{in-plane} = 150$mT, $\theta = 75°$. In this regime no $0-\pi$ transition is observed suggesting that multiple quantum dot orbitals contribute to the transport. The phase shifts are mainly constant inside the regions of gate space in which the quantum dot occupation number is fixed. Gate settings are: $V_1 = 100$ mV; $V_2 = 50$ mV; $I_{bias} = 220$ pA; $V_{ref} = 450$ mV.

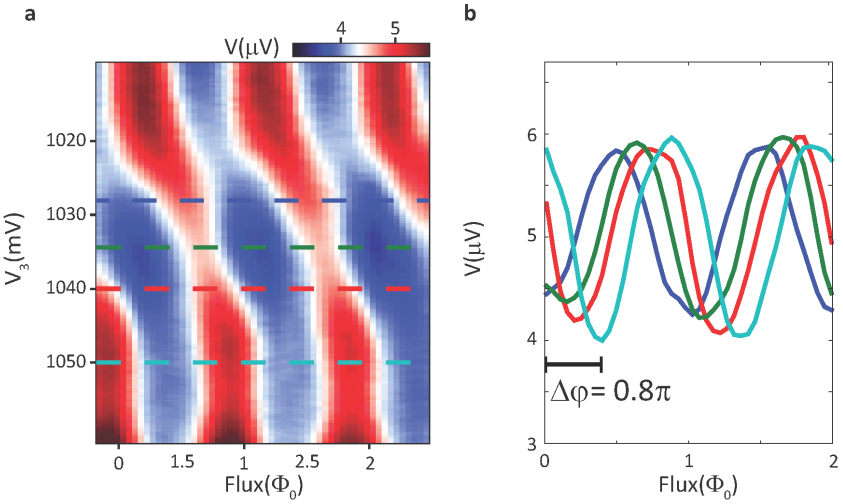

Figure 6.12: **Continuously gate tuneable φ_0-shift. a,** Zoom in on Figure 6.11**b**. The dashed lines represent the values of V_3 at which the curves in **b** are taken. **b,** Measured voltage vs flux taken at consecutive V_3 values marked in **a**. The total phase shift between the blue curve and cyan curve is 0.8π.

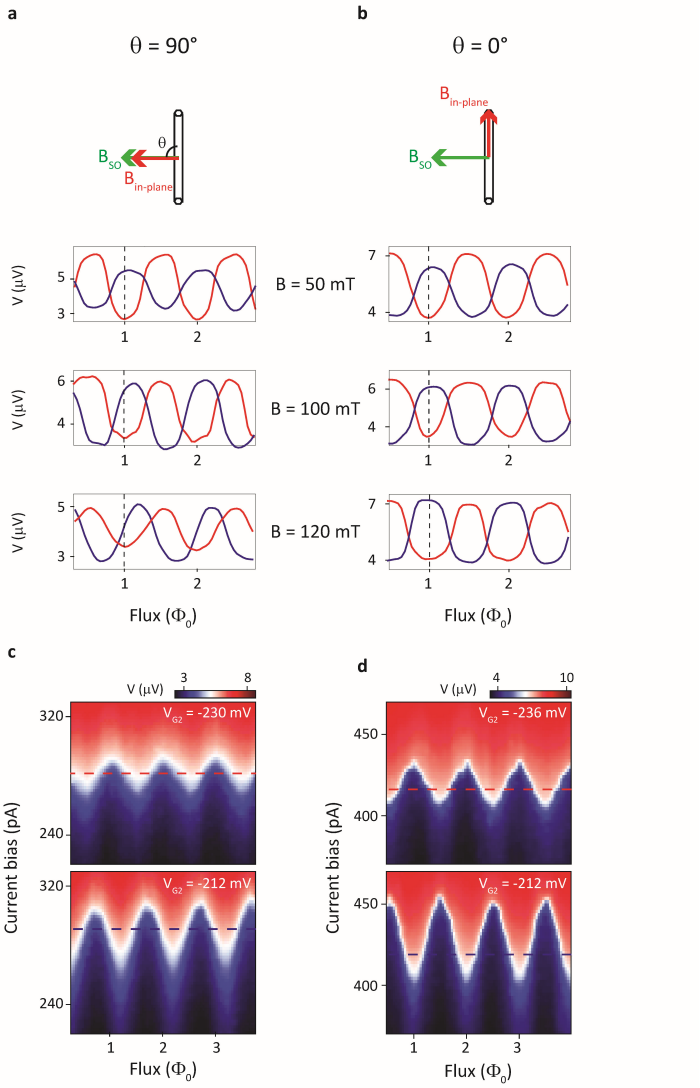

Figure 6.13: **Evolution of the shift in the SQUID pattern with the magnetic field for two different magnetic field orientations. a,** Orthogonal to the nanowire. **b,** Along the nanowire. The blue and red traces correspond to the two consecutive quantum dot occupation states. **c-d** Voltage as a function of flux and current bias at $B_{in-plane}$ = 120 mT for the same field orientation as in **a** and **b**. The sharp transition from the low voltage state (blue) to the high voltage state (red) indicates the value of the switching current as a function of flux. The phase offset is independent of the current bias. The red and blue lines correspond to the current bias at which the data in the lowest panel of **a** and **b** is taken.

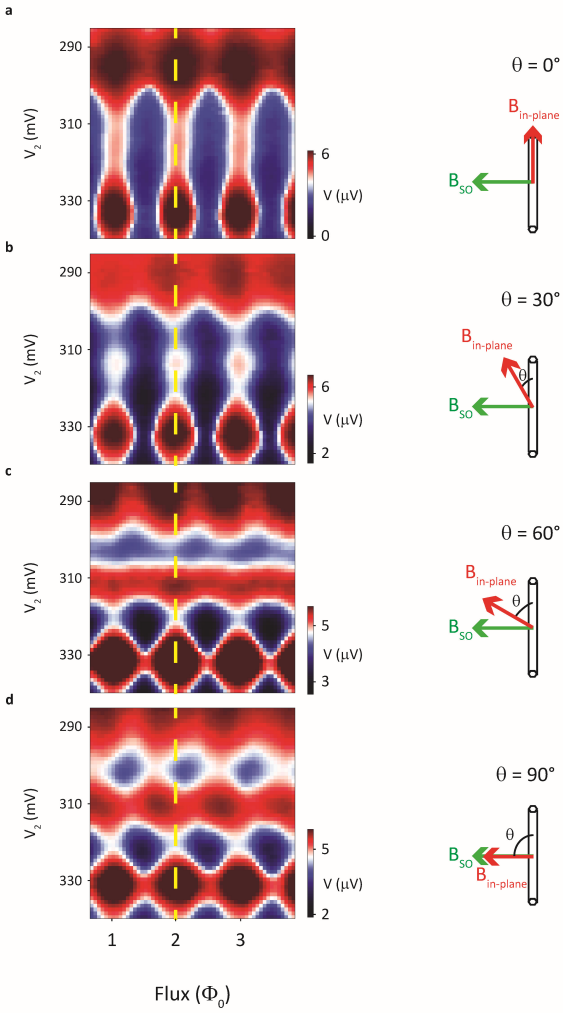

Figure 6.14: **Anisotropy of the SQUID phase shift in the open QD regime a-d,** Voltage as a function of V_2 and flux for different orientations of $B_{in-plane}$ and 30-50 more electrons compared to the regime in Figure 6.4. Here the $0-\pi$ transition was not observed strongly suggesting that multiple orbitals are contributing to the transport. In this very different regime compared to the data discussed in the main text the φ_0 shifts are still the largest when the external in-plane field ($B_{in-plane}$ = 100mT) is oriented orthogonal to the nanowire.

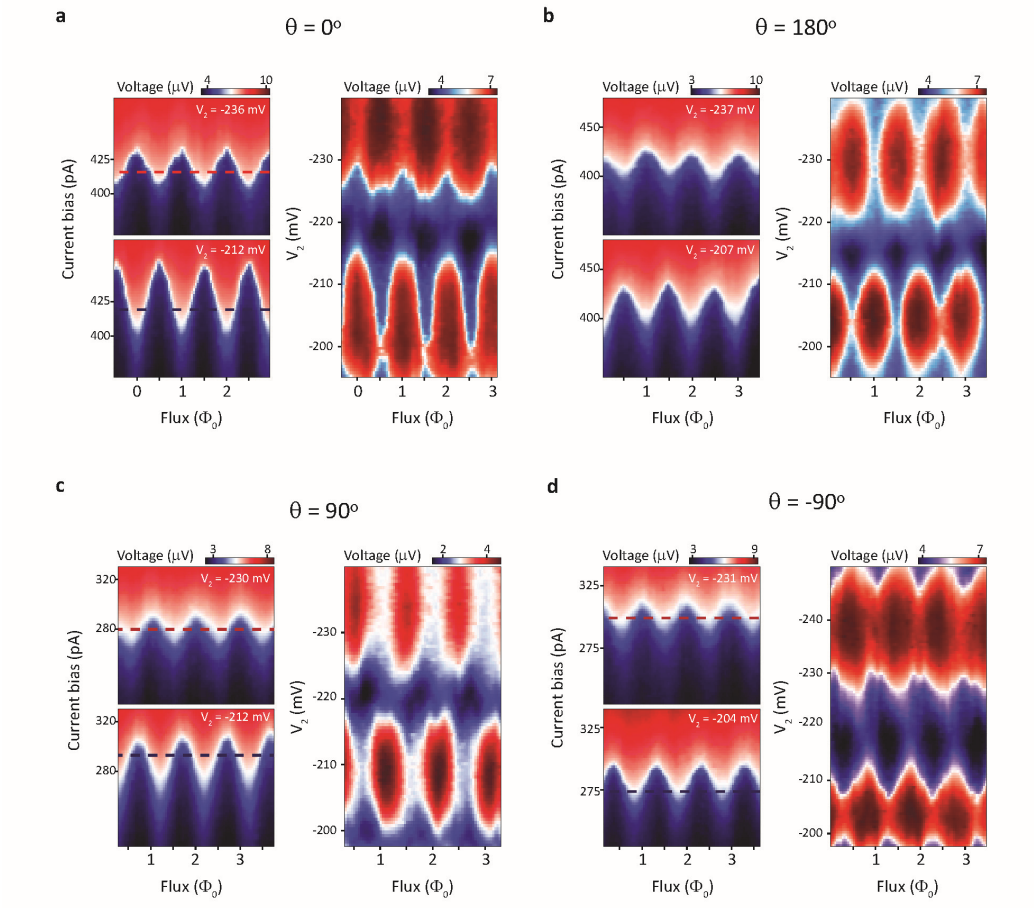

Figure 6.15: **Additional anisotropy data for** $B_{in-plane}$ = 120**mT. a-d,** The left panel shows voltage vs current bias and flux for the gate settings corresponding to two consecutive Coulomb blockade regions. The right panel shows voltage vs V_2 and flux. The angle θ between the nanowire and $\mathbf{B_{in-plane}}$ is indicated. Blue and red dashed lines indicate cuts shown in Figure 6.4. The corresponding values of the I_{bias} are: **a** top panel I_{bias} = 415 pA , bottom panel I_{bias} = 420pA; **c** I_{bias} = 280 pA, I_{bias} = 290 pA; **d** I_{bias} = 295 pA, I_{bias} = 275 pA.

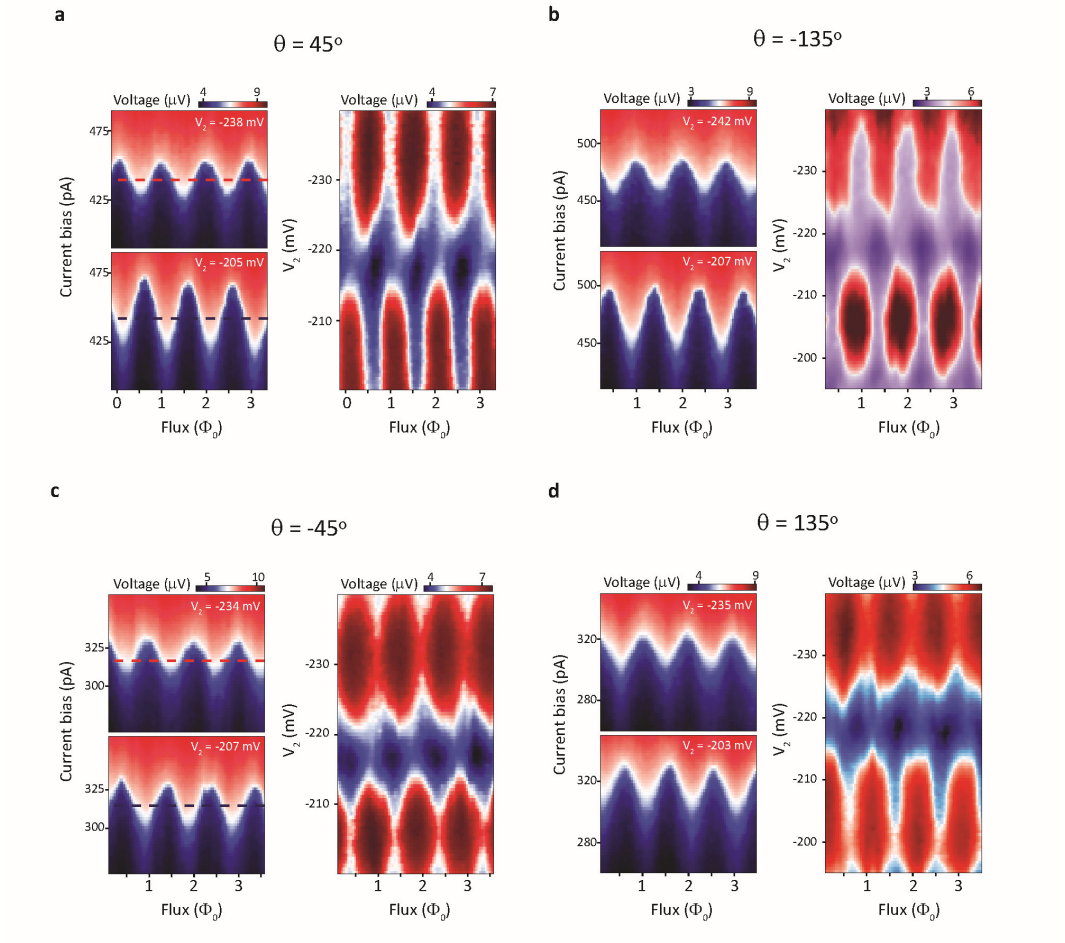

Figure 6.16: **Additional anisotropy data for $B_{in-plane}$ = 120mT. a-d,** The left panel shows voltage vs current bias and flux for the gate settings corresponding to two consecutive Coulomb blockade regions. The right panel shows voltage vs V_2 and flux. The angle θ between the nanowire and $\mathbf{B_{in-plane}}$ is indicated. Blue and red dashed lines indicate cuts shown in Figure 6.4. The corresponding values of the I_{bias} are: **a** top panel I_{bias} = 440 pA , bottom panel I_{bias} = 440pA; **c** I_{bias} = 320 pA, I_{bias} = 315 pA

BIBLIOGRAPHY

[1] B. D. Josephson, "Possible new effects in superconductive tunnelling," *Physics Letters*, vol. 1, pp. 251–253, July 1962.

[2] S.-K. Yip, O. F. De Alcantara Bonfim, and P. Kumar, "Supercurrent tunneling between conventional and unconventional superconductors: A Ginzburg-Landau approach," *Physical Review B*, vol. 41, pp. 11214–11228, June 1990.

[3] A. Buzdin, "Direct Coupling Between Magnetism and Superconducting Current in the Josephson φ_0 Junction," *Physical Review Letters*, vol. 101, p. 107005, Sept. 2008.

[4] A. A. Reynoso, G. Usaj, C. A. Balseiro, D. Feinberg, and M. Avignon, "Anomalous Josephson Current in Junctions with Spin Polarizing Quantum Point Contacts," *Physical Review Letters*, vol. 101, p. 107001, Sept. 2008.

[5] A. Zazunov, R. Egger, T. Jonckheere, and T. Martin, "Anomalous Josephson Current through a Spin-Orbit Coupled Quantum Dot," *Physical Review Letters*, vol. 103, p. 147004, Oct. 2009.

[6] A. Golubov, M. Y. Kupriyanov, and E. Il'Ichev, "The current-phase relation in josephson junctions," *Reviews of Modern Physics*, vol. 76, no. 2, p. 411, 2004.

[7] I. V. Krive, L. Y. Gorelik, R. I. Shekhter, and M. Jonson, "Chiral symmetry breaking and the josephson current in a ballistic superconductor–quantum wire–superconductor junction," *Low temperature physics*, vol. 30, no. 5, pp. 398–404, 2004.

[8] J.-F. Liu and K. S. Chan, "Anomalous Josephson current through a ferromagnetic trilayer junction," *Physical Review B*, vol. 82, p. 184533, Nov. 2010.

[9] Y. Tanaka, T. Yokoyama, and N. Nagaosa, "Manipulation of the majorana fermion, andreev reflection, and josephson current on topological insulators," *Physical review letters*, vol. 103, no. 10, p. 107002, 2009.

[10] F. Dolcini, M. Houzet, and J. S. Meyer, "Topological Josephson φ_0 junctions," *Physical Review B*, vol. 92, p. 035428, July 2015.

[11] F. S. Bergeret and I. V. Tokatly, "Theory of diffusive φ_0 Josephson junctions in the presence of spin-orbit coupling," *EPL (Europhysics Letters)*, vol. 110, no. 5, p. 57005, 2015.

[12] M. Alidoust and J. Linder, "φ-state and inverted Fraunhofer pattern in nonaligned Josephson junctions," *Physical Review B*, vol. 87, p. 060503, Feb. 2013.

[13] T. Yokoyama, M. Eto, and Y. V. Nazarov, "Anomalous Josephson effect induced by spin-orbit interaction and Zeeman effect in semiconductor nanowires," *Physical Review B*, vol. 89, p. 195407, May 2014.

[14] G. Campagnano, P. Lucignano, D. Giuliano, and A. Tagliacozzo, "Spin–orbit coupling and anomalous Josephson effect in nanowires," *Journal of Physics: Condensed Matter*, vol. 27, p. 205301, May 2015.

[15] L. Dell'Anna, A. Zazunov, R. Egger, and T. Martin, "Josephson current through a quantum dot with spin-orbit coupling," *Physical Review B*, vol. 75, p. 085305, Feb. 2007.

[16] A. Brunetti, A. Zazunov, A. Kundu, and R. Egger, "Anomalous Josephson current, incipient time-reversal symmetry breaking, and Majorana bound states in interacting multilevel dots," *Physical Review B*, vol. 88, p. 144515, Oct. 2013.

[17] E. Goldobin, D. Koelle, R. Kleiner, and R. G. Mints, "Josephson Junction with a Magnetic-Field Tunable Ground State," *Physical Review Letters*, vol. 107, p. 227001, Nov. 2011.

[18] H. Sickinger, A. Lipman, M. Weides, R. G. Mints, H. Kohlstedt, D. Koelle, R. Kleiner, and E. Goldobin, "Experimental Evidence of a φ Josephson Junction," *Physical Review Letters*, vol. 109, p. 107002, Sept. 2012.

[19] C. Fasth, A. Fuhrer, L. Samuelson, V. N. Golovach, and D. Loss, "Direct Measurement of the Spin-Orbit Interaction in a Two-Electron InAs Nanowire Quantum Dot," *Physical Review Letters*, vol. 98, p. 266801, June 2007.

[20] S. Nadj-Perge, S. M. Frolov, E. P. a. M. Bakkers, and L. P. Kouwenhoven, "Spin-orbit qubit in a semiconductor nanowire," *Nature*, vol. 468, pp. 1084–1087, Dec. 2010.

[21] J. A. van Dam, Y. V. Nazarov, E. P. A. M. Bakkers, S. De Franceschi, and L. P. Kouwenhoven, "Supercurrent reversal in quantum dots," *Nature*, vol. 442, pp. 667–670, Aug. 2006.

[22] M. Della Rocca, M. Chauvin, B. Huard, H. Pothier, D. Esteve, and C. Urbina, "Measurement of the current-phase relation of superconducting atomic contacts," *Physical review letters*, vol. 99, no. 12, p. 127005, 2007.

[23] J. Pillet, C. Quay, P. Morfin, C. Bena, A. L. Yeyati, and P. Joyez, "Andreev bound states in supercurrent-carrying carbon nanotubes revealed," *Nature Physics*, vol. 6, no. 12, pp. 965–969, 2010.

[24] W. Chang, V. Manucharyan, T. S. Jespersen, J. Nygård, and C. M. Marcus, "Tunneling spectroscopy of quasiparticle bound states in a spinful josephson junction," *Physical review letters*, vol. 110, no. 21, p. 217005, 2013.

[25] J.-P. Cleuziou, W. Wernsdorfer, V. Bouchiat, T. Ondarçuhu, and M. Monthioux, "Carbon nanotube superconducting quantum interference device," *Nature nanotechnology*, vol. 1, no. 1, pp. 53–59, 2006.

[26] J. Linder and J. W. Robinson, "Superconducting spintronics," *Nature Physics*, vol. 11, no. 4, pp. 307–315, 2015.

[27] M. Leijnse and K. Flensberg, "Parity qubits and poor man's majorana bound states in double quantum dots," *Physical Review B*, vol. 86, no. 13, p. 134528, 2012.

[28] I. C. Fulga, A. Haim, A. R. Akhmerov, and Y. Oreg, "Adaptive tuning of majorana fermions in a quantum dot chain," *New Journal of Physics*, vol. 15, no. 4, p. 045020, 2013.

[29] F. Konschelle, I. V. Tokatly, and F. S. Bergeret, "Theory of the spin-galvanic effect and the anomalous phase shift φ 0 in superconductors and josephson junctions with intrinsic spin-orbit coupling," *Physical Review B*, vol. 92, no. 12, p. 125443, 2015.

[30] A. Zyuzin, M. Alidoust, and D. Loss, "Josephson junction through a disordered topological insulator with helical magnetization," *Physical Review B*, vol. 93, no. 21, p. 214502, 2016.

[31] P. San-Jose, E. Prada, and R. Aguado, "Mapping the Topological Phase Diagram of Multiband Semiconductors with Supercurrents," *Phys. Rev. Lett.*, vol. 112, p. 137001, Apr. 2014.

[32] P. Marra, R. Citro, and A. Braggio, "Signatures of topological phase transitions in Josephson current-phase discontinuities," *Physical Review B*, vol. 93, June 2016. arXiv: 1508.01799.

[33] C. Padurariu and Y. V. Nazarov, "Theoretical proposal for superconducting spin qubits," *Physical Review B*, vol. 81, p. 144519, Apr. 2010.

[34] E. C. Gingrich, B. M. Niedzielski, J. A. Glick, Y. Wang, D. L. Miller, R. Loloee, W. P. Pratt Jr, and N. O. Birge, "Controllable 0-π Josephson junctions containing a ferromagnetic spin valve," *Nat Phys*, vol. 12, pp. 564–567, June 2016.

[35] A. A. Reynoso, G. Usaj, C. A. Balseiro, D. Feinberg, and M. Avignon, "Spin-orbit-induced chirality of Andreev states in Josephson junctions," *Physical Review B*, vol. 86, p. 214519, Dec. 2012.

[36] R. Delagrange, R. Weil, A. Kasumov, M. Ferrier, H. Bouchiat, and R. Deblock, "0-π quantum transition in a carbon nanotube Josephson junction: Universal phase dependence and orbital degeneracy," *Phys. Rev. B*, vol. 93, p. 195437, May 2016.

[37] S. R. Plissard, D. R. Slapak, M. A. Verheijen, M. Hocevar, G. W. G. Immink, I. van Weperen, S. Nadj-Perge, S. M. Frolov, L. P. Kouwenhoven, and E. P. A. M. Bakkers, "From InSb Nanowires to Nanocubes: Looking for the Sweet Spot," *Nano Lett.*, vol. 12, pp. 1794–1798, Apr. 2012.

[38] V. Mourik, K. Zuo, S. M. Frolov, S. R. Plissard, E. P. a. M. Bakkers, and L. P. Kouwenhoven, "Signatures of Majorana Fermions in Hybrid Superconductor-Semiconductor Nanowire Devices," *Science*, vol. 336, pp. 1003–1007, May 2012.

[39] R. Feynman, R. Leighton, and M. Sands, "The feynman lectures on physics, the definitive edition volume 3 (feynman lectures on physics (hardcover))," 2005.

[40] P. Jarillo-Herrero, J. A. van Dam, and L. P. Kouwenhoven, "Quantum supercurrent transistors in carbon nanotubes," *Nature*, vol. 439, pp. 953–956, Feb. 2006.

[41] S. De Franceschi, L. Kouwenhoven, C. Schönenberger, and W. Wernsdorfer, "Hybrid superconductor-quantum dot devices," *Nature Nanotechnology*, vol. 5, pp. 703–711, Oct. 2010.

[42] S. Nadj-Perge, V. S. Pribiag, J. W. G. van den Berg, K. Zuo, S. R. Plissard, E. P. A. M. Bakkers, S. M. Frolov, and L. P. Kouwenhoven, "Spectroscopy of Spin-Orbit Quantum Bits in Indium Antimonide Nanowires," *Phys. Rev. Lett.*, vol. 108, p. 166801, Apr. 2012.

7

OUTLOOK

This chapter offers improvements on the experiments described in the previous chapters and follow up experiments, mainly having in mind the goal of measuring Majorana fermions and topological state of matter in InSb nanowires and nanocrosses.

7.1. IMPROVING THE CONTACT PREPARATION - EPITAXIAL CONTACTS

All experiments in this thesis involve proximitizing an InSb nanowire with NbTiN superconducting contacts. The interface between the nanowire and the superconductor is therefore crucial both to induce a strong gap inside the nanowire and to avoid subgap states within the induced gap. Improving the interface could significantly augment the critical current values of InSb SNS junctions and increase the magnetic field limit at which supercurrent can be detected. Thus the interface needs to be as close to perfect crystallographic as possible and clean from residues and impurities that may come from removing the surface oxide of the nanowire.

The devices presented in this thesis were prepared by etching the native oxide in an Argon plasma environment before contact deposition. The plasma accelerates the charged Argon ions towards the sample, resulting in an ion bombardment of the nanowire, knocking off the oxide molecules. Although the method is effective at removing the oxide, it is an invasive procedure which destroys the crystalline surface of the wire. Since the process happens at relatively high pressures the contact area may also be contaminated from impurities in the sputtering machine, such as carbon.

Sulphur passivation, being a less invasive procedure, can improve results compared to Argon etching[1]. Ideally though, best results can be achieved if the contact is deposited in-situ with the nanowire growth, preventing the formation of an oxide barrier all together. This method used on InAs nanowires with in-situ evaporated aluminium produced an epitaxial interface and very low subgap conductance[2]. Achieving similar results with InSb and high critical field superconductor would prove to be a significant breakthrough for superconducting devices and Majorana experiments.

7.2. REDUCING SUPERCONDUCTING INTERFERENCE WITHIN THE JUNCTION

In chapter 4 we studied the critical current of InSb SNS Josephson junctions as a function of the strength and direction of an external magnetic field. The junctions measured were of various lengths from 100 nm to ~ 1 μm. Our results show that the critical current decays rapidly to below 1 nA irrespective of the zero field value beyond 100 mT. Following the rapid decay, I_C shows Fraunhofer-like interference as a function of magnetic field, but aperiodic and the critical current not necessarily reaching zero where the interference is destructive. The field values where I_C is maximum or minimum varies as the chemical potential or the field angle is changed.

This interference can be caused by either spin-dependent phase shifts due to a finite Zeeman splitting and spin-orbit interaction or intermode phase shifts due to a finite flux enclosed between different orbital modes. The latter effect is more likely as it explains the rapid fall in I_C and it is anticipated to occur at lower field values for junctions occupying multiple modes. In the context of using such nanowire Josephson junctions as elements of a topological qubit braiding circuit, the interference is undesirable as it causes abrupt variations in I_C and hence E_J. If the initial decay in I_C is caused by the destructive interference of orbital modes, than E_J is severely reduced compared to its achievable maximum. More importantly, the interference of orbital modes substantially alters the topological phase diagram, possibly suppressing the topological gap protecting Majorana bound states [3].

The following improvements can allow to discriminate between the cause of the interference and moderate its effects:

- Assuming the enclosed flux between orbital modes is the main cause of the interference, the magnetic field scale at which the effect is apparent is proportional to the areal cross-section of the wire seen by the magnetic field. Unfortunately in this thesis we only measured angle dependent critical current for short junctions of length ~ 100 – 200 nm where the cross-section of the wire does not substantially vary whether the field is directed along or perpendicular to the wire. For junctions of length of the order of ~ 1μm, however, the oscillations should occur at a much lower field scale when the field is perpendicular to the wire.

- The effect of interfering orbital modes can be reduced by tuning the wire to the single mode regime. This is hard to achieve via gating, especially since the electrostatic gates are ineffective on the wire sections which are covered by a metallic contact. Reducing the wire diameter itself, however, would increase the subband spacing inside the wire. Currently the average wire diameter of 100 – 120 nm results in a subband spacing of 15 meV. A wire of diameter 50 – 60 nm would quadruple the energy between subbands, making the regime of a single occupied mode experimentally reachable and thus interference avoidable.

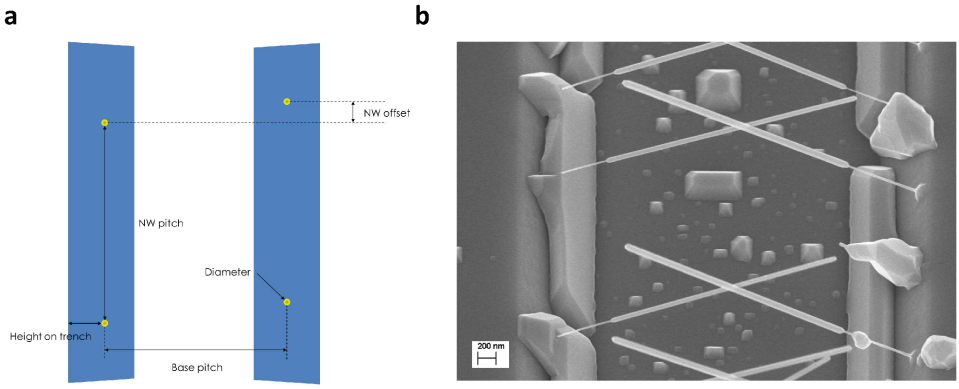

Figure 7.1: **Lithographically patterned nanocross fabrication. a,** Schematics of the trench on the sides of which the nanowires are grown. Parameters of the growth determining the placement of the gold particles from which the wires nucleate are shown. **b,** SEM image of the growth chip after nanowire growth. Individual wires growing on the opposite sides of the trench merge together to from a nanocross. Images copied from Reference[4].

7.3. IMPROVING THE YIELD AND QUALITY OF SEMICONDUCTING NANOCROSSES

We have studied the electronic properties of InSb nanocrosses in two chapters of this thesis.

- **Superconducting nanowire networks** (Chapter 4): The conductance and the supercurrent is measured between the four terminals of a nanowire cross. A finite size supercurrent is measured via all terminals.
- **Resonant Andreev reflection through a three terminal nanowire quantum dot** (Chapter 5): The three terminals of a nanowire T-junction are used as a normal tunnel probe and two superconductors joined in a loop to enable flux biasing. A quantum dot is created at the intersection. Flux periodic oscillations are measured for finite voltage bias at specific chemical potential, identified as resonant Andreev reflection through the dot. These oscillations persist at finite magnetic field up to 600 mT.

These experiments require the transfer of suitable nanowire crosses from the growth chip to the silicone substrate on which the device is patterned. However the yield of crosses on the growth chip was extremely low. This rendered the fabrication time of devices very long, but more importantly resulted in very few devices per fabrication run offering no alternatives for better contact resistances. Reproducing the experiment and obtaining even a single good device is thus difficult.

Our yield was low because the nanowire pair forming the nancross grew skew for the majority of the cross structures transferred from the growth chip. Skew nancrosses result in non-coplanar arms and consequently not all arms could be contacted for most devices, as one arm is lifted from the substrate. Moreover, only about 8% of the crosses

have an optimal crossing angle $\varphi = 70.5°$ required for a single crystalline intersection. This yield was improved to 25% by Diana Car and her colleagues in Eindhoven [5] by patterning deterministically the location of the gold catalyst, kinking the InP stem during growth and growing InSb directly on the InP. This method can be further improved as in [4] to give a 50% yield on single crystalline wires by growing InSb on InP trenches inclined at the desired angle of 70.5°. This way the wires will grow towards each other at the correct angle with a user controlled offset defined by the lithographically patterned displacement of the gold particles (see Figure 7.1). The 50% yield is a result of the number of rotational twins formed in the wire during growth. In order for a single crystalline nanocross to form, the parity of twins in each wire section of the cross should be equal (i.e. odd-odd or even-even).

7.4. FURTHER EXPERIMENTS WITH NANOWIRE NETWORKS

On obvious goal for the semiconducting nanowire networks is to implement them in the Majorana braiding scheme as a component in the topological quantum computer. In the proposals involving these networks, the quantum operations are implemented by physically exchanging the Majorana states in the 2D plane, either via electrostatic gating [6] or fusing them by varying the superconducting phase [7]. Since the wire is quasi one-dimensional, such an exchange requires a branched wire. Although these schemes are promising, they have a disadvantage: the magnetic field necessary to drive the wire into the topologically trivial regime cannot be aligned with all wire sections, by virtue of the branching of the wires. A large magnetic field with a component perpendicular to the wire may exasperate the effects of interfering orbital modes and possibly completely kill the topological gap as mentioned earlier. Thus if the magnetic field is misaligned compared to the wire axis, the topologically trivial regime may be impossible to reach. This problem can be cured of the wire is tuned uniformly to the single subband occupation regime, in which case there can be no interference. More recent proposals are bridging this obstacle by measurement-based protocols, where the quantum operations are carried out by measuring the state of the qubits instead of braiding[8, 9].

Nevertheless, these semiconducting wire networks are a remarkable platform to explore low-dimensional superconducting physics. The shape of the nanocross offers the possibility to probe the local density of states of a proximitized nanowire. This offers a new possibility to descriminate Majorana boud state induced zero-bias conductance peaks from other mechanisms such as disorder[10]. The device geometry depicted in Figure 7.2**a** allows to probe the density of states from both sides of the topogogical superconductor as well as tunneling from the middle of the proximitzed region. If the area of the proximitized region forms a single continuous topogogically non-trivial superconductor, the MBS wavefunction is amplitude is substantial on the edge and is exponentially small in the center of the region. Thus probing from the side contacts would result in measuring a zero-bias conductance peak, as opposed to tunneling from the middle probe. A conductance peak formed by disorder, however, would give a uniform conductance from all sides.

The nanowire networks are also suitable to fabricate multiterminal Josephson junctions as shown in Figure 7.2**b**. A JJ with n terminals gives a parameter space of $n-1$ phase differences $\varphi_1,..,\varphi_{n-1}$. For $n>2$, the phases can be used to break time reversal sym-

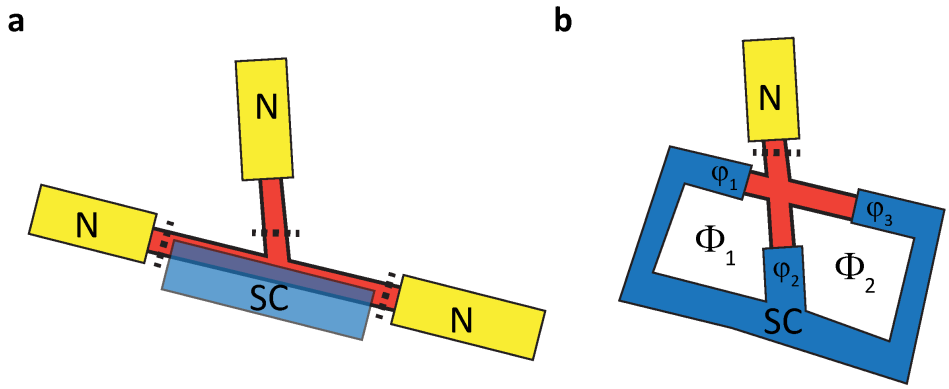

Figure 7.2: **Suggested experiments using nanowire networks. a,** Measurement of the local density of states. The middle of the wire is covered with a superconductor, and local gates (dashed lines) are mounted on the three wire sections adjacent to the superconductor. The wire may be probed both along the contact and through the middle of the contact. **b,** Multiterminal Josephson junction scheme.

metry and thus break Kramer's degeneracy of half-integer spin levels. In other words, spin-manipulation is possible by tuning the phases and a large magnetic field is not necessary. Majorana bound states or other exotic topologically protected quasiparticles, such as Weyl fermions, may be engineered in multiterminal junctions without the application of any magnetic field beyond the microtesla regime[11, 12]. Such phase biasing may be achieved by connecting three terminals with two superconducting loops and apply local flux bias to each loop, as shown in Figure 7.2**b**. The fourth terminal is used as a tunnel probe to measure the zero-bias conductance features. To break the spin degeneracy with the superconducting phase, it is necessary that the junctions fall in the short junction limit: $L \ll \xi_0 = \frac{\hbar v_F}{\pi \Delta}$, with ξ_0 the coeherence lenght of electrons. This is feasible with semiconducting nanowires ($\xi_0 \sim 100$nm) but experimentally unreachable with conventional metallic junctions ($\xi_0 \sim 1$nm) .

7.5. JOSEPHSON φ_0-JUNCTION

In Chapter 6 we present an InSb nanowire embedded into a dc-SQUID for phase biasing. The supercurrent as a function of phase and magnetic field is measured through a gate defined quantum dot inside the nanowire. At zero in-plane magnetic field a π-transition of the supercurrent phase is measured as the ground state parity of the dot changes. At finite field, as long as the field has a component pointing parallel to the intrinsic SOI of the QD, the ground state supercurrent acquires a phase φ_0 different from zero or π, implying an anomalous supercurrent flow at zero phase difference across the dot.

Because the control junction constituting the other arm of the dc-SQUID is also nanowire based, the absolute phase change in the ground state φ_0 or the magnitude of the anomalous current I_a could not be measured. In order to measure the absolute phase shift, the reference junction of the SQUID needs to be a standard SIS junction, in the sense that its CPR is known exactly both at zero and finite field. If this is the case, the exact phase drop over the reference junction is known and the phase over the quantum

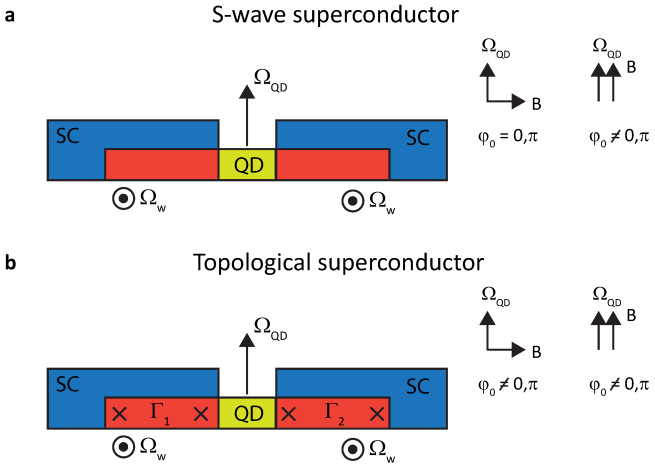

Figure 7.3: **Experimental schematics for detecting the topological phase by measuring φ_0 through a nanowire quantum dot. a,** Nanowire quantum dot connected to s-wave superconducting leads. $\Omega_{\mathbf{W}}$ and $\Omega_{\mathbf{QD}}$ show the direction of the effective SOI in the wire and dot sections respectively. Inset: Possible values of φ_0 depending on the angle between $\Omega_{\mathbf{QD}}$ and the external magnetic field **B**. **b,** Same as **a** with the s-wave wire section replaced by topological superconductors with parity Γ_1, Γ_2.

dot and thus the CPR can be deduced. If φ_0 and I_a are extracted, an estimate of the SOI strength can be made, independent from the estimates established via singlet-triplet splitting[13] and weak anti-localization measurements[14].

7.5.1. DEMONSTRATING TOPOLOGICAL PHASE IN A JOSEPHSON φ_0-JUNCTION

The ingredients necessary for an anomalous current to flow in a nanowire quantum dot are the same as for driving the wire into the topological regime, namely SOI and a finite Zeeman splitting inside a one dimensional semiconductor. Schrade et al. [15] show an intimate relationship between measuring an anomalous current and the topologically non-trivial phase bearing Majorana bound states. Measuring the phase shift φ_0 can be a qualitative sign of the topological phase of the nanowire sections adjacent to the dot. A brief description of the experiment is given below.

Schrade et al. calculate the effective tunneling Hamiltonian and thus the dissipationless supercurrent (which is the phase derivative of the tunneling Hamiltonian) of a quantum dot with two orbitals, connected to either standard s-wave superconducting leads(s-wave system) or topological superconducting leads with MBS(TS system), as shown in Figure 7.3. The chemical potential on the dot is such that the dot it is doubly occupied. The external magnetic field strength B is set close to the singlet-triplet anti-crossing of the dot levels, as level-mixing is necessary to induce an anomalous current. Where the metallic leads cover the wire, the effective SOI $\Omega_{\mathbf{W}}$ points in the plane of the substrate perpendicular to the wire. At the uncovered section of the wire where the QD is defined, the SOI vector $\Omega_{\mathbf{QD}}$ points perpendicular to the wire and the substrate. When the external magnetic field **B** is rotated in the plane of the wire perpendicular to the

substrate, such that when $B > B_c$ (where B_c is the critical field needed to drive the wire topological) the wire is always in the topologically non-trivial state.

For $B < B_c$, the leads are s-wave superconductors (Figure 7.3**a**). When the external magnetic field vector **B** is not orthogonal to the spin-orbit field $\Omega_{\mathbf{QD}}$, the ground state phase of the junction shifts by an angle $\varphi_0 \neq 0, \pi$. Both chiral and time reversal symmetry is broken and an anomalous current flows at zero phase difference across the dot. The chiral symmetry is broken by the SOI, which mixes the two orbitals of the dot, and allows electrons to tunnel through both orbitals without flipping spin. When **B** is orthogonal to $\Omega_{\mathbf{QD}}$, this process of electrons changing orbital without flipping spin is prohibited, and chiral symmetry is restored. The ground state phase is restricted to 0 and π.

For $B > B_c$, the leads are topological and electrons tunnel to the dot via non-local Majorana bound states. This system does not preserve chiral symmetry even when $\mathbf{B} \perp \Omega_{\mathbf{QD}}$. This is because the topologically non-trivial leads do not transform into each other after mirroring. The anomalous current flowing depends on the parity of the leads $\Gamma_1\Gamma_2$ and is non-zero, and thus $\varphi_0 \neq 0, \pi$. To detect the phase shift, however, one has to measure faster than the parity lifetime of the MBS, otherwise the anomalous current signal is washed out.

During the experiment, the external field **B** is first oriented along the wire axis. The phase φ_0 is monitored at a rate faster than the parity lifetime of MBS. As the field is increased beyond B_c, the phase φ_0 is expected to jump from 0 or π to a different value indicating the transition to the topologically non-trivial regime. To double-check if this si the case, **B** can be rotated in the plane containing the wire and $\Omega_{\mathbf{QD}}$ for the cae $B < B_c$ and $B > B_c$. The phase shift φ_0 would in the case of $B > B_c$ remain constant and different from 0 or π, whereas in the case of $B < B_c$ the phase goes to zero or π as the field direction is aligned with the wire.

BIBLIOGRAPHY

[1] H. Zhang, Ö. Gül, S. Conesa-Boj, K. Zuo, V. Mourik, F. K. de Vries, J. van Veen, D. J. van Woerkom, M. P. Nowak, M. Wimmer, D. Car, S. Plissard, E. P. A. M. Bakkers, M. Quintero-Pérez, S. Goswami, K. Watanabe, T. Taniguchi, and L. P. Kouwenhoven, "Ballistic Majorana nanowire devices," *arXiv:1603.04069 [cond-mat]*, Mar. 2016. arXiv: 1603.04069.

[2] W. Chang, S. M. Albrecht, T. S. Jespersen, F. Kuemmeth, P. Krogstrup, J. Nygård, and C. M. Marcus, "Hard gap in epitaxial semiconductor-superconductor nanowires," *Nat Nano*, vol. 10, pp. 232–236, Mar. 2015.

[3] B. Nijholt and A. R. Akhmerov, "Orbital effect of magnetic field on the Majorana phase diagram," *Phys. Rev. B*, vol. 93, p. 235434, June 2016.

[4] S. C. Balk, *Fabrication methods for high yield Majorana braiding networks*. MSc thesis, TU Delft, Jan. 2016.

[5] D. Car, J. Wang, M. A. Verheijen, E. P. A. M. Bakkers, and S. R. Plissard, "Rationally Designed Single-Crystalline Nanowire Networks," *Adv. Mater.*, vol. 26, pp. 4875–4879, July 2014.

[6] J. Alicea, Y. Oreg, G. Refael, F. von Oppen, and M. P. A. Fisher, "Non-Abelian statistics and topological quantum information processing in 1d wire networks," *Nat Phys*, vol. 7, pp. 412–417, May 2011.

[7] T. Hyart, B. van Heck, I. C. Fulga, M. Burrello, A. R. Akhmerov, and C. W. J. Beenakker, "Flux-controlled quantum computation with Majorana fermions," *Phys. Rev. B*, vol. 88, p. 035121, July 2013.

[8] P. Bonderson, M. Freedman, and C. Nayak, "Measurement-Only Topological Quantum Computation," *Phys. Rev. Lett.*, vol. 101, p. 010501, June 2008.

[9] T. Karzig, C. Knapp, R. Lutchyn, P. Bonderson, M. Hastings, C. Nayak, J. Alicea, K. Flensberg, S. Plugge, Y. Oreg, C. Marcus, and M. H. Freedman, "Scalable Designs for Quasiparticle-Poisoning-Protected Topological Quantum Computation with Majorana Zero Modes," *arXiv:1610.05289 [cond-mat, physics:quant-ph]*, Oct. 2016. arXiv: 1610.05289.

[10] J. Liu, A. C. Potter, K. T. Law, and P. A. Lee, "Zero-Bias Peaks in the Tunneling Conductance of Spin-Orbit-Coupled Superconducting Wires with and without Majorana End-States," *Phys. Rev. Lett.*, vol. 109, p. 267002, Dec. 2012.

[11] B. van Heck, S. Mi, and A. R. Akhmerov, "Single fermion manipulation via superconducting phase differences in multiterminal Josephson junctions," *Phys. Rev. B*, vol. 90, p. 155450, Oct. 2014.

[12] R.-P. Riwar, M. Houzet, J. S. Meyer, and Y. V. Nazarov, "Multi-terminal Josephson junctions as topological matter," *Nature Communications*, vol. 7, p. 11167, Apr. 2016.

[13] S. Nadj-Perge, V. S. Pribiag, J. W. G. van den Berg, K. Zuo, S. R. Plissard, E. P. A. M. Bakkers, S. M. Frolov, and L. P. Kouwenhoven, "Spectroscopy of Spin-Orbit Quantum Bits in Indium Antimonide Nanowires," *Phys. Rev. Lett.*, vol. 108, p. 166801, Apr. 2012.

[14] I. van Weperen, B. Tarasinski, D. Eeltink, V. S. Pribiag, S. R. Plissard, E. P. A. M. Bakkers, L. P. Kouwenhoven, and M. Wimmer, "Spin-orbit interaction in InSb nanowires," *Phys. Rev. B*, vol. 91, p. 201413, May 2015.

[15] C. Schrade, S. Hoffman, and D. Loss, "Detecting Topological Superconductivity with φ_0 Josephson Junctions," *arXiv:1607.07794 [cond-mat]*, July 2016. arXiv: 1607.07794.

A

MAJORANA PHYSICS IN SEMICONDUCTING NANOWIRES

The idea of Majorana particles came from the Italian physicist Ettore Majorana [1] who found a real solution to Dirac's equation for spin 1/2 paricles of mass m. A real solution implies that Majoranas are their own antiparticles, that is a Majorana creation operator $\gamma^\dagger$ satisfies

$$\gamma = \gamma^\dagger. \tag{A.1}$$

Although Majorana was thinking in the context of particle physics, nearly 70 years later condensed matter physicists [2–4] found similarly behaving quasiparticle exitations in condensed matter systems.

Condensed matter Majoranas form a system of non-Abelian anyons with a highly degenerate ground state: upon the exchange of two Majoranas the overall wavefunction gains a phase which depends on the exchange order.

The ground state of this system is gapped in energy from its excited states, consituting a platform for fault tolerant topological quantum computing [5]. Computation is done by exchanging pairs of Majoranas, while remaining in the degenerate ground state, a process called braiding [3]. The excitation gap guarantees the system doesn't couple to the environment and thus there is no source for decoherence.

In this section we review how Majoranas arise in semiconducting nanowires with induced superconductivity, and experimental methods on how to detect them.

A.1. FORMATION OF MAJORANA BOUND STATES IN SUPERCONDUCTING NANOWIRES WITH SPIN-ORBIT COUPLING

We work in the semiconductor representation of the solutions to a 1D superconducting Hamiltonian H_{BdG} derived in section**??**. The space of excitations is spanned by the four dimensional basis: $\gamma^\dagger_{E\uparrow}, \gamma^\dagger_{E\downarrow}, \gamma^\dagger_{-E\downarrow}, \gamma^\dagger_{-E\uparrow}$.

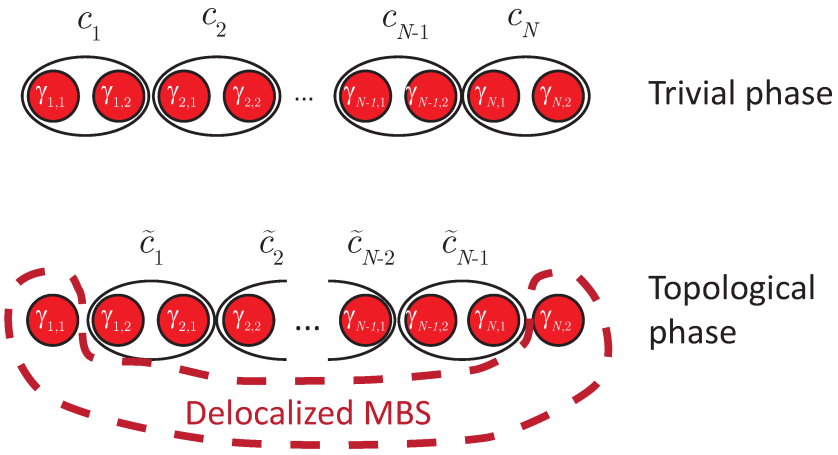

Figure A.1: **One dimensional Kitaev chain of Fermions in non-topological vs. topological regime.**

There are two excitations with opposite spin and positive energy $(\gamma^\dagger_{E\uparrow}, \gamma^\dagger_{E\downarrow})$ and two with negative energy $(\gamma^\dagger_{-E\uparrow}, \gamma^\dagger_{-E\downarrow})$. However the solutions are redundant since adding a particle of energy E ans spin σ is equivalent to removing a particle of energy $-E$ and with spin $-\sigma$:

$$\gamma^\dagger_{E\sigma} = \gamma_{-E-\sigma}$$

If spin could be ignored, the above equation for $E = 0$ would satisfy the Majorana condition A.1 and the zero energy quasiparticle excitations would behave as real solutions to Dirac's equation.

The pairing potential in an s-wave BCS superconductor pairs electrons of opposite spin. However, one can consider p-wave paired superconductors, where the pairing potential pairs electrons of the same spin. Thus excitations in a superconductor with p-wave paring take the form

$$\gamma^\dagger_{E\sigma} \equiv u^\star c^\dagger_\sigma - v^\star c_\sigma \tag{A.2}$$
$$\gamma^\dagger_{-E\sigma} \equiv u c_\sigma - v c^\dagger_\sigma \tag{A.3}$$

Which implies

$$\gamma^\dagger_{0\sigma} = \gamma_{0\sigma}. \tag{A.4}$$

How do these Majorana excitations arise in a one-dimensional p-wave superconductor? In Kitaev's toy model the Hamiltonian of a 1D p-wave superconductor composed of a chain of N fermions $c^\dagger_i$ can be written

$$\mathscr{H}_{Kitaev} = -\mu \sum_1^N c^\dagger_i c_i - \sum_1^{N-1} (t c^\dagger_i c_{i+1} + \Delta c_i c_{i+1} + h.c.) \tag{A.5}$$

where μ is the chemical potential, t a hopping paramter standing for kinetic energy and Δ is the p-wave pairing [1].

Each fermion can be decomposed into two half fermions in the following way:

$$\begin{aligned} c_i &= \tfrac{1}{2}(\gamma_{i,1} + i\gamma_{i,2}) \\ c_i^\dagger &= \tfrac{1}{2}(\gamma_{i,1} - i\gamma_{i,2}) \end{aligned} \tag{A.6}$$

One can check that the γ operators defined as such indeed obey the Majorana equation A.1. This decomposition is depicted in the top of FigureA.1. Rewriting A.5 in terms of the newly defined γ and subsituting the particular values $\mu = 0$ and $t = \Delta$ one gets:

$$\mathcal{H}_{Kitaev} = -it \sum_{1}^{N-1} \gamma_{i,2}\gamma_{i+1,1} \tag{A.7}$$

Now introduce new fermion operators such that the pairing of the Majoranas is redefined:

$$\tilde{c}_i = \frac{1}{2}(\gamma_{i+1,1} + i\gamma_{i,2}) \tag{A.8}$$

The new pairing is shown on the bottom of FigureA.1. The Hamiltonian in terms of the $\tilde{c}_i$ now writes

$$\mathcal{H}_{Kitaev} = 2t \sum_{1}^{N-1} \tilde{c}_i^\dagger \tilde{c}_i \tag{A.9}$$

This Hamiltonian counts the number of fermions $\tilde{c}_i^\dagger$ in the chain and its ground state is when the chain is empty. However there is a degeneracy, since one fermion operator is missing:

$$\tilde{c}_M = \frac{1}{2}(\gamma_{N,2} + i\gamma_{1,1}) \tag{A.10}$$

Thus the ground state of $\mathcal{H}_{Kitaev}$ is degenerate, with the same energy whether the highly delocalized fermion state $\tilde{c}_M$, composed of two Majoranas, is full or empty. Although we presented the case $\mu = 0$ and $t = \Delta$, it is true if the chemical potential is within the gap $|\mu| < 2t$.

That is, a one-dimensional p-wave superconductor has two topological phases: the 'trivial regime' where the DOS is gapped as for a normal s-wave superconductor, and the non-trivial regime which allows degenerate zero-energy excitations which demonstrate Majorana statistics. These zero-energy excitations are called Majorana bound states, always come in pairs and are spatially delocalized: the individual Majoranas forming the fermionic pair be found at the two ends of a one dimensional chain.

Although spinless p-wave paired superconductors readily host MBS when driven to the topological regime, the few materials predicted to owe such a pairing are very difficult to process and are sensitive to disorder[6].

Luckily, a p-wave superconductor can be engineered from a 1-D semiconductor with induced s-wave pairing, Zeeman interaction E_Z and strong spin-orbit interaction α_{SO}, such as an InSb nanowire[7]. The Hamiltonian of such a system can be written as:

[1] The pairing is p-wave since the spin of each fermion is not defined

A

$$\mathcal{H}_{BdG} = \begin{bmatrix} H_0 & \Delta \\ \Delta^\star & -\mathcal{T} H_0 \mathcal{T}^{-1} \end{bmatrix} \tag{A.11}$$

With

$$\Delta = \begin{bmatrix} 0 & e^{i\varphi}\Delta \\ -e^{i\varphi}\Delta & 0 \end{bmatrix}, H_0 = \begin{bmatrix} \frac{\hbar^2 k_x^2}{2m} - \mu & E_Z + i\alpha_{SO}k_x \\ E_Z - i\alpha_{SO}k_x & \frac{\hbar^2 k_x^2}{2m} - \mu \end{bmatrix}, -\mathcal{T} H_0 \mathcal{T}^{-1} = \begin{bmatrix} -\frac{\hbar^2 k_x^2}{2m} + \mu & -E_Z \\ -E_Z + i\alpha_{SO}k_x & - \end{bmatrix}$$

As shown in references [7, 8], the relevant parameter describing the topology of the system is $E_{gap,k=0}$, the size of the gap in the system at zero momentum. It is equal to

$$E_{gap,k=0} = \sqrt{\Delta^2 + \mu^2} - E_Z. \tag{A.12}$$

When $E_{gap,k=0} > 0$ the system is in the topologically trivial regime with a finite sized gap. When $E_{gap,k=0} < 0$ the system is driven to the non-trivial regime and two degenerate zero-energy solutions appear, corresponding to a pair of MBS.

ZERO BIAS PEAK IN TUNNELLING CONDUCTANCE

An ideal nanowire in proximity of an s-wave superconductor with gap Δ has no available electronic states inside the gap due to the induced pairing in the topologically trivial regime. In the non-trivial regime where such a nanowire hosts a pair of Majorana fermions, the conduction channel containing the MBS admits a zero energy state with conductance of $2e^2/h$ [9, 10].

This zero-energy delocalized bound state can most readily be detected via a voltage biased tunnel spectroscopy measurement. In such a setup, conductance through the nanowire is suppressed (to zero, ideally) within the gap in the trivial regime, and show a peak at zero bias (of ideal height $2e^2/h$) in the non-trivial regime.

The earliest experiment on nanowires contacted by a superconductor and a normal metal exhibiting zero-bias peaks (ZBP) at finite magnetic field, was reported in Delft [11]. The device was an InSb nanowire with one superconducting contact made from NbTiN and a normal gold contact, with local gates to tune the chemical potential and to create a tunnel barrier.

As the magnetic field is increased, $E_{gap,k=0}$ decreases and becomes negative above a critical field value B_C (such that $E_Z(B_C) = \sqrt{\Delta^2 + \mu^2}$) where the wire becomes topological. Indeed a ZBP at finite field is observed which is non-existent at zero magnetic field.

Although Reference [11] is the first experimental milestone in condensed matter Majorana research, it also revealed experimental difficulties and theoretical discrepancies, such as:

- The ZBP height is considerable less than the expected value $2e^2/h$.
- The conductance inside the gap does not vanish, as one would expect in an ideally gapped material. This implies electronic states inside the nanowire within the gap, so-called quasiparticle states. These quasiparticle states can poison the Majorana signal, as we shall see later.

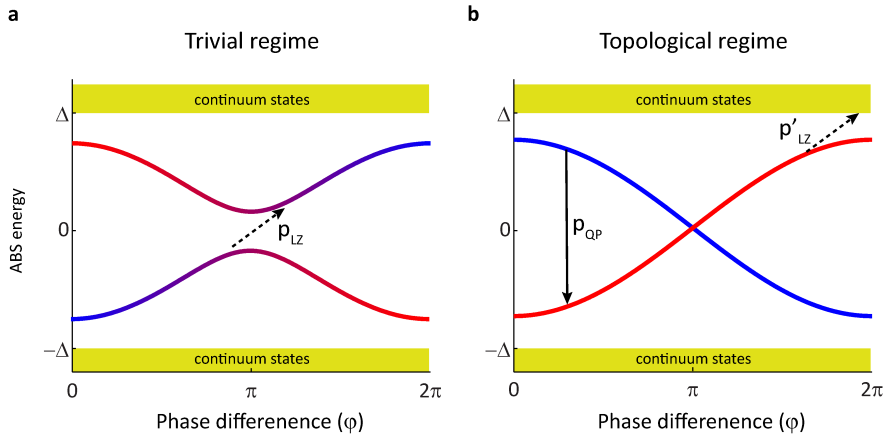

Figure A.2: **ABS dispersion for an SNS junction in the trivial regime and for a junction hosting MBS. a,** The ABS of different parity of a junction in the trivial regime are coupled and are 2π periodic in phase. Landau-Zener transitions can keep the parity constant. **b,** As the junction becomes topologically non-trivial, the ABS periodicity doubles from 2π period to 4π period. Landau-Zener transitions to the continuum and quasiparticle poisining can restore the 2π periodic signature.

Moreover, a number of microscopic phenomena result in a zero bias conductance peak beside Majorana fermions, such as Kondo state or disorder[10]. Below we discuss other methods related to supercurrent flow through Majorana states, offering diverse experimental signatures of the topological regime.

A.2. SIGNATURES OF MBS IN SUPERCONDUCTING NANOWIRES

EXPERIMENTS CARRYING SIGNATURES OF 4π PERIODICITY

The most important signature of a Josephson junction hosting Majorana bound states is the doubling of the ABS period as a function of the phase, called the 4π effect. In Reference[8] the authors derive the CPR of a single mode 1-d channel JJ, with a geometry such that the inner Majoranas are allowed to hybridize through the junction of length $L \ll \xi$ but the outer Majoranas are exponentially far away so that they do not couple to the junction.

A single channel JJ with transmission t in the trivial phase hosts a spin-degenerate pair of ABS of opposite parity . For realistic values of $t<1$, where for example spin-orbit coupling is responsible for coupling the ABS with opposite parities, a gap opens in the ABS spectrum around zero energy as shown in FigureA.2**a**.

In the non-trivial regime (FigA.2**b**), the zero energy crossing of the ABS is topologically protected, meaning the zero energy solution is practically[2] robust with respect to perturbations of local parameters. The ABS are thus 4π periodic instead of 2π, implying a range of observable effects accompanying this period doubling sensitive to the

[2] Although there is a small gap around the Fermi level due to the overlap of the outer Majoranas of the junction, the size of this gap drops exponentially with the distance between the Majoranas[12], and thus can be made arbitrarily small in an experiment.

junction's energy dispersion in phase. It is worth noting however, that it is possible to generate a 4π phase periodic signal from a trivial junction if the gap around the Fermi level is small enough for Landau-Zener transitions to take place as shown in FigureA.2**a**.

In References [13, 14] the authors calculate the behavior of the MAR and I_c signatures which differ whether in the trivial or the non-topological phase. However the observation of these effects require large supercurrents which are difficult to achieve at high magnetic fields where the transition is expected.

DOUBLING OF THE CPR PERIOD

The period doubling of the ABS energies $E_A(\varphi)$ from 2π ($E_A(\varphi) = E_A(\varphi+2\pi)$) to 4π ($E_A(\varphi) = -E_A(\varphi+2\pi) = E_A(\varphi+4\pi)$) while transitioning from the trivial to the topologically non-trivial regime directly implies the period doubling of the CPR of the JJ hosting the Majoranas via 2.32. Thus measuring the period doubling of the CPR in a junction is a signature of Majorana fermions. The CPR of a junction can be measured with various methods:

- The junction can be embedded in a DC-SQUID in parallel with a junction of much higher critical current with known CPR (see section 2.5.2).
- The junction can be embedded in a RF-SQUID which in turn is inductively coupled to a tank circuit. The junction inductance and thus the CPR can be inferred from the tank circuit's resonant frequency shift as a function of flux through the RF-SQUID.
- Measuring $E_A(\varphi)$ directly is also a way to deduce the CPR. Bretheau et. al. used this method in [15] for an aluminum break junction, which they embedded in a DC-SQUID in order to phase bias the junction and subsequently measure the radiation emitted by the SQUID via a spectrometer JJ.

JOSEPHSON RADIATION

The AC Josephson effect warrants an emitted Josephson radiation of frequency $\nu_J = \frac{qV}{h}$ from a junction biased by voltage V with phase coherent transfer of charge q. For a junction in the non-topological regime, $q = 2e$ the charge of a Cooper pair. For a junction in the topological regime, quasiparticles of charge $q = e$ can be coherently transferred through the zero energy MBS, consequently such a junction emits radiation at half the Josephson frequency $\nu = \frac{eV}{h}$. Thus detecting the Josephson radiation can provide evidence for MBS in the junction.

MISSING ODD SHAPIRO-STEPS

A JJ with Josephson frequency $\frac{qV}{h}$ exposed to external radiation ν_0 exhibits Shapiro steps in the I-V curve at exact multiples of the voltage $V = \frac{nh\nu_0}{q}$ for integers n. Thus as the junction is pushed to the topological phase, q changes from $2e$ to e and every odd frequency Shapiro step $V = \frac{(2k-1)h\nu_0}{q}, k \in \mathbb{Z}$ vanishes, as of another signature for Majoranas.

The disappearance of some odd steps was observed in nanowire devices in reference [16], however this can also be caused by high microwave power known to influence Shapiro step visibility.

QUASIPARTICLE POISONING PROBLEM

A Josephson junction in the topological regime hosts a pair of ABS both 4π periodic in phase and of opposite quasiparticle parity. In realistic junctions however, the MBS lifetime is finite and the junction switches parity, allowing relaxation to the ground state and restoring the 2π periodic CPR signature.

In reference [17] the authors take into account the effects contributing to a finite MBS lifetime, which could result from

- Quasiparticles hopping from the electrodes on the junction or vice-versa switching the parity of the MBS. This is represented by the continuous arrow in FigureA.2**b** showing the phase particle switching branches.
- A dynamically evolving junction phase coupled to the continuum states, represented by a dashed-dotted arrow in FigureA.2**b**.

Thus measuring the CPR too slow results in 2π periodicity since the junction will relax to its ground state corresponding to the parity of lower energy for a fixed phase. If the CPR is measured too fast, transitions to the continuum states via LZ tunneling will reset the parity and also results in 2π periodicity. Hence there exists an optimum phase evolution rate window within which 4π signatures are observable.

Increasing the poisoning lifetime of the junction by building quasiparticle traps can increase the detection efficiency by expanding the time window within which the CPR has to be measured. In reference [18] on-chip quasiparticle traps allowed for quasiparticle lifetime above 1 minute in islands of NbTiN. Adapting such techniques to JJs including nanowires can substantially facilitate measurements of MBS signatures.

BIBLIOGRAPHY

[1] E. Majorana, "Teoria simmetrica dell'elettrone e del positrone," *Nuovo Cim*, vol. 14, pp. 171–184, Sept. 2008.

[2] N. Read and D. Green, "Paired states of fermions in two dimensions with breaking of parity and time-reversal symmetries and the fractional quantum Hall effect," *Phys. Rev. B*, vol. 61, pp. 10267–10297, Apr. 2000.

[3] D. A. Ivanov, "Non-Abelian Statistics of Half-Quantum Vortices in p-Wave Superconductors," *Phys. Rev. Lett.*, vol. 86, pp. 268–271, Jan. 2001.

[4] A. Y. Kitaev, "Unpaired Majorana fermions in quantum wires," *Phys.-Usp.*, vol. 44, no. 10S, p. 131, 2001.

[5] A. Stern, "Non-Abelian states of matter," *Nature*, vol. 464, pp. 187–193, Mar. 2010.

[6] S. Das Sarma, C. Nayak, and S. Tewari, "Proposal to stabilize and detect half-quantum vortices in strontium ruthenate thin films: Non-Abelian braiding statistics of vortices in a ${p}_{x}+i{p}_{y}$ superconductor," *Phys. Rev. B*, vol. 73, p. 220502, June 2006.

[7] Y. Oreg, G. Refael, and F. von Oppen, "Helical Liquids and Majorana Bound States in Quantum Wires," *Phys. Rev. Lett.*, vol. 105, p. 177002, Oct. 2010.

[8] R. M. Lutchyn, J. D. Sau, and S. Das Sarma, "Majorana Fermions and a Topological Phase Transition in Semiconductor-Superconductor Heterostructures," *Phys. Rev. Lett.*, vol. 105, p. 077001, Aug. 2010.

[9] M. Wimmer, A. R. Akhmerov, J. P. Dahlhaus, and C. W. J. Beenakker, "Quantum point contact as a probe of a topological superconductor," *New J. Phys.*, vol. 13, no. 5, p. 053016, 2011.

[10] J. Liu, A. C. Potter, K. T. Law, and P. A. Lee, "Zero-Bias Peaks in the Tunneling Conductance of Spin-Orbit-Coupled Superconducting Wires with and without Majorana End-States," *Phys. Rev. Lett.*, vol. 109, p. 267002, Dec. 2012.

[11] V. Mourik, K. Zuo, S. M. Frolov, S. R. Plissard, E. P. a. M. Bakkers, and L. P. Kouwenhoven, "Signatures of Majorana Fermions in Hybrid Superconductor-Semiconductor Nanowire Devices," *Science*, vol. 336, pp. 1003–1007, May 2012.

[12] L. Fidkowski, R. M. Lutchyn, C. Nayak, and M. P. A. Fisher, "Majorana zero modes in one-dimensional quantum wires without long-ranged superconducting order," *Phys. Rev. B*, vol. 84, p. 195436, Nov. 2011.

[13] P. San-Jose, J. Cayao, E. Prada, and R. Aguado, "Multiple Andreev reflection and critical current in topological superconducting nanowire junctions," *New J. Phys.*, vol. 15, no. 7, p. 075019, 2013.

[14] P. San-Jose, E. Prada, and R. Aguado, "Mapping the Topological Phase Diagram of Multiband Semiconductors with Supercurrents," *Phys. Rev. Lett.*, vol. 112, p. 137001, Apr. 2014.

[15] L. Bretheau, . . Girit, H. Pothier, D. Esteve, and C. Urbina, "Exciting Andreev pairs in a superconducting atomic contact," *Nature*, vol. 499, pp. 312–315, July 2013.

[16] L. P. Rokhinson, X. Liu, and J. K. Furdyna, "The fractional a.c. Josephson effect in a semiconductor-superconductor nanowire as a signature of Majorana particles," *Nat Phys*, vol. 8, pp. 795–799, Nov. 2012.

[17] M. Houzet, J. S. Meyer, D. M. Badiane, and L. I. Glazman, "Dynamics of Majorana States in a Topological Josephson Junction," *Phys. Rev. Lett.*, vol. 111, p. 046401, July 2013.

[18] D. J. van Woerkom, A. Geresdi, and L. P. Kouwenhoven, "One minute parity lifetime of a NbTiN Cooper-pair transistor," *Nat Phys*, vol. 11, pp. 547–550, July 2015.

B

METHODS

In this chapter we give details of the sample fabrication process as well as the measurement conditions and measurement electronics used for experiments detailed in the thesis.

B.1. NANOFABRICATION

All samples were processed in the Kavlo Nanolab in Delft. The patterns were generated via electron beam lithography using a Raith EBPG-5000+ system. Each processing step involves spinning resist on the chip, Ebpg lithography, pattern development, deposition or etching and resist liftoff. Between each processing step, the sample is imaged under a scanning electron microscope (SEM) for quality checking and to align subsequent fabrication patterns. The details of each processing step are presented in table 1. The substrate used for the samples is p-doped silicon covered with a 285 nm thick thermally annealed SiO_2; the doped Si is optionally used as a global backgate. The substrate is thoroughly cleaned with HNO_3 prior to processing.

B.2. NANOWIRE GROWTH, DEPOSITION AND CONTACTING

The nanowires used in the thesis are all InSb grown in Eindhoven in an MOVPE(metal organic vapor phase epitaxy) chamber. The wires are grown on InP (111) substrate via a gold cathalyst distributed on the substrate via a colloid. Growth results in an average wire diameter of 100 nm and wire length 2-4 μm. Details of the growth can be found in Reference [1].

The nanowires are transferred individually from the growth chip to the sample substrate via a nanowire manipulator [2, 3]. The wires are transferred on the dielectric of the sample chip, i.e. on to the SiO_2 prior to processing in case of only global backgated chip, or on the Si_3N_4 if local fine gates are used. The individual wire transfer allows firstly to select nanowires of suitable length: in case of SQUID devices, the wires need to be at least 2.5 μm long such that there is space for three contacts. Secondly, once a nanowire is deposited, it is possible to realign the nanowire such that its axis is perpendicular to the

B

Process	Resist type and spin speed	Deposition system	Material deposited and thickness	Lift off
Ebeam markers	PMMA 495k a4 @5000 rpm; PMMA 950k a3 @6000 rpm	AJA ebeam evaporator	5 nm Ti/ 80 nm Au	Acetone in ultrasonic bath
Local gates	PMMA 950k a2 @5000 rpm	AJA ebeam evaporator	5 nm Ti/ 10 nm Au	Acetone in ultrasonic bath
Dielectric	PMMA 950K A4 @4000 rpm	Alliance Concept RF magnetron sputter deposition	25 nm Si_3N_4	Acetone in ultrasonic bath
Super-conducting contacts	PMMA 950K A4 @4000 rpm	AJA magnetron sputter system	Rf plasma etch; NbTiN 120 nm	Hot acetone
Normal contacts	PMMA 495k a4 @5000 rpm; PMMA 950k a3 @6000 rpm	AJA ebeam evaporator	Sulfur passivation; 10nm Ti/ 150 nm Au	Hot acetone
Top gates	PMMA 495k a4 @5000 rpm; PMMA 950k a3 @6000 rpm	AJA ebeam evaporator	10nm Ti/ 150 nm Au	Hot acetone

Table B.1: **List of the processing steps used during sample fabrication and their details.**

local gates and aligned with the magnet axis defined by the setup in which the sample is measured. For these reasons, individual wire transfer is preferred to random mass transfer.

As soon as the nanowires are exposed to air, the surface oxidizes through a thickness of 2-4 nm. This surface oxide layer acts as a dielectric and is electrically insulating. Thus, while allowing electrical leads to act as topgates without requiring the deposition of additional dielectric material, it is critical that the oxide layer is removed prior to contacting the wire. For superconducting contacts, this is achieved by an in-situ Argon rf-plasma etch in the sputtering machine just before contact deposition. For gold contacts, the sample is passivated in a Sulphur solution as described in reference [4].

B.3. ROOM TEMPERATURE CHARACTERIZATION AND BONDING

When all the fabrication steps are complete, the sample chip is diced with a diamond cutter to appropriate size. The device resistances are then probed at room temperature by pressing needles to the metallic bond pads in which the electrical leads terminate. As there are usually 5-6 devices per sample chip but only 2 or 3 can be electrically connected inside the dilution refrigerator, this step serves to select the devices with lowest resistance. For a nanowire device with channel length up to 200 nm, a 10-20kΩ resistance is considered good. Devices around 50kΩ can still perform well at low temperatures. Devices of resistance 100kΩ and beyond are rejected.

The sample chip is glued via conducting silver paint on copper bracket which is directly in contact with the mixing chamber of the dilution unit (DU), or on a gold chip carrier[1]. The appropriate devices on the sample chip are then bonded on a PCB (printed circuit board) or chip carrier with aluminum wires using an ultrasonic ball bonder. The PCB is mounted on the bracket and is electrically connected to DC lines running through the fridge.

B.4. COLD TEMPERATURE AND MEASUREMENT ELECTRONICS SETUP

In order to proximitize the nanowire and measure dissipationless supercurrent through it, the sample needs to be cooled to the millikelvin range. The DC electric lines are thermally anchored at several stages of the DR to minimize the electron temperature. All the samples in the thesis have been measured in a dilution refrigerator (DR) with electron temperature 20-50 mK, with the exception of Chapter 4 where a smaller dilution unit of electron temperature 100 mK was used. The colder DRs used were so-called 'dry fridges' where a pulse tubed is used to cool the 4K stage. The warmer DR is a 'wet fridge' where the DU is dunked into a He4 bath at 4K. To measure supercurrent of the order of pico Amperes, it is necessary to use electronic filters covering the full high frequency range. Copper powder filers (covering the range $\omega > 0.5$GHz) and RC-filters (covering the range $1kHz < \omega < 0.5$GHz) are mounted on the mixing chamber plate or on the PCB. The filters and the sample are enclosed inside a copper shield to protect from the

[1] In case a global backgate is used, an insulating layer such as sapphire is inserted between the sample chip and copper bracket or chip carrier

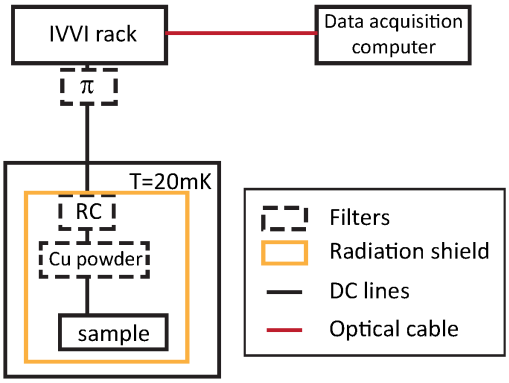

Figure B.1: **Measurement setup and electronic filters.**The sample is shielded from 50 Hz and high frequency noise.

outside radiation. Additional room temperature Pi filters are built in the measurement electronics. Measuring and applying current/voltage is performed by the IVVI rack built and maintained by Raymond Schouten at TU Delft. The IVVI rack is battery powered so to electronically isolate the sample and measurement apparatus from 50 Hz noise. Communication between the computer governing the measurement and the IVVI rack is maintained via optical fiber. The diagram of the measurement setup is shown if FigureB.1.

BIBLIOGRAPHY

[1] S. R. Plissard, D. R. Slapak, M. A. Verheijen, M. Hocevar, G. W. G. Immink, I. van Weperen, S. Nadj-Perge, S. M. Frolov, L. P. Kouwenhoven, and E. P. A. M. Bakkers, "From InSb Nanowires to Nanocubes: Looking for the Sweet Spot," *Nano Lett.*, vol. 12, pp. 1794–1798, Apr. 2012.

[2] K. Flöhr, M. Liebmann, K. Sladek, H. Y. Günel, R. Frielinghaus, F. Haas, C. Meyer, H. Hardtdegen, T. Schäpers, D. Grützmacher, and M. Morgenstern, "Manipulating InAs nanowires with submicrometer precision," *Review of Scientific Instruments*, vol. 82, p. 113705, Nov. 2011.

[3] D. J. van Woerkom, *Majorana fermions in well aligned InSb-nanowires with superconducting and normal contacts.* MSc thesis, TU Delft, Delft, Netherlands, 2012.

[4] D. B. Suyatin, C. Thelander, M. T. Björk, I. Maximov, and L. Samuelson, "Sulfur passivation for ohmic contact formation to InAs nanowires," *Nanotechnology*, vol. 18, no. 10, p. 105307, 2007.

ACKNOWLEDGEMENTS

My quest for a PhD began in February 2011, while visiting Delft for an interview in Leo's lab. It has been a long bumpy road since, which I am very grateful to have traveled, and which shaped me to what I am now. This extraordinary adventure would not have been possible without great many people, a few of which I thank on these pages.

First of all thank you Leo for giving me the opportunity to join your research. You have provided me with all the necessary resources, time and faith needed to succeed. Your scientific vision is outstanding as well as the fluency with which you communicate scientific ideas to anyone with any level of understanding. Your truly libertarian style of conducting science will always be a model for me.

When I arrived to QT my experimental skills barely matched that of a mathematician or theoretical physicist. Here I thank my mentors who taught me the art of measuring: Sergey, our overlap was brief yet influential. I still remember the three possible device layouts you presented me to accomplish my PhD (number 2 was the winner). Attila, you introduced me basic electronic skills and expert fridge skills. Stevan, I am glad you joined even if late, your help with the search for quantum dots and writing up our paper was invaluable. Can you believe I nearly broke our golden device three times? And yet after each resurrection we found a nicer regime.

My fellow team members in the Topo-team were not less influential: they taught me the art of working in the cleanroom, cooling down and measuring in the late night, and scientific politics. Kun* and Vincent* (equal contributors), your warm welcome to the group never ceased and was a significant reason of me coming here in the first place. I learned a tremendous lot from our discussions about science and about practicing science. I hope we meet again soon in the eastern part of the world. Ludo, you were a more than model master student and I wonder if I taught you anything at all, so I will take pride in the fact that you decided to take on a PhD during your masters project.

About half-way in my PhD the Topo-team reached an inflationary epoch and grew from a small family to a large team: Önder, David, Jakob, Jasper, Fokko, Michiel, James , Alex, Fanming, Maja, Hao and everyone else, thank you for providing such a vibrant and diverse environment.

My research could not have been realized without our exceptional nanowire growers from Eindhoven. Diana, go and spread the crazy fire within wherever you go, don't let anyone else tell you otherwise. Erik, I wish we had discussed more often; even on the gloomier days of my project you were always attentive and radiating confidence.

A first class research environment depends heavily on a strong supporting staff without which my research would still be stuck in its incubation phase: Bram, Remco, Jelle, Mark and Jason, thank you for your prompt technical support, fixing anything on demand, let it be fridge, evaporator or helium. Raymond, your passion for electronics is boundless and admirable. Thanks to you and Ruud, Jack and Rogier for providing me with the best equipment for my project. Many thanks for the cleanroom staff of the VLL for tutoring

me on machines, repairing the Ebeam countless times and cleaning up after me on the sulfur bench. And I won't forget to mention our wonderful administrative staff: Marja, Yuki, Heera, Simone and Chantal, thank you for helping out with booking flights, filling out tax forms, organizing uitjes and lending a listening ear when needed.

Since I cannot mention all the names I must thank the whole of QT(ech) in general, and in particular the PIs for this hot bed for scientific inspiration as well as host of crazy parties. Leo K, Leo DC, Ronald and Lieven, thank you for creating this environment. I dearly hope the institution of the QT uitje will strive for long.

And now I'd like to thank people who have supported me not only professionally but on a personal level. I have to name my office mates with whom we shared the enchanted rooms B62-20. Martin and Vishal I hope you found your better life you were seeking. Iman, your optimistic pessimism is truly charming. Machiel, you let me in on the secret of the broodje lente for which I owe an eternal supply to you. We should all have an office party in the hout once again.

My flatmates deserve a huge recognition for bearing me in the D-house (thanks Ronald for illustrious name) which we managed to turn into the in-town designated QT before and afterparty hotspot. Önder, I wish you the best in Boston, your dedication will be most valuable there as well. Stefan, may you dance Serbian style in many more weddings to come and spread your boundless positive attitude. Nodar, you were honorary inhabitant before even becoming one. I wish our tantalizing secret project lasted longer. May you find the path dedicated for you.

During my PhD years we assembled a sizable crew of peeps with the mission of reconnecting our body with the mind through rhythm. Vincent, I'm happy I could give you something in return of the many beers in the office. Kun, so glad you could also make it. Diana, your spirit brought you despite the music. Ale and Anaïs (and Vincent), what a truly memorable concert we rocked up to in Austin. Marco, I'm sure the SUN festival was more than what you asked for but you lived through it! And James, Stefan, Nodar, Debbie, your names can't miss from this paragraph either.

I could have not assumed my body in this world without my bloodline, who will always play an important role behind the scene. I want to thank my parents for their support and for drawing out this path since early childhood. And my brother Kristóf for feeding and nurturing my imagination from my infancy.

I came to Delft to find scientific truth and as the irony of life, found love instead. My dear Sára, it seems as if everything in life was leading to our encounter on that sunny Monday afternoon of June 2015. You are my guiding light, showing me the way to dance through life. Let's jump on our next adventure and open a new chapter: the Szaturday's in the land of Oz.

Daniel Szombati
Budapest, February 2017

CURRICULUM VITÆ

Daniel SZOMBATI

11-02-1986	Born in Budapest, Hungary.
1999–2005	Secondary Education Berzsenyi Dániel Gimnázium, Budapest (1999–2002, 2004-2005) Lycée Français Charles de Gaulle British Section, United Kingdom (2002–2004)
2005–2008	Undergraduate in Mathematics University of Cambridge, UK
2008–2009	Educational consultant Heymath! Innovation Lab Chennai, India
2009-2010	MSc. Physics École Polytechnique Fédérale de Lausanne, Switzerland
2010-2011	MSc. Physics Columbia University, USA *Thesis:* Ultrafast optical spectroscopy of Bismuth *Supervisor:* Prof. László Forró, Prof. Tony Heinz
2011–2017	PhD research, Delft University of Technology *Thesis:* Superconducting InSb nanowire devices *Promotor:* Prof. dr. L.P. Kouwenhoven

LIST OF PUBLICATIONS

4. **D. B. Szombati,** S. Nadj-Perge, D. Car, S. R. Plissard, E. P. A. M. Bakkers, L. P. Kouwenhoven, *Josephson φ_0-junction in nanowire quantum dots.*, Nature Physics **12**, 568 (2016).

3. K. Zuo, V. Mourik, **D. B. Szombati**, B. Nijholt, D. J. van Woerkom, A. Geresdi, J. Chen, V. P. Ostroukh, A. R. Akhmerov, S. R. Plissard, D. Car, E. P. A. M. Bakkers, D. I. Pikulin, L. P. Kouwenhoven and S. M. Frolov, *Supercurrent interference in few-mode nanowire Josephson junctions*, In submission.

2. S. R. Plissard, I. van Weperen, D. Car, M. A. Verheijen, G. W. G. Immink, J. Kammhuber, L. J. Cornelissen, **D. B. Szombati**, A. Geresdi, S. M. Frolov, L. P. Kouwenhoven and E. P. A. M. Bakkers *Formation and electronic properties of InSb nanocrosses*, Nature Nanotechnology **8**, 859 (2013).

1. V. Ranjan, G. de Lange, R. Schutjens, T. Debelhoir, J. P. Groen,**D. B. Szombati**, D. J. Thoen, T. M. Klapwijk, R. Hanson, L. DiCarlo , *Probing dynamics of electron-spin ensemble via a superconducting resonator*, Physical Rev. Lett. **110**, 067004 (2013).